ABSTRACT

FORMATION OF SCREEN-PRINTED CONTACTS ON MULTICRYSTALLINE SILICON (mc-Si) SOLAR CELLS

by
Vishal R. Mehta

Commercial multicrystalline silicon (mc-Si) solar cells use screen-printing process for depositing both the Ag paste based gridded front and Al based back (whole area) metal contacts. This thesis relates to experimental and theoretical studies of contact formation mechanisms in silicon solar cells. Temperature distribution studies during optical processing by attached thermocouples to cells indicates that the maximum temperature reached under the front silver metal is less than 800°C; this is lower than the eutectic point of Ag-Si (≈835°C). An analysis of the interaction of Ag particles and Si via the constituents of glass is given. This mechanism leaches metallic ions (solvent metals such as Pb, Bi or Zn), which cover the Ag particles and form a material of surface composition with low-melting-point. The low-temperature melt facilitates agglomeration of Ag and formation of a shallow alloy between Si, Ag, and the solvent metal. Ag-glass-Si interactions lead to the formation of Ag-rich and Si-rich areas at the metal-semiconductor interface. The non-uniformity of the Ag-Si interaction leads to degradation of various electrical parameters (i.e., fill factor and open circuit voltage (V_{oc})).

A hypothesis invoking ion exchange phenomena for front contact formation is presented. Ag-Si, Ag-glass, glass-Si and Ag-glass-Si reactions are discussed. SIMS study on etched cells shows that a significant consumption of phosphorous occurs during Si-Ag interaction. Scanning Kelvin Probe Microscopy profiles have been studied to measure the surface potential of the metal semiconductor region. Current Voltage characteristics of

the fired cells are presented. An improved technique to cross-section large lengths of wafers/solar cells for statistically meaningful analyses of the metal semiconductor interface is presented. Results and applications of study of the temperature distribution across the cell during firing, by contact thermocouples are presented. Thermal modeling predicts a temperature gradient of more than 10°C across the cell width due to combined effect of shadowing and thermal mass of the metal grid. However, experimentally, no systematic effect of the temperature gradient is seen on the front contact formation mechanism. A study on the back Al contact formation revealed that Si diffusion led to several defects (e.g. bumps, holes, shunts) in the cells.

FORMATION OF SCREEN-PRINTED CONTACTS ON MULTICRYSTALLINE SILICON (mc-Si) SOLAR CELLS

by
Vishal R. Mehta

A Dissertation
Submitted to the Faculty of
New Jersey Institute of Technology
in Partial Fulfillment of the Requirements for the Degree of
Doctor of Philosophy in Materials Science and Engineering

Interdisciplinary Program in Materials Science and Engineering

May 2010

APPROVAL PAGE

FORMATION OF SCREEN-PRINTED CONTACTS ON MULTICRYSTALLINE SILICON (mc- Si) SOLAR CELLS

Vishal R. Mehta

Dr. N. M. Ravindra, Dissertation Co-Advisor — Date
Professor of Physics, NJIT

Dr. Bhushan Sopori, Dissertation Co-Advisor — Date
Principal Engineer, National Renewable Energy Laboratory, Golden, CO

Dr. Trevor A Tyson, Committee Member — Date
Professor of Physics, NJIT

Dr. Anthony Fiory, Committee Member — Date
Research Professor of Physics, NJIT

Dr. Tao Zhou, Committee Member — Date
Associate Professor of Physics, NJIT

Dr. Przemyslaw Rupnowski, Committee Member — Date
Researcher, National Renewable Energy Laboratory, Golden, CO

BIOGRAPHICAL SKETCH

Author: Vishal R. Mehta

Degree: Doctor of Philosophy

Date: May 2010

Undergraduate and Graduate Education:

- Doctor of Philosophy in Materials Science and Engineering,
  New Jersey Institute of Technology, Newark, NJ, 2010

- Master of Science in Materials Science and Engineering,
  New Jersey Institute of Technology, Newark, NJ, 2002

- Bachelor of Engineering in Metallurgy,
  Maharaja Sayajirao University of Baroda, Vadodara, India, 1995

Major: Materials Science and Engineering

Presentations and Publications:

Mehta, V., Sopori, B. L., Rupnowski, P., Reedy, R., Appel, J., & Domine, D., & N. M. Ravindra. Formation of Ag-Si contact in fire-through metallization for solar cells: experimental studies. To be published *in Journal of Materials Science*.

Mehta, V., & Sopori, B. (2009, December). Screen printed Al back contacts on Si solar cells: issues and some solutions. Paper presented at the *2009 MRS Fall Meeting*, Boston, MA.

Sopori, B., Mehta, V., Guhabiswas, D., Reedy, R., Moutinho, H., Bobby, T., Shaikh, A., & Rangappan, A. (2009). Formation of a back contact by fire-through process of screen-printed silicon solar cells. Proceedings of the *34th IEEE Photovoltaic Specialists Conference*, 1963 – 1968. doi: 10.1109/PVSC.2009.5411536

Mehta,V., Sopori, B., Guhabiswas, D., Reedy, R., Moutinho, H., To, B., Liu, F., Shaikh, A., Young, J., & Rangappan, A. (2009, August). A new approach to overcome some limitations of back Al contact formation of screen printed silicon solar cells. Paper presented at the *19th Workshop on Crystalline Silicon Solar Cells and Modules: Materials and Processes*, Vail, CO.

Young, J.L., Mehta, V., Guhabiswas, D., Moutinho, H., Bobby To, Ravindra, N. M., & Sopori, B. (2009, August). Back contact formation in Si solar cells: Investigations using a novel cross-sectioning technique. Poster session presented at *19th Workshop on Crystalline Silicon Solar Cells and Modules: Materials and Processes*, Vail, CO.

Sopori, B., & Mehta, V. (2009, October). Formation of screen-printed contacts on si solar cells. Paper presented at the *216th Electrochemical Society Meeting*, Vienna, Austria.

Sopori, B., Rupnowski, P., Mehta, V., Budhraja, V., Johnston, S., Call, N., Moutinho, H., Al-Jassim, M., Shaikh, A., Seacrist, M., & Carlson, D. (2009). Performance limitations of mc-si solar cells caused by defect clusters, *ECS Trans. 18* (1), 1049.

Sopori, B., Mehta, V., Rupnowski, P., Moutinho, H., Shaikh, A., Khadilkar, C., Bennett, M., & Carlson, D. (2009). Studies on backside Al-contact formation in si solar cells. In B. Sopori, J. Yang, T. Surek, B. Dimmler (Ed.), MRS Symposium on Fundamental Mechanisms. *Photovoltaic Materials and Manufacturing Issues*, *1123*, 7-11, Warrendale, PA.

Sopori, B., Mehta, V., & Knorowski, C. (2008, August). Technique for rapid cross-sectioning of si solar cells with highly planar, damage-free, edge. Poster session presented at the *18th Workshop on Crystalline Silicon Solar Cells and Modules: Materials and Processes*; Vail, CO.

Sopori, B., Rupnowski, P., Mehta, V., & Ewan, M. (2008, August). Mechanism of hillock formation during chemical-mechanical polishing of multi-crystalline silicon wafers. Poster session presented at the *18th Workshop on Crystalline Silicon Solar Cells and Modules: Materials and Processes*, Vail, CO.

Sopori, B., Rupnowski, P., Appel, J., Mehta, V., Li, C., & Johnston, S. (2008). Wafer preparation and iodine-ethanol passivation procedure for reproducible minority-carrier lifetime measurement. Proceedings of the *33rd IEEE Photovoltaic Specialists Conference*, 1-4. doi:10.1109/PVSC.2008.4922688

Sopori, B., Mehta, V. R., Rupnowski, V. R., Domine, D., Romero, M., Moutinho, H., To, B., Reedy, R., Al-Jassim, M., Shaikh, A., Merchant, N., & Khadilkar, C. (2007). Studies on fundamental mechanisms in a fire-through contact metallization of Si solar cells. Proceedings of the *22nd European Photovoltaic Solar Energy Conference*, 841–848.

Sopori, B., Mehta, V., Rupnowski, P., Appel, J., Romero, M., Moutinho, H., Domine, D., To, B., Reedy, R., Al-Jassim, M., Shaikh, A., Merchant, N., Khadilkar, C., Carlson, D., & Bennet, M. (2007). Fundamental mechanisms in the fire-through contact metallization of Si solar cells: A review. Proceedings of *17th Workshop on Crystalline Silicon Solar Cells and Modules: Materials and Processes*, 93-103.

Sopori, B., Mehta, V., Fast, N., Moutinho, H., Domine, D., To, B., & Al-Jassim, M. (2007). Cross-sectioning Si solar cells: Mechanics of polishing. Proceedings of *17th Workshop on Crystalline Silicon Solar Cells and Modules: Materials and Processes*, 222–227.

Mehta, V., Sopori, B., & Ravindra, N. M. (2008, March). Mechanisms of front contact formation in Si solar cell. Paper presented at the *137th Annual TMS Meeting and Exhibition*, New Orleans, LA.

Mehta, V., Sopori, B., Rupnowski, P., Appel, J., Domine, D., Moutinho, H., To, B., Shaikh, A., Merchant, N., Carlson, D., & Ravindra, N. M. (2007, March). Formation of Ag-Si contact in fire-through metallization for solar cells: Experimental studies. Paper presented at *136th Annual TMS Meeting and Exhibition*, Orlando, FA.

Appel, J. S., Sopori, B., Rupnowski, P., Duda, A., Roybal, L., Mehta, V., & Ravindra, N. M. (2008, March). Characterization of solar cell substrates using diode array technique. Paper presented at the *137th Annual TMS Meeting and Exhibition,* New Orleans, LA.

Sopori, B., Rupnowski, P., Appel, J., & Mehta, V., (2006, October). Defect engineering approaches for improving silicon solar cell performance: Characterization, modeling, and cell fabrication. Poster session presented at the meeting of *CU/NREL Energy Symposium*, Boulder, CO.

Ravindra, N. M., Ravindra, K., Rabus, M., Mehta, V.R., Rubin, S.E., Shet, S. & Fiory, A.T. (2005, September). Applications of spectral emissometry. Paper presented at the annual meeting of *Materials Science and Technology Conference and Exhibition,* Pittsburgh, PA.

Ravindra N. M., Mehta, V. R., & Shet, S. (2005). Silicon nano-electronics and beyond: An overview and recent developments. *Journal of Materials*, 57, 6, 16-20.

Mehta, V.R., Shet, S., Ravindra, N.M., Fiory, A. T., & Lepselter, M. P. (2005). Silicon-integrated un-cooled infrared detectors: Perspectives on thin films and microstructures. *Journal of Electronic Materials*, 34, 5, 484-490.

Shet, S., Mehta, V.R., Fiory, A.T., Lepselter, M. P., Ravindra, N. M. (2004). Macro self assembly techniques. *Journal of Materials*, *56*, 11, 300.

Ravindra, N.M., Fiory, A.T., Rubin, S., Shet, S., Mehta, V.R., & Srivatsa, S. (2004). Temperature dependent infrared properties of InP, AIN and Al_2O_3. *Journal of Materials*, *56*, 11, 22.

Shet, S., Mehta, V.R., Fiory, A.T., Lepselter, M. P., & Ravindra, N. M. (2004). The magnetic field- assisted assembly of nanoscale semiconductor devices: A new technique. *Journal of Materials*, *56*, 10, 32-34.

Mehta, V.R., Fiory, A.T., Ravindra, N.M., Ho, M.Y., Wilk, G.D., & Sorsch, T.W. (2003). Flat-band voltage study of atomic-layer-deposited aluminum-oxide subjected to spike thermal annealing. Proceedings of the *Material Research Society,* 765, 109-113.

Dedicated to my mother, Harsha; father, Rajendraprasad;
sister, Divyangi;
wife, Bhargavi; and son, Veer
With love and gratitude

ACKNOWLEDGMENTS

The author wishes to express his sincere gratitude to his co-advisors Dr. N. M. Ravindra at NJIT and Dr. Bhushan Sopori at NREL for their invaluable guidance and perpetual encouragement given to me throughout this research work. I also want to thank Dr. Anthony Fiory, Dr. Trevor Tyson, Dr. Tao Zhou and Dr. Przemyslaw Rupnowski who were kind enough to actively participate in my dissertation committee providing constructive criticisms and valuable suggestions at all stages of this work.

The author is grateful to the U.S. Dept. of Energy for sponsoring this research through subcontract no. ZEA-6-66009-01 with NJIT. The author appreciates the support of Dave Carlson and Murray Bennett from BP Solar, Aziz Shaikh from Ferro for helping him with the samples and sharing their knowledge. The author is grateful to Matt Page, Anna Duda, Robert Reedy and Helio Moutinho (all of NREL) for their support during his research activities.

The author is thankful to Mr. Henry McCloud and Mrs. Lorna Derilhomme Joasil for their continued support during his course of studies. Also, he would like to thank the Graduate Student Association-NJIT and the U.S. Dept. of Energy, for covering his travel expenses to various conferences.

The author expresses words of gratitude to colleagues Dr. Sudhakar Shet, Dr. Takuya Matsunaga, Dr. Jesse Appel, Dr. Chuan Li, Vinay Budhraja, Debraj Guhabiswas and Srinivas Devayajanam for their help and support throughout the course of this research.

TABLE OF CONTENTS

TABLE OF CONTENTS
(Continued)

TABLE OF CONTENTS
(Continued)

LIST OF TABLES

LIST OF FIGURES

LIST OF FIGURES
(Continued)

LIST OF FIGURES
(Continued)

Figure **Page**

LIST OF FIGURES
(Continued)

Figure **Page**

LIST OF FIGURES
(Continued)

Figure **Page**

CHAPTER 1

INTRODUCTION

Thick film metallization is the predominant technology in photovoltaic industry for making contacts to solar cells. More than 86% of the solar cells produced world-wide in 2006 were fabricated using silver thick film contacts on the front side and aluminum thick film contacts on the rear side of the cell (Neuhaus & Munzer, 2007). The advantages of thick film metallization technology are high throughput rate, limited number of process steps, and possibility to benefit from the experience of the microelectronic industry so that, this technology is cost-effective. Efficiencies of at least $\eta = 15.8\%$ on multi-crystalline silicon and at least $\eta = 17.0\%$ on mono crystalline silicon solar cells have currently been attained in the photovoltaic industry.

The industry uses an empirical approach to increase the efficiency of screen printed mc-Si cells. Optimizing thick film front contact metallization process in mc-Si solar cells requires thorough understanding of contact formation and current conduction mechanisms. Hence, despite the success of the fire-through process of contact metallization, many aspects of the physics of the front-contact formation remain unclear. Some of the concerns relate to:

1. Kinetics of Ag-Si interactions—In particular, how do Ag particles, which are dispersed in a matrix of glass frit, interact with the Si surface at temperatures that are considerably lower than the eutectic point?
2. How do Ag particles agglomerate to form a laterally conducting contact, and how does it influence the series resistance of the cell?
3. What is the actual temperature at which Si-Ag forms an alloy, and is this alloy formation aided by the presence of the "solvent metal" M?
4. To what amount does the melting of Ag particles occur?

5. Does Ag get dissolved in glass and re-precipitate, as proposed in some published work (Hilali, 2005, & Ballif, 2003)?
6. How much Si is consumed in a typical contact formation?

The present work addresses these concerns. An inclusive approach was taken in which, all the competing processes in the contact metallization were studied. Electro optical characterization techniques were used on planar cross sections of fired cells to understand how vital constituents have reacted. Current voltage characteristics and electrical losses due to thick film metallization were analyzed. A hypothesis for front contact formation and current conduction is presented.

1.1 Thesis Outline

In Chapter 1, solar cell fundamentals are reviewed. Basic equations for various critical parameters of solar cells are presented. Planar cross section polishing technique is presented and its importance as a sample preparation technique is explained. Various electro-optical characterization tools/techniques used during the course of present study are briefly reviewed.

In Chapter 2, the contact metallization of solar cells is discussed. Initially, brief history of contact metallization on solar cell is presented. Different contemporary metal deposition techniques are briefly discussed and the most widely used method, i.e., screen printing, is discussed in detail. Composition of front Ag paste and back Al paste is elaborated and importance of various constituents is explained. Brief description of optical processing furnace is presented. Fire-through contact metallization (i.e., co-firing) of conventional multi-crystalline Si solar cells is discussed in detail with the help of an optimum firing profile. All three important processes occurring during co-firing, i.e.,

front Ag contact formation, back Al contact formation and Hydrogen passivation are introduced. Chapter 3 is about front contact formation and current conduction mechanisms in mc-Si solar cells. First a brief review of existing hypothesis is presented. Next, experimental details are given and the results are discussed. Detailed explanation about interaction between Ag-Si, glass-Si, glass-Ag, and glass-SiN: H and Ag-Glass-Si is given. A hypothesis about contact formation and current conduction mechanisms is presented.

In Chapter 4, the effect of front grid on the temperature distribution of solar cells is discussed. First, experimental details are elaborated and results discussed. Next, thermal modeling of the effect of front grid on the temperature distribution of solar cells during contact firing using Comsol multi-physics is introduced. Steady state and transient state 3D calculations have been carried out. Results of thermal modeling are presented and discussed. The effect of temperature distribution on the Ag-Si interaction behavior is analyzed.

In Chapter 5, results of Current- Voltage (I-V) characteristics of fired mc-Si solar cells are presented.

1.2 Solar Cell Basics

The mc-Si solar cell studied in this thesis is a pn junction diode (homojunction or single junction). When the cell is illuminated by sun (or xenon lamp), electron hole pairs are generated throughout the device. The built in field separates the light generated carries (see Figure 1.1a). These carriers are then collected by the metal contacts and fed either to the grid or stored in a battery. Figure 1.1b is equivalent circuit of the solar cell. The open circuit voltage (V_{oc}), Short circuit current (I_{sc}), efficiency (η) are some of the important

parameters that characterize the device. V_{oc} (V) is defined as the maximum voltage when the cell is in open circuit (e.g, zero current). I_{sc} (mA/cm^2) is the maximum current given by the device when it is in short circuit. For low series resistance, I_{sc} and I_L (i.e., light generated current) are interchangeable. V_{oc} can be calculated using equation 1.1. Here, I_L is the light generated current, T is the temperature in K, I_0 is the dark saturation current, q is the electronic charge and κ is the Boltzmann constant. The fill factor (FF) is defined as the ratio of the maximum power from the solar cell to the product of V_{oc} and I_{sc} (e.g., see equation 1.2). η is defined as the ratio of the energy output from the cell to the input energy (P_{in}) from the sun (e.g., see equation 1.3).

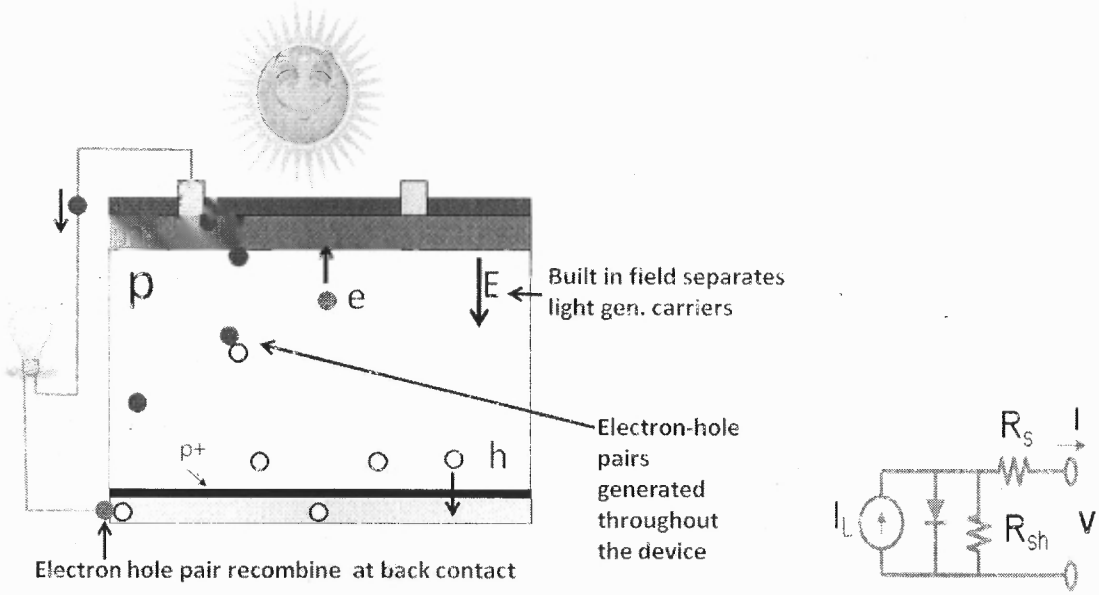

(a) (b)

Figure 1.1 Solar cell basics. (a) Schematic of a Si solar cell, (b) The equivalent circuit diagram of a solar cell.

$$V_{oc} = (\kappa T/q)\ln(I_L/I_0+1) \quad (1.1)$$

$$FF = (V_{mp}I_{mp}/V_{oc}I_{sc}) \quad (1.2)$$

$$\eta = (V_{oc}I_{sc}FF/P_{in}) \quad (1.3)$$

1.3 Fabrication of Industrial mc-Si Solar Cells

A typical cell fabrication process for screen printed mc-Si is shown in Figure 1.2. P type mc-Si is cast as ingots from the crystal growth furnace. Wire sawing is used to cut the ingots into wafers of desired thickness (i.e., 160-180μm). Next, chemical etching step serves to remove saw damage (10 μm) and, subsequently, texture etch (i.e., 4-5μm texture height) the wafers. The wafers are either anisotropically etched in alkaline (NaOH+ Isopropyl alcohol) or isotropically etched acidic solution (HF + HNO_3 + Water). Wafers are then rinsed and dried.

Next, Phosphorus diffusion step is performed on wafer by using either $POCl_3$, or dilute H_3PO_4 to form n+ type layer on p type wafer. It is a high temperature step carried out at 900°C for 25 minutes. The phosphor glass is then removed by acid etching. Sheet resistance of n+ layer (also called as emitter) is usually maintained at 40-50Ω/□. A non-stoichiometric SiN:H based anti-reflection coating (70-80nm thick with refractive index of ≈2.0) is deposited using PECVD technique. The cell is edge isolated using plasma etch. Gridded Ag based front (25 micron thick) and back (whole area) Al based paste (7-10mg/cm^2) are screen printed to serve as contacts. Cells are fired using fire-through contact metallization technique. The cells are tested using current voltage (IV)-characteristics, sorted and sent for module preparation.

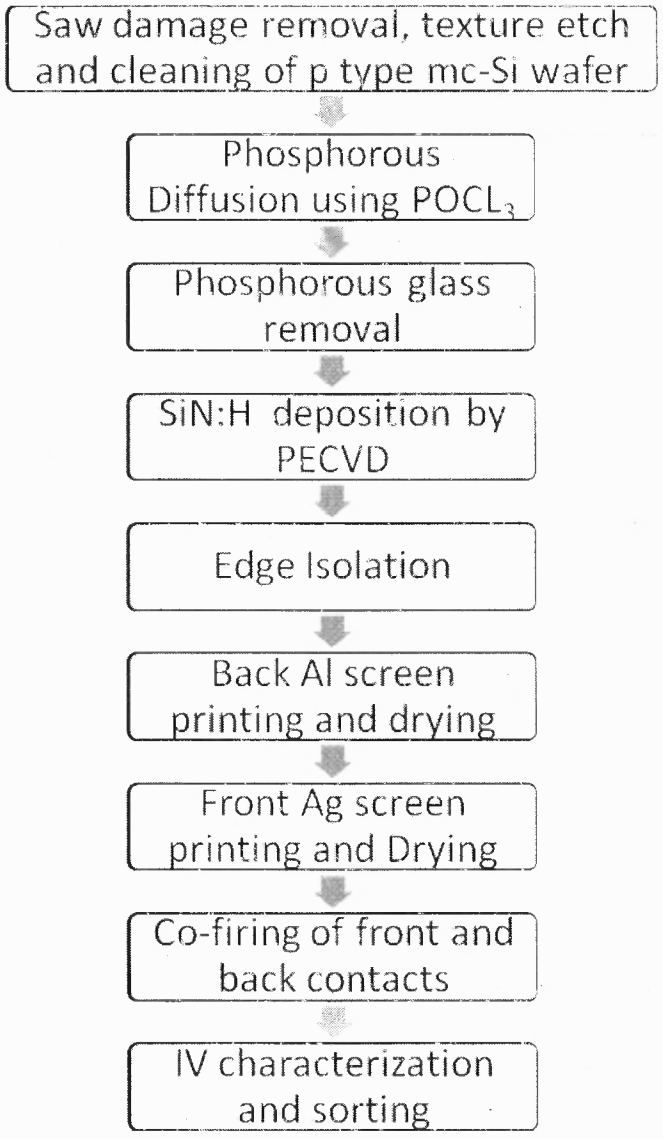

Figure 1.2 mc-Si solar cell processing flow chart.

1.4 Optical Processing Furnace

The screen printed mc-Si solar cells are fired in optical processing furnace (OPF). Developed at National Renewable Energy Laboratory (NREL) by Dr. B. Sopori, the OPF technology has recently been licensed to AOS Solar Inc, CA. As seen from Figure 1.3, the process is controlled in terms of the optical power delivered to the device. This process uses spectrally selected light to create a controlled uniform local melt at an

illuminated semiconductor-metal interface. This melt forms an alloyed region that re-grows epitaxially on the silicon substrate to form highly reflective, ohmic contact of extremely low contact resistivity ($<10^{-4}$ Ω-cm^2) (Sopori et al., 1993).

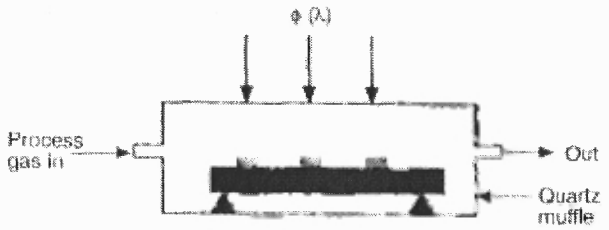

Figure 1.3 Illustration of the use of Optical Processing for simultaneous formation of the front and back contacts.
Source: (Sopori et al., 1993).

The energy delivered to the cell can also produce bulk heating to induce other predetermined thermal effects. The spectrum, intensity, and duration of the incident flux are chosen for the specific application. In contrast, a typical Rapid Thermal Anneal (RTA) is a thermal process that cannot discriminate between the front and the backside of the cell since such a process is completely thermally controlled. In OPF, surfaces of the back Al contacts typically remain shiny and free from the "spikes" and pitting produced by other processes (Cudzinovic and Sopori, 1996).

OPF consists of a quartz muffle that is illuminated from above by quartz-halogen lamps. The optics of the light sources is designed such that the illumination in the process zone is highly uniform (edge to edge uniformity of ± 5°C, at 900 °C on 156mm substrate). Process gases such as Ar, N_2, Forming gas (i.e., 2% H_2 in N_2), and O_2, if required, are regulated to flow through the furnace. The temperature of the sample in the OPF is mainly controlled by light intensity (LI) signals to IR lamps. The light intensity signal (also called as command signal) is given in the range from 0-10 V. The lamp power

controller supplies power to the lamp, corresponding to the light intensity signal. The controller is a single phase, phase-angle SCR (e.g. Silicon Control Rectifier or thyristor) power controller. The controller linearly controls with respect to a command signal, either, the RMS value of the load voltage, the average value of the load voltage, the RMS load current or load power. OPF is completely controlled by a computer. The process parameters (e.g. signal voltage values, N_2 flow rate in muffle) are fed into the computer using Labview® based user interface. OPF has the capability to efficiently remove effluents that are generated during various processes. This rapid process uses much less power, provides uniform light distribution, has high throughput, has minimal effect of the impurities in the ambient gas/gases on the characteristics of the contacts compared to either furnace processing or RTA. The process requires much less power than furnace or RTA anneals. The process requires fewer steps than conventional approaches and results in significant cost savings. The furnace can be used for alloying metal contacts on semiconductors, re-crystallizing thin film silicon, preparing wafer for oxidation and dopant diffusion on silicon wafers to create N+/P junctions. In the current work, the cells were fired by varying light intensity values of controllers to study the effect of temperature uniformity on the cell electrical parameters.

1.5 Characterization Tools and Techniques

In order to analyze the various important parameters (e.g., electrical and optical) of mc-Si solar cells, various electro optical techniques are used. In this section, some of the main techniques that are used to characterize the solar cells are briefly explained. Much of the work for the current research has been devoted to develop a repeatable cross sectional polishing technique. Thus, it will be discussed in detail.

1.5.1 Chemical Mechanical Polishing (CMP)

Cross-sectioning (c/s) of a wafer or a device is done to reveal the structure within its thickness. A number of techniques are used to examine variations in the structure of a multilayer device. Sample preparation for these measurements can be done by depth profiles using step polishing, angle polishing, sputter etching, and cross-sectional Transmission Electron Microscopy (XTEM). In many cases, techniques used for this investigation include Energy Dispersive X-ray (EDX) analyses, Energy Loss Spectroscopy (ELS), Conductive Atomic Force Microscopy (C-AFM), microprobe, optical excitations, and Electron Beam Induced Current (EBIC). For a Si solar cell, the cross-sectional information can be obtained to investigate metallization, back surface field (BSF), defects within the bulk of the cell, and interface characteristics. In many cases, one can cleave the wafer. This approach sometimes works well for single crystal wafers and can be useful for such examination that uses large beam size (i.e., Auger or microprobe analyses). Sample cleaving can produce fracture patterns which can interfere with analyses such as AFM, CAFM, and other high resolution methods. Cleaving can produce very undesirable surface morphologies for a device that has multilayer structure with different materials. Such a structure often has stress that causes stress lines and uneven height variations (Sopori, Mehta, & Knorowski, 2008).

CMP and mechanical polishing have been extensively used in the integrated circuit industry for various wafer processing and preparation steps. This has been adapted to the needs of the photovoltaic (PV) industry, and studies have focused especially on the effects of flat polishing multi-crystalline silicon (mc-Si) wafers for characterization (Sopori, Nilsson, & McClure, 1981). For the purposes of cross-sectional

polishing of a single material wafer, a mounting mechanism that avoids the complications of epoxy by using a low temperature wax is desired and the mechanism must simultaneously provide good support to the sample edge (Sopori, 1982).

More recent work has adapted these techniques for the cross-sectional polishing of a solar cell made of several different materials. It has been shown that polishing parameters such as pressure, slurry flow, polishing time, and edge support need to be carefully controlled in order to obtain a quality edge (Speed, Romero, To, Mountinho, Page, M., & Sopori, 2006). CMP has been extended and developed to cross-section large lengths of wafers/solar cells at any step of the solar cell fabrication process. A variety of combinations of pads, grit sizes, and other polishing parameters were investigated (Sopori et al., 2007).

1.5.1.1 Polishing Procedures. The solar cell to be cross-sectioned is cut into 1.6"x1.6" samples with straight edges, using either a laser scriber or a dicing saw (Disco Automatic dicing saw – DAD-2H/6T). The sample is mounted in a chuck whose photograph is shown in Figure 1.4a. A schematic cut-section of the sample holder is given in Figure 1.4b and described in detail in reference (Sopori, 1989).

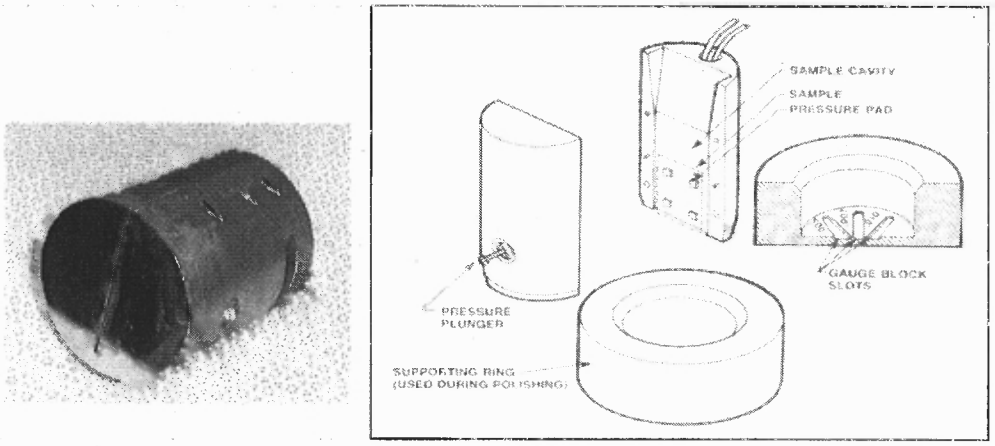

(a) (b)

Figure 1.4 Cross section polishing chuck, (a) Photograph of sample mounting chuck and (b) detailed schematic of the sample mounting chuck
Source: (Sopori, 1989).

To mount the sample, the spring-loaded pressure plunger is pulled out and the sample is placed inside the sample chamber so that it is sitting on top of the four pads with about 0.1 mm protruding from the bottom of the chuck; then the plunger is released to support the sample. Pieces of wax (Crystalbond 509, M.P. of 120 °C) are then introduced to the funnel shaped side of the chuck, which also has two circular openings for the dual heaters (typically 200W power). As the wax seeps out of the bottom of the chuck, it forms a thick layer around the protruding edge of the sample. The heaters are then taken out from the chuck and wax is allowed to cool slowly.

The wax around the sample edge is then leveled with respect to sample edge using a specially modified soldering iron tip and then it is ready for polishing. The wax meniscus mechanically supports the edge and helps prevent rounding and maintain edge quality, as illustrated in Figure 1.5a. A good wax support in the form of a plateau around the front contact and SiN_x is observed in Figure 1.5b. The sample is polished on the CMP

machine (See Figure 1.6). The chuck is placed in a retaining ring that is connected to the rotary arm. The process uses Nalco alkanolamine Si slurry and a scuba 4 polishing pad. The slurry oxidizes the silicon surface and the pad removes the oxide (Sopori, Rupnowski, Mehta, Ewan, 2008). It takes about 2-3 hours to polish a sample.

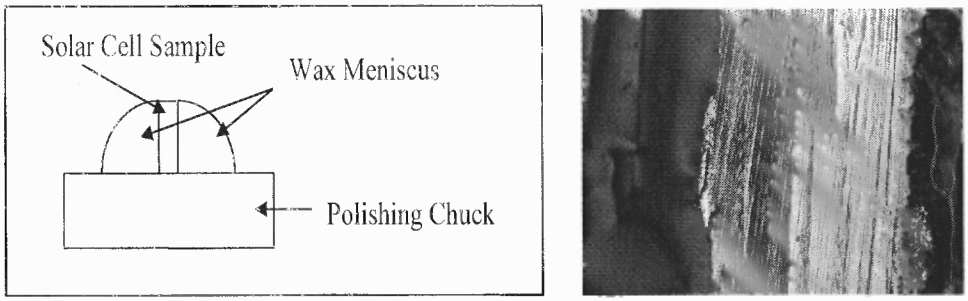

(a) (b)

Figure 1.5 Details of wax support for sample, (a) Schematic of sample protruding out of chuck with wax support, and (b) As-cut sample in chuck after mounting in wax.

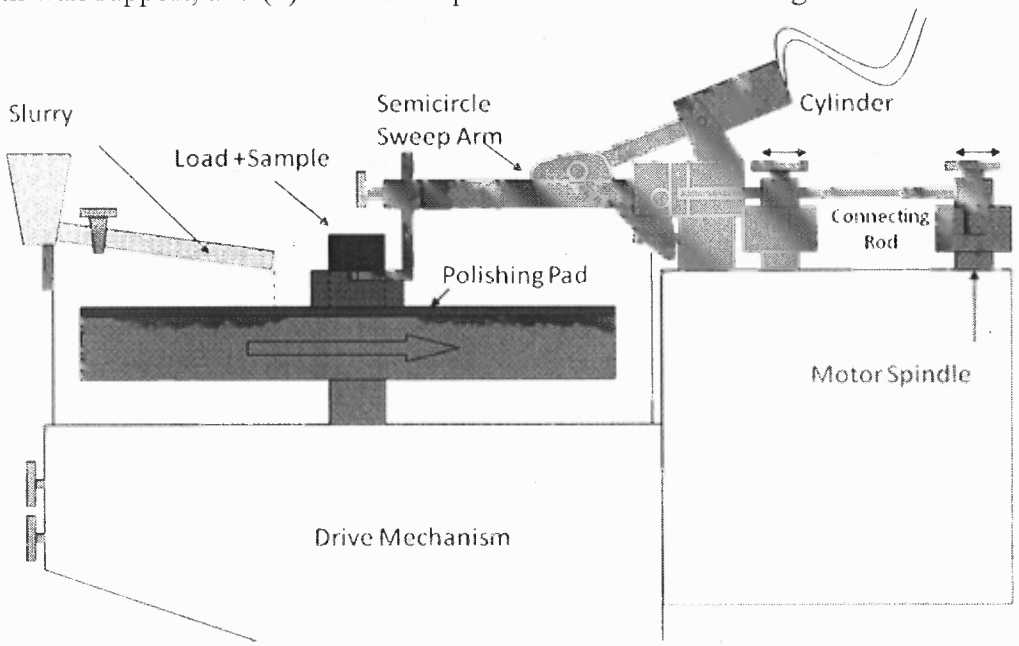

Figure 1.6 Schematic of a CMP machine.

After polishing, the chuck is re-heated (120°C) and wax is allowed to drip out. The plunger is pulled and sample is collected. The wax on the sample is dissolved in acetone, followed by cleaning with isopropyl alcohol. Next, the polished edge is cleaned with q-tip and soap water. Finally, polished edge is rinsed in de-ionized water.

1.5.1.2 Study of C/S Images. Figure 1.7 compares SEM micrographs of cleaved samples with polished samples. Cleaved samples ((a), (c), (e)) have fracture marks and the surface is non planar. Polished ((b), (d), (f)) samples have almost planar surface with no fracture marks. In cleaved samples, cracks will propagate around the silver particles and hide finer details. Cross section (C/S) will polish the particles also and hence a boundary between crystalline and glass layer can be seen (Figure 1.7(b)). On higher magnification (Figure 1.7(e)), artifacts on the cleaved samples can be wrongly interpreted as precipitates of Ag crystallites. In c/s polishing we do not see such artifacts (Figure 1.7(f)). Similar samples of cells fired with under-fired (≈750°C), optimal fired (≈800°C) and over fired (≈830°C) conditions were prepared.

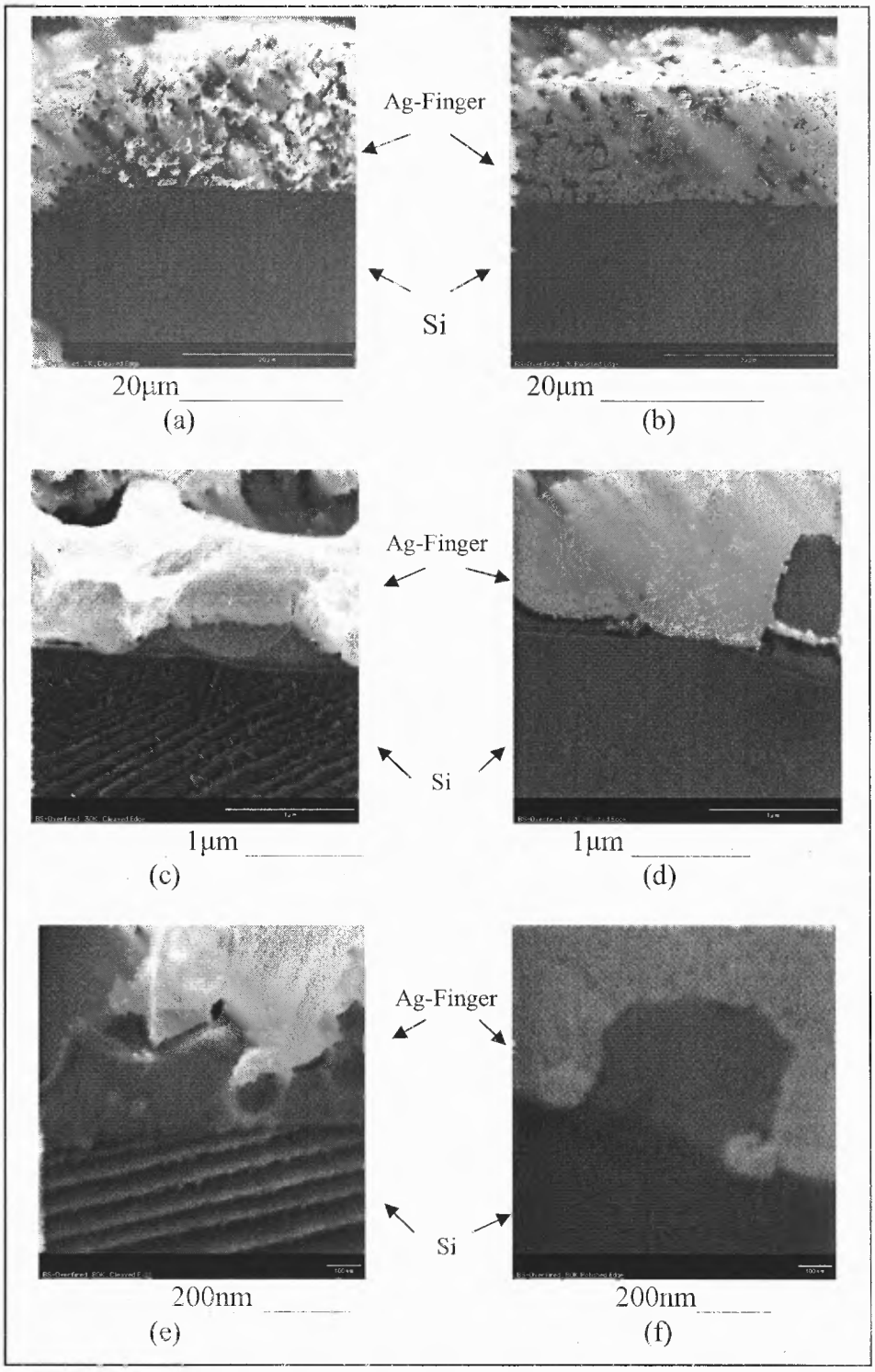

Figure 1.7 SEM comparison of (a, c, e) cleaved samples and (b, d, f) cross-sectioned samples.

Analysis of c/s of these samples helped in understanding front contact formation and current conduction mechanisms. More details are given in Chapter 3. Similar c/s sections were prepared to understand back contact formation. Figure 1.8 (a) and (b) shows a c/s photograph of sintered back aluminum contact. A stratified layer of p-type substrate, Al-Si eutectic and glass trapped in sintered Al particles can be seen. In Figure 1.8(a), a continuous layer of Al-Si eutectic layer can be seen. In Figure 1.8 (b), a close up of Si lamellae can be seen. Figure 1.8 (c) is an SEM image of the c/s polished sample. Agglomerated Al particles can be clearly seen. Dopant contrast SEM can show a p+ region at the Si-Al interface (see chapter 2 for further details).

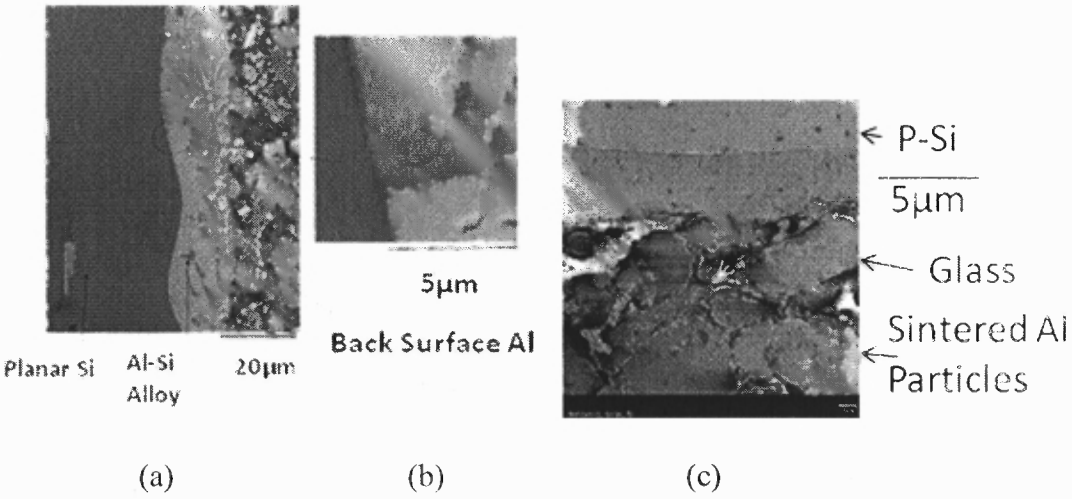

Figure 1.8 Optical image of Back Aluminum and Si/Al alloy under (a) Nomarski filter, (b) Digitally enlarged view of Al/Si Alloy showing lamellar structure, (c) SEM image of c/s back aluminum contact.

1.5.2 Scanning Electron Microscopy (SEM)

SEM was extensively used on c/s samples to study the Ag-Si interaction at the finger-Si interface, Ag and glass distribution within the finger/bus-bar structure and change in glass particle size with increase in temperature. A typical SEM has electron gun, a lens system, scanning coils, an electron collector and a cathode ray display tube (See Figure

1.9). In basic SEM, a beam of highly energetic (0.1-50 keV) electrons is focused on a sample surface. This can produce several interactions including the emission of secondary electrons, backscattered electrons, photons, and X-rays (Schroder, 2006).

Since the bombarding electron beam is scanned in the X-Y plane, an image for each of these different processes can be mapped with a suitable detector. A detector for secondary electrons, standard to all basic SEMs, records topography of the surface under observation. Since SEM uses electrons, large magnification (>400,000x) and higher depth of field is possible. SEMs have a resolution of the order of 1-2 nm. In addition, information on composition, phase, electrical, optical, thermal, and other properties can be mapped with excellent resolution with appropriate detectors (Schroder, 2006).

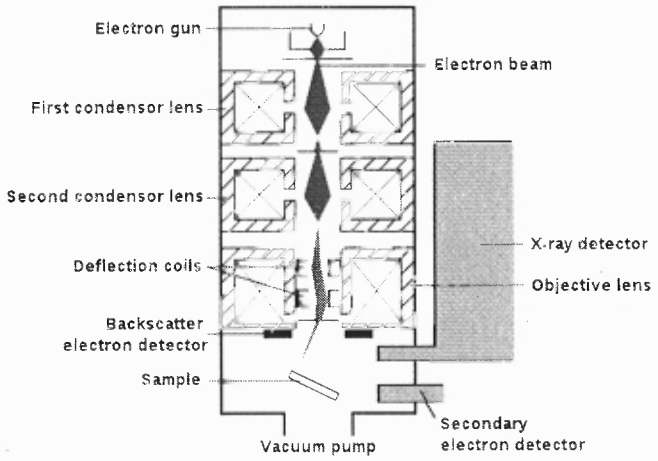

Figure1.9 Schematic diagram of SEM.
Source: ("Schema MEB (en).svg.," 2010)

1.5.3 Conductive Atomic Force Microscopy (C-AFM)

Conductive AFM is operated in contact mode AFM. In the present study, it was used to characterize front silver silicon contact structure. Conductive AFM is used for collecting simultaneous topography imaging and current imaging. Variations in surface conductivity can be distinguished using this mode (sensitivity 2pA to 1μA). The contact tip is scanned

in contact with the sample surface (Figure1.10). While the z feedback signal is used to generate a normal contact AFM topography image, the current passing between the tip and the sample is measured to generate the conductive AFM image. The sample is held at ground potential (Schroder, 2006).

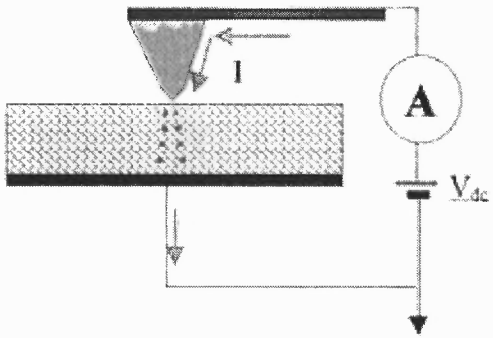

Figure 1.10 Schematic of operating principle of Conductive AFM.
Source: ("Conductive AFM option," 2010).

1.5.4 Scanning Kelvin Probe Microscopy (SKPM)

SKPM was used in this work to study the surface potential of the front silver contact and silicon surface. In this method, unlike Kelvin method, forces are measured instead of currents [Nonnenmacher, O'Boyle, & Wickramasinghe, 1991). SKPM measures two-dimensional distributions of contact potential difference (CPD) between the tip and the sample with resolution in the 100 nanometer range. The CPD can be converted to the work function of the sample if the measurement is performed under thermally equilibrium state; and it can be converted to an electrical potential when the sample is illuminated or a bias is applied to the sample.

In SKPM, the AFM system operates in non-contact mode, and a conductive tip is oscillated at the first resonant frequency of the cantilever over the sample surface as it is scanned laterally. The topographic data is taken by controlling the atomic force between

the tip and the sample. In addition to the atomic force, a long-range electrostatic force also exists between the tip and the sample, which is determined by the CPD between them. The electrostatic force is detected by an ac voltage to the tip and using a lock-in amplifier. The ac voltage frequency is set at either the second resonant frequency of the cantilever or a low frequency (~20 kHz) that is far off the first resonant frequency, in order to avoid the interaction between the topographic and electrical signals. The electrostatic force is zero when the CPD is completely compensated by a dc voltage applied to the tip. In this case, the CPD is equal to the applied dc voltage (Schroder, 2006).

1.5.5 Secondary Ion Mass Spectroscopy (SIMS)

Dynamic SIMS (Figure 1.11) was carried out on the c/s silicon solar cells to determine the phosphorous doping profile below the finger, before and after the firing and to determine Si diffusion in Aluminum. Ag finger was etched of prior to measuring SIMS data. SIMS is a highly sensitive technique and utilizes less amount of sample. Higher energy (10-20KeV) ion flux (O_2^+ or Cs^+ ions), with diameter of less than 10 μm is used in dynamic SIMS. Beam sputters away at the surface of the sample, and steadily buries deeper into the sample and generates secondary ions that characterize the composition at varying depths. Ion yield changes with time as primary particles build up on the analyte effecting the ejection and path of secondary ions.

In dynamic SIMS, the intensity of one peak for one particular mass is recorded as a function of time as the sample is sputtered at a higher sputter rate (~10μm/hr), yielding a depth profile as in dopant profiling. SIMS can detect dopant densities as low as $10^{14}cm^{-3}$ (Schroder, 2006). It can simultaneously measure several elements and has a depth

resolution of 1 to 5 nm. It analyzes ionized atoms (e.g. 1% of the total) by passing them through a mass spectrometer. SIMS is expensive and cannot differentiate between total and electrically active impurities. Continuous analysis, while sputtering, produces information as a function of depth, called a depth profile.

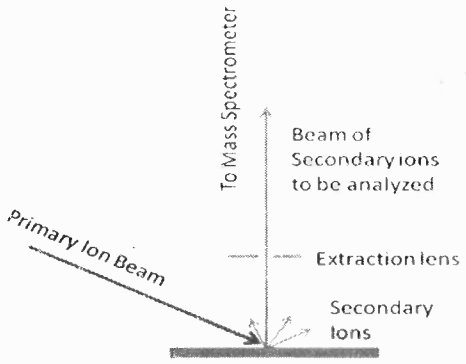

Figure 1.11 Schematic of working principle of SIMS.
Source: ("Schematic Depiction of Sims Source Region," 2010).

CHAPTER 2

THICK FILM METALLIZATION OF mc-Si SOLAR CELLS

In this chapter, thick film metallization is introduced and its important role in contact formation and current conduction mechanisms of mc-Si solar cell is emphasized. First, a brief evolution of contact metallization of mc-Si solar cells has been presented. Some challenges of these methods have been highlighted. An overview of some new and upcoming metallization techniques is given. This is followed by a detailed discussion of screen printing technique. Advantages and limitations of screen printing method are presented. Composition of the conductive metal paste and roles of its various constituents have been explained. Next, basic concept of fire-through contact metallization has been given. Concept of Front and back contact formation mechanism, and hydrogen passivation is briefly presented.

2.1 Early Metallization Techniques in Silicon Solar Cells

In the 1950s, electroless Ni plating was used to prepare metal contacts on space solar cells (Iles, 2001). In the 1960s, metallization on Si solar cells was done by vacuum evaporation using metal shadow mask (Green, 1993). Initially Ti/Ag layers were used to collect carriers and later on Ti/Pd/Ag (i.e. metal stack structure) was used for metal contacts. Ti reacts with silicon and forms low resistance (10^{-5} Ωcm^2) contacts. Pd was used as a diffusion barrier. Pd also increases corrosion resistance and thereby prevents peeling of the contacts during temperature–humidity testing (Iles, 2001). Silver (i.e., 4μm thick) is used as conductor. Certain high efficiency laboratory solar cells (e.g., Passivated Emitter Rear Locally diffused (PERL) cells) still use same stack structure. In 1973, Lindmayer & Allison introduced photolithography (which was already being used in

microelectronics) to replace contacts made by vacuum evaporation. This technique allowed for finer grid and shallower doping of the emitter. The contacts made by photolithography have minimum series resistance and good shunt resistance resulting in lower power loss. It has advantage of 2% absolute efficiency over screen printed contacts (Doshi, Mejia, Tate, & Rohatgi, 1997).

Until the mid 70s, the bulk of solar cells were made for space applications and terrestrial solar cells were still prohibitively expensive for the general public. The techniques used were time consuming and metals selected were costly. In 1975, Si solar cells were introduced with screen printed metal contacts, having gridded Ag based front and Al based whole area rear contacts (Ralph, 1975). The self aligned nature of these screen printed contacts made them cheaper to manufacture. In 2006, 86% of Si solar cells had screen-printed front and back metal contact (Neuhaus & Munzer, 2007).

The size of the individual solar cell during 1970s-1980s was $4cm^2$. Later, as the solar cell size increased to $100cm^2$, and as photovoltaic technologies improved (i.e. increased carrier lifetime, better light trapping design, good surface passivation layer), problems with screen printed solar cells became prominent. As efficiency of the solar cells increased from 4% to 16.5%, the contact metallization became a technological bottleneck. However, the efficiency difference between screen printed cells made from high lifetime Czochralski wafers and cast mc-Si wafers is only 1.5% (Neuhaus & Munzer, 2007).

Current conventional Si cells with 125 mm and 156mm sizes, suffer from lower fill factors (<78 % FF). Screen printed contacts are supposed to make near ohmic contacts ($\rho_c = 10^{-7}\ \Omega\text{-cm}^2$) with the Si solar cell to efficiently collect the light generated

charge carriers from the cell. However, screen printed cells have glass as additive in the paste. Presence of glass at the metal-Si interface can increase the contact resistance. Increased interfacial and lateral resistance (i.e., line resistance) of the contact reduces the FF, preventing solar cell from achieving optimal performance (85% FF). To overcome limitations of screen printed contacts, new techniques have been proposed. In the next section, we will review some of existing and promising new deposition techniques.

2.2 Thick Film Deposition Techniques

Thick film (>5μm thick) contact deposition techniques can generally be divided into single run or multi-run process. In the following description, single run techniques are defined as those that deposit paste on the substrate only once. Multi-run techniques are described as those in which metal is being deposited on the substrate, on the same place, more than once (i.e. multiple layer). These have advantage of fine line resolution (better finger width control through slower paste deposition rates), but costly equipment and slower cost recovery for industry.

2.2.1 Single Run Deposition Processes

Screen printing is the most widely used state of the art metal contact deposition technique in the mc-Si solar industry. It has been adopted from the microelectronic industry. In this process, conductive metal based paste is deposited in a desired pattern on SiN:H coated mc Si solar cell using a metal screen. It is a contact method and pressure is applied on the wafer by squeegee via a screen. The screen printing technique is explained in detail in Section 2.2.

Screen printing has certain limitations such as (i) Large shadow loss (7-10%) as narrow (<80μm wide) and thicker (>35μm) fingers are difficult to deposit simultaneously, (ii) Emitter doping has to be kept high (i.e. <50Ω/□ sheet resistance, ≈ 2E+20 atoms/cm^3 dopant concentration at the surface), (iii) High contact resistance (>4mΩcm^2) and line resistance. To overcome these limitations, researchers have suggested different techniques. These will be presented in the following section.

Stencil Printing is a precursor of screen printing technique. It is widely used in printing circuit boards. However, in solar cells, textured surfaces erode the life of the stencils. It is being improved to overcome aspect ratio (i.e. line height/line width) limitation of screen printing technique by using heated (80-90°C) wafer (Erath et al., 2010).

Syringe printing deposits metal paste using syringe. It is useful for depositing on mechanically textured surfaces (Huster et al, 2000). Multiple syringes can be used to simultaneously deposit several rows of fingers. The rhelogy of the paste and the paste depositing mechanism has to be carefully designed. Fingers with higher aspect ratios can be deposited. It is used mainly in laboratory environments.

Hotmelt ink process was developed at Frounhofer ISE Germany (Mette, 2007). The paste composition is different with higher amount of silver (>80%) compared to regular screen printed paste (70-80%). The paste is solid at room temperature. Major devices that come in contact with the pastes are therefore heated (i.e., screen, squeegee). Deposited finger has better aspect ratio than finger deposited by regular paste. More details of this technique can be found in (Mette, 2007). This technique is not widely used industry.

2.2.2 Multiple Run Deposition Processes

Ink jet printing technique can be used to deposit metal on substrates in the form of fine droplets (Teng & Vest, 1988). Stress on the wafer is eliminated, as it is a non contact method. Constant height is maintained between printing head and wafer, as the printing head moves with respect to wafer. To facilitate passage of ink through a small orifice, it uses less amount of silver than a screen printed paste. To have a thicker finger, printing head has to pass through the same point, multiple times. The improvement in aspect ratio of finger is also minimal. While it is commercialized for organic PV cells, for mc-Si solar cells, it has to overcome some challenges such as high contact resistance and higher line resistivity.

Roller printing is another two step process developed by Huster et al. in 2000. A beveled single blade is used to create finger ridges on the cell. A roller is then used to apply the screen printed paste. The technique is still under developmental stage.

In 2006, Glunz et al. have proposed the two layer process. In the first step, a narrow metallization line, i.e., the seed layer is created on the silicon surface. This layer creates a good mechanical and electrical contact to the silicon surface. This is followed by a growth step whereby, printed line is thickened by silver electro-plating to increase the line conductivity. Additional details are discussed below.

Pad Printing is one of the proposed seed layer process. It is a widely used process for printing small size patterns (50 micron). It is a contact method. A pad is used to transfer patterned paste from photopolymer plate onto the cell. The paste has similar composition as screen printed paste, but lower viscosity. The photopolymer plate used in this process has short life and erodes fast (Mette, 2007). Paste transfer from ink reservoir

to cell via pad has to be quick or else, incomplete paste transfer occurs. The process is not being currently used in the Si solar cell industry. To improve the paste transfer efficiency, the hot melt ink with heated pad and printing plate are used (Huljic, 2006). In another non contact method, i.e., the seed layer technique, a powder of metal particles is deposited on the surface of the cell. The metal powder is then sintered or melted by laser to form the contact lines. Pulsed laser is used to prevent the rest of the substrate from heating. The remaining powder is removed. This technique is still under developmental stage.

Metal Aerosol Jetting is another non contact, seed layer technique that is being developed. A metal aerosol is conducted through a specially designed printing head. In this printing method, the particles are surrounded by a ring-shaped gas flow which prevents contact between the aerosol and the tip. The aerosol spray is therefore, controlled by the ring-shaped gas flow and line widths considerably smaller than the tip diameter can be deposited. The process is still under development (King, O'Reily & Barnes, 2009).

Light-Induced Electro-Plating is the suggested method to be used for increasing the finger thickness of above mentioned multi run methods. It is selective and a high deposition rate process (Glunz, Knobloch, Biro, and Wettling, 1997). The cell is immersed in a potassium silver cyanide electro-plating bath with an Ag-electrode as anode and solar cell acting as a cathode. Only back Al side of the cell is contacted. The applied potential suppresses dissolution on this side. By illuminating the cells, the front electrodes on solar cell are on a more negative potential, high enough to stimulate deposition of Ag ions (Mette, 2007). This process is explained in Figure 2.1. A new cyanide free bath is being tested by Q-cells.

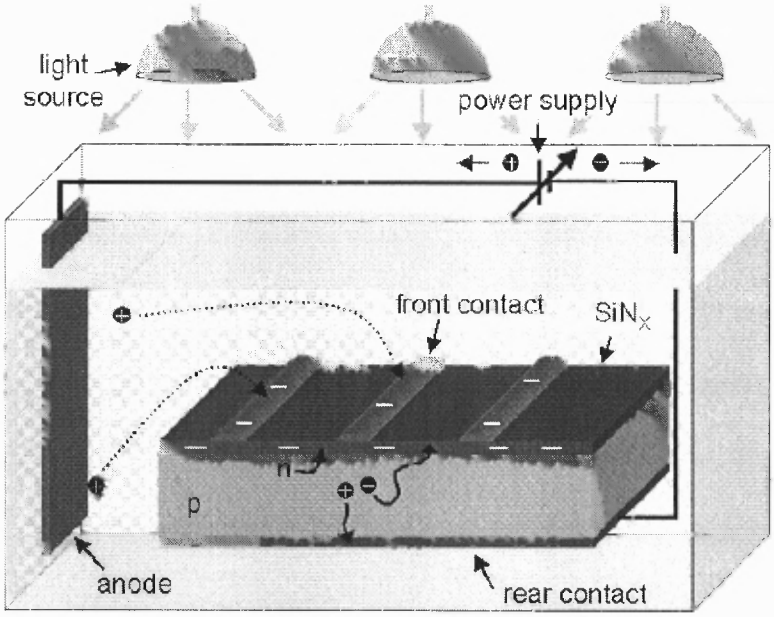

Figure 2.1 Schematic of LIP process.
Source: (Mette, 2007).

The above mentioned multiple run processes require a lot of expensive and state of the art equipment when compared to screen printing. Additionally, material wastage is also an issue. Moreover, the electroplating step is applied after contact firing and can introduce more contaminants thereby affecting the efficiency. Hot melt ink method mentioned in the pad printing step itself is still a developing process. The mechanical adhesion of metal grid on solar cell is an issue.

2.3 Screen Printing

Screen printing is one of the oldest forms of graphic art reproduction (Prudenziati, 1994). Screen-printing is a rapid (i.e., single production line can have throughput of about 1000 wafers/hour), repeatable and an economical technique for applying thick metallic films to a substrate. As mentioned before, Ag-based pastes (or inks) are used for the front contact and Al-based pastes for back contact formation.

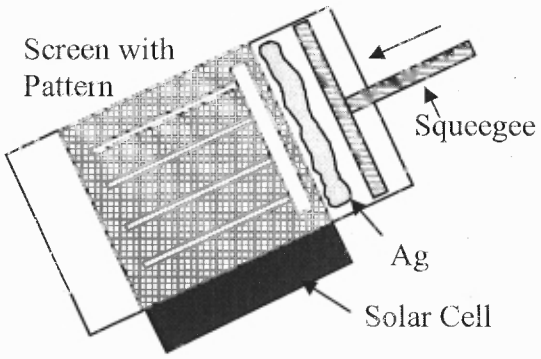

Figure 2.2 Schematic of a typical screen printer set-up.

As illustrated in Figure 2.2, the screen consists of an aluminum frame and a woven mesh of steel wires clamped to the frame. As an alternative, polyester or polyamide can also be used as wire mesh. Screen mesh size is usually 250-325 wires per inch with wire diameter of around 10μm and mesh opening of around 30 μm. The size of the frame needs to be large enough so that the paste releases from the mesh on to the substrate during the snap-off. Steel wires are coated with photosensitive emulsion (0.0015-0.020 inch thick). Photolithography is used to create patterns (openings) that are similar to solar cell grid. The spring loaded squeegee can be made of metal, neoprene or polyurethane. The edge squeegee makes a 45° angle with the screen. By keeping cross section of squeegee as a rectangle, all edges can be rotated periodically.

During screen printing process, the open areas of the screen are flooded with paste by moving a squeegee over the surface of the screen without applying a vertical force. The screen is not touching the wafer, but is at a certain distance away from it; this distance is called snap off distance (i.e., 0.5 mm). Next, a vertical force is applied to the printing-squeegee, pressing the screen onto the wafer and forcing paste through the screen openings. The paste sticks to the substrate due to adhesion forces. In the final phase, the paste is released out of the screen.

For solar cell metallization, screen printing is applied in different steps. Initially two bus bars are printed using Ag/Pd paste onto the back (i.e., solder tab cannot be placed on Al layer) of the solar cell, followed by printing the remaining area with Al paste. Cell is dried (100-200°C) and front Ag paste is printed after flipping the cell.

The rheology of the screen printing paste is one of the most critical properties. Initially, while on screen, paste is expected to be highly viscous. Then on the application of shear force by the squeegee, it is supposed to flow through the screen and onto the cell. As squeegee pressure is removed, it is again expected to become a viscous paste to maintain desired print thickness and width. Hence, thioxotropy and rheology of the paste are considered invaluable properties. Figure 2.3 shows change in viscosity with time at

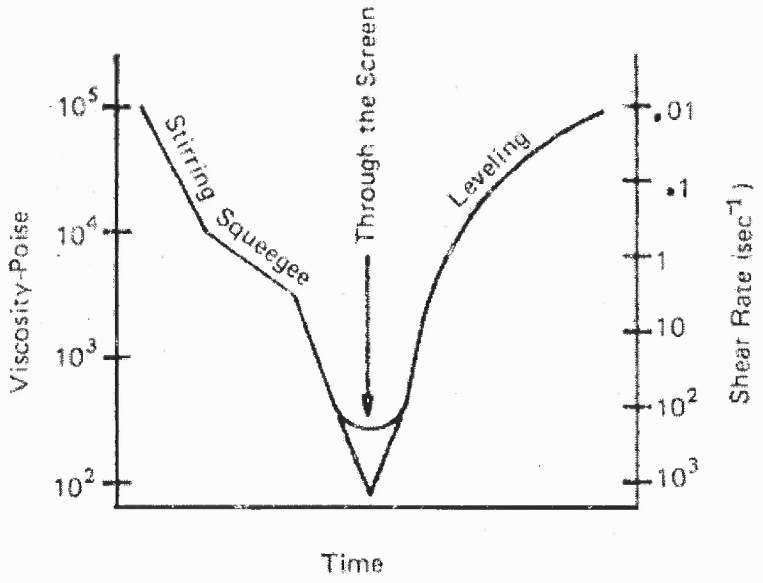

Figure 2.3 Change of paste viscosity with time.
Source: Hybrid Microcircuit Technology Handbook (2nd Edition), By: Licari, J.J.; Enlow, L.R. © 1998 William Andrew Publishing/Noyes.

applied shearing rate. The quality of the print image depends mainly on the screen, the paste, photo emulsion and on the printing parameters such as (i) snap-off distance between screen and cell (e.g., 1-3 mm), (2) printing speed (maximum of 300 mm/s), (3) squeegee and squeegee pressure (maximum of 13 kg). Screen printing has been accepted widely by the industry. But it has its drawbacks:

- Screen mesh size limitation requirements prevent finer fingers (<60 micron) and bus bars. This leads to shadowing loss (up to 7-10%). It also has poor aspect ratio (i.e. height to width ratio) of ≈ 0.17.
- The top layer of the cell has to have a high doping level so that the contact formation is near ohmic. High doping level leads to less response for short wavelength light (e.g. blue light).
- Glass (5-8%) in the paste affects contact formation and current conduction. The contact formation is through islands of silver and silicon. Thus the process is not efficient enough.
- The back contact aluminum requires additional Ag/Pd soldering pad leading to additional screen printing step.
- Front Ag/back Al pastes have organic compounds which give out fumes that interfere with processing as well as pose environmental hazards. These hazards are mitigated by utilizing expensive exhaust systems.
- Solar cell is subjected to a notable pressure during screen printing. Weak wafers or thin wafers can create cracks which may result in shunt if metal paste is covering the crack.
- Screen slowly becomes deformed and wears out with usage.

2.4 Thick Film Metal Pastes

In the next section, details of composition of front silver based and back aluminum based pastes are given and their functions are discussed. Various ink manufacturers (i.e., Ferro, DuPont, ESL) have proprietary compositions that can vary to accommodate requirements of cell manufacturers. Pastes are designed to meet many requirements such as: (i) good

thixotropy (defined as a full-bodied material which undergoes a reduction in body when shaken, stirred or otherwise mechanically disturbed and which readily recovers the original full body condition on standing (Mette, 2007)) and rheology (i.e. flow behavior) to facilitate ease of transfer of paste from screen onto a desired pattern on solar cell, (ii) provide mechanical adhesion with minimum stress (i.e., the thermal expansion coefficient gradient between paste and Si substrate should be as small as possible) that can withstand cell handling and module manufacturing process.

2.4.1 Front Contact Pastes

Silver paste is composed of many ingredients that undergo a variety of interactions during firing to yield required electrical (i.e. low conductivity =3-30μΩcm, low contact resistance between metal-semiconductor = <0.3Ω), mechanical (e.g., low stress on substrate), and thermal (e.g., closely matched thermal expansion coefficient between finger and silicon) properties. In general, the paste consists of three major constituents: (a) a fine powder of Ag, (b) a glass frit, and (c) an organic binder. Although Ag is the primary metal in the contact formation by Si-Ag alloy, other constituents (i.e. glass frit and solvent metal) play an important role.

2.4.1.1 Silver Particles. Silver particles are most commonly made by chemical reduction of silver nitrate solution in the presence of hydrazine hydrate (i.e. reducing agent), ammonia complex agent and gelatin (protective agent) (Yiwewi, Yunxia, Shuanglong, Lihua & Guorong, 2007). Silver precipitates thus formed are treated with surfactants such as Triethanolamine (Boiling Point (B.P.) = 335°C) and Caprylic acid (B.P. = 239°C) to improve their surface characteristics. The surface area and the tap density are important parameters affecting their behavior. The surface area of the

powders plays a major role in the rheology of the paste. The higher the surface areas, better the screen ability of resultant paste. Surfactants help the transfer of ink from the stainless steel mesh to the wafer. They improve the wetting characteristics of the silver particles. This helps molten glass to cover the silver particles thoroughly. They also improve the pseudo plasticity. Surfactants also increase the stability of the silver paste thereby increasing the shelf life. Ag particles are 0.1 to 0.3 μm in size (mainly spherical shaped Ag particles are used, but mixtures of various shapes can also be used to improve packing density). Silver paste has 65-75 wt % Ag particles.

2.4.1.2 Glass Frit. As mentioned previously, solar cells have antireflection coating of SiN:H. During solar cell contact firing process, Silver does not react with SiN:H (Young & Carroll, 2000), hence SiN:H must be dissolved before Ag can come in contact with Si. SiN:H dissolution is accomplished by adding glass frit to ink. The glass frit softens into a liquid at 550°C (Prudenziati, Moro, Morten, Sirotti & Sardi, 1989) and helps to dissolve/etch the SiN:H layer and bring Ag particles in contact with the Si interface. Lead borosilicate is a widely used glass for contact metallization of solar cells. Lead free borosilicate glass is also being explored mainly due to strict EU RoHS guidelines and to be consistent with green image of the solar cell. Leaded/unleaded borosilicate glass has been well studied by the glass industry (Prudenziati et al., 1989).

Although used in lesser amount (5-8%) in paste, compared to Ag, glass plays a number of important roles as follows: (1) glass provides mechanical strength to the finger and bus-bar (required during wafer handling and soldering of the contact leads during module packaging), (2) glass reduces bow in thinner wafers (<150 microns), (3) glass dissolves (i.e. etchs) SiN_x:H and (4) glass influences Ag contact formation and current

conduction process. To accomplish these tasks, various additives are introduced in the glass. They can be oxides of Pb, Bi, Zn, Sn, B, Al, Mn etc. There can be two or more of these oxides present in a given paste. The B and Al oxides increase the mechanical strength. Bi oxide can be reduced to form Bi ions (through forming gas annealing or Si) which can help in the tunneling conduction mechanism (Gzowski, Murawski, & Trzebiatowski, 1982). Zn and Sn are believed to be used as replacement for Pb which is considered a health issue. ThO_2, Gd_2O_3, NiO are added to the metallization to minimize the shrinkage mismatch with the dielectric during co-firing by delaying the early sintering of the metallization to higher temperatures so as to more closely match that of the dielectrics. The cumulative effect of all of these oxides on one other or on the contact formation mechanism is difficult has not been studied in a realistic manner.

Paste manufacturers vary the glass transition temperature (T_g) to achieve some of the above mentioned properties. For example, modifiers in the glass can fluidize glass quickly and crystallize faster after cooling to affect the Ag-Si direct contact (Hilali, 2005). The glass can also be made aggressive depending on the emitter doping level (i.e., junction depth).

Reactions between Ag and Si at relevant processing temperature ($<835^0$C) are negligible (Figure 2.4(a)). It requires a solvent metal such as Pb, Zn, or Bi to lower the temperature of interaction between Ag and Si. This solvent metal comes from glass frit. Details of Ag-Si and Ag-Pb systems are available in the literature (Massalski, 1992). To get an idea of role of glass frit composition, Figure 2.4(b) shows sketch of phase diagram of Ag-Pb-Bi (Kattner, 2003). Sopori et al., in 2007, proposed that Ag particles and Ag agglomerates can interact with solvent metal (M) such as Pb (and more recently Bi) to

form a thin surface of Ag-Pb or Pb-Bi alloy. Such an alloy can lower the melting point of Ag. For example, only about 20% Pb or Bi is needed to interact with Ag to lower the melting point to less than 800^0C. As previously stated in this section, various metals and metal oxides are present in close vicinity at high temperature for a few seconds. While phase diagrams can give a general idea of possible reactions, one has to go beyond them to understand the contact formation mechanisms.

To prepare a desired glass frit, any of the before mentioned additives are mixed with the molten glass. Glass is than solidified as sheet. This glass sheet is crushed (using ball mill) and mixed with the silver paste. The size of glass particles is few microns (i.e. 3-8 μm). Glass frit can also increase the contact resistivity. They are usually found between the finger and the silicon surface. Thus, their effect cannot be neglected. By nature, they are non conductive. Glass frit has a resistivity of $10^9\Omega$cm (Ballif, Huljic, Willeke, & Wyser, 2003).

2.4.1.3 Organic Solvents/Binders. A solution of ethyl cellulose in α-terpineol (2-20 wt %) is commonly used as solvent. B.P. of Terpineol is 220°C. Different manufactures may use other solvents. Solvents give the silver paste its green strength (i.e., as deposited, unfired strength). This property decreases the wear of thin finger during transfer from one machine to another. Organic solvents also disperse metal and glass frit, and improve rheology of the paste.

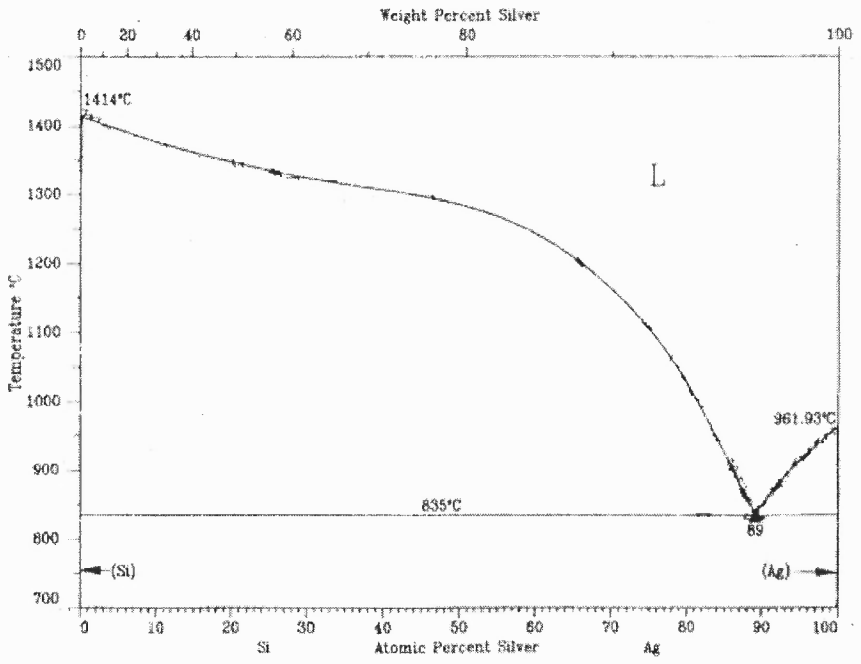

(a)

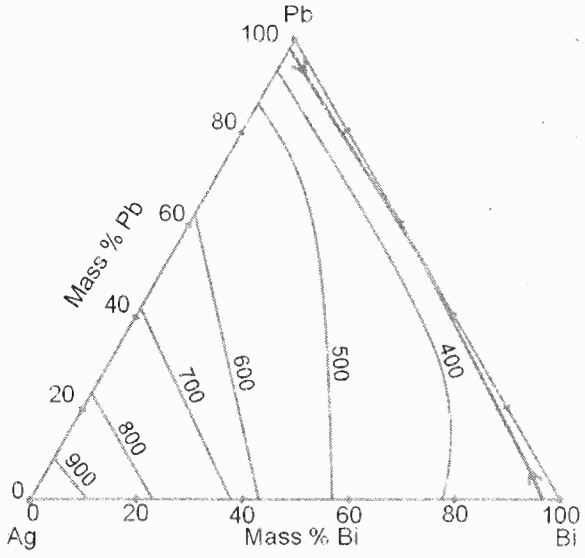

(b)

Figure 2.4 (a) Modified assessed Phase diagram of Ag-Si system, (b) Ternary Phase diagram of Ag-Pb-Bi.
Source: (Olesinski, Gokhale, & Abbaschian, 1989), (Kattner, 2003).

2.4.2 Back Contact Pastes

The Al paste consists of Al particles from 1-10 μm size (70-80 wt %), similar sized glass frit (5-8wt %, PbO, Bi_2O_3, B_2O_3, ZnO, used for adhesion) and organic solvents and binders (15wt%, to control the rheology of paste). About 7-10 mg/cm^2 Al paste is screen printed on the back side of the cell (Huster & Schubert, 2005). It is difficult to solder back Al layer; hence, additional contact pads of Ag/Pd are screen printed on the back side. More detailed explanation of the functions of Al paste and its role in back contact formation is explained in Section 2.5.2.

2.5 Fire-through Contact Metallization

Fire-through contact metallization is the most common method in the industry to form metal contacts on a silicon solar cell. It is cheap, fast and a high throughput process (1000-2000 wafers/hr). Higher production rates can be achieved by using multiple lines in parallel. As with the rest of the photovoltaic technology, it is borrowed from thick film circuitry techniques of the microelectronics industry.

In this process, a n+/p mc-Si solar cell coated with about 750 Å thick SiN:H antireflection film is the starting material (See Figure 2.5a). A front metallization pattern consisting of Ag-based ink is then screen printed on top of the SiN:H layer of a silicon solar cell. An Al-based contact is also screen printed on the back side of the cell so that both contacts can be co-fired (Figure 2.5b). Next, the cell is fired in an infrared (IR) belt furnace in which the cell experiences a temperature profile that typically peaks at about 800°C (Figure 2.5c). During firing, silver paste etches SiN:H, and brings Ag in contact with underlying silicon (hence the name = "Fire-through"). Interaction of Ag particles with Si results in creation of front contact at the front Si surface (Figure 2.5d). Low

resistance ($<10^{-4}\Omega cm^2$) contact is also formed at the back side due to Al-Si alloying. Furthermore, during this step, H from the damaged layer between the SiN:H and Si diffuses into the bulk of the cell passivating impurities and defects (Sopori et al., 2004).

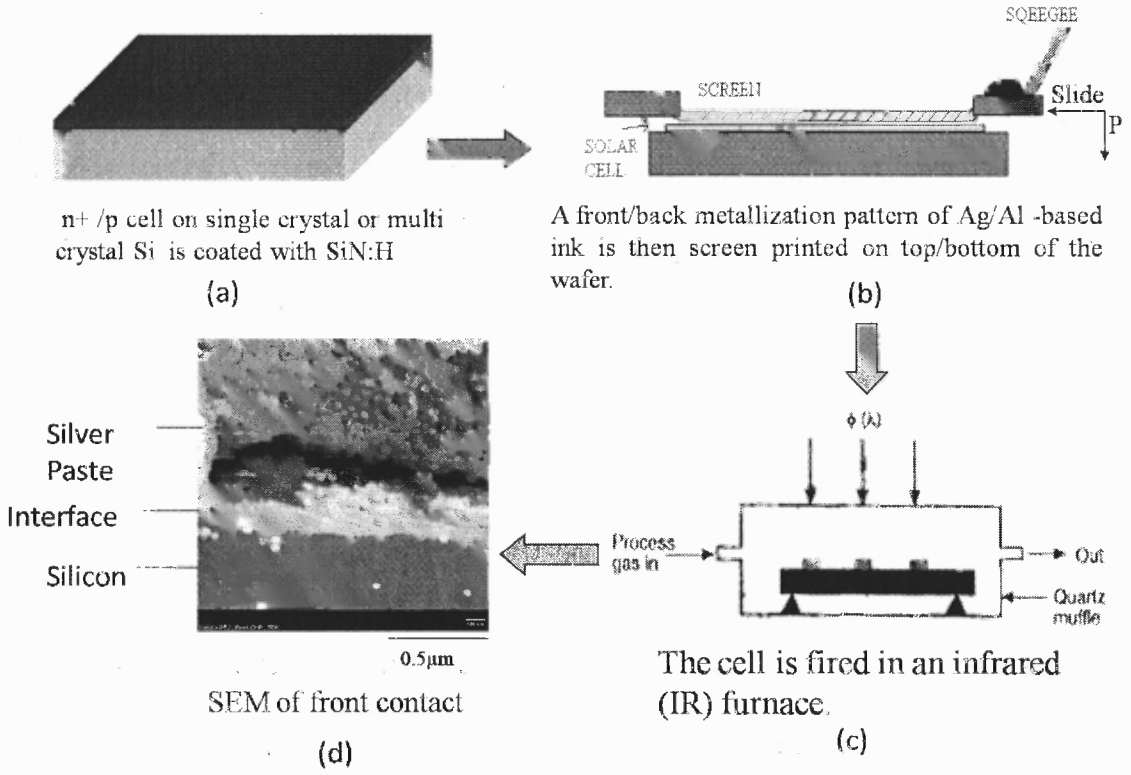

Figure 2.5 Schematic of fire-through contact metallization process.

To develop more detailed understanding of the processes occurring during fire-through contact metallization, different firing profiles were prepared. Figure 2.6 shows a typical firing profile. Three sections in the temperature range indicate phenomenological stages that an ink encounters to end up as a good contact. Stage (a) corresponds to baking in a temperature range of 300°–450°C. Here, the organic binders evaporate and the ink pattern densifies. Although the industry empirically arranges the belt speed and temperature profile of IR furnaces to ensure that all the volatile material has evaporated, experiments performed in current study showed that typical ink dries in 15 min when

baked at 400°C. Stage (b), between 500°–550°C, leads to softening and melting of the glass frit. It has been mentioned before that the molten frit attacks and dissolves SiN:H. Stage (c) consists of a temperature between 551°C and about 800°C and the cool-down. Although all the stages are critical for good contact formation, stage (c) is the most complex step. There has been significant research into the potential mechanisms that occurs in this process. In stage (c), Ag particles interact at the Si surface and lead to the formation of a Si-Ag alloy (Sopori, 2007).

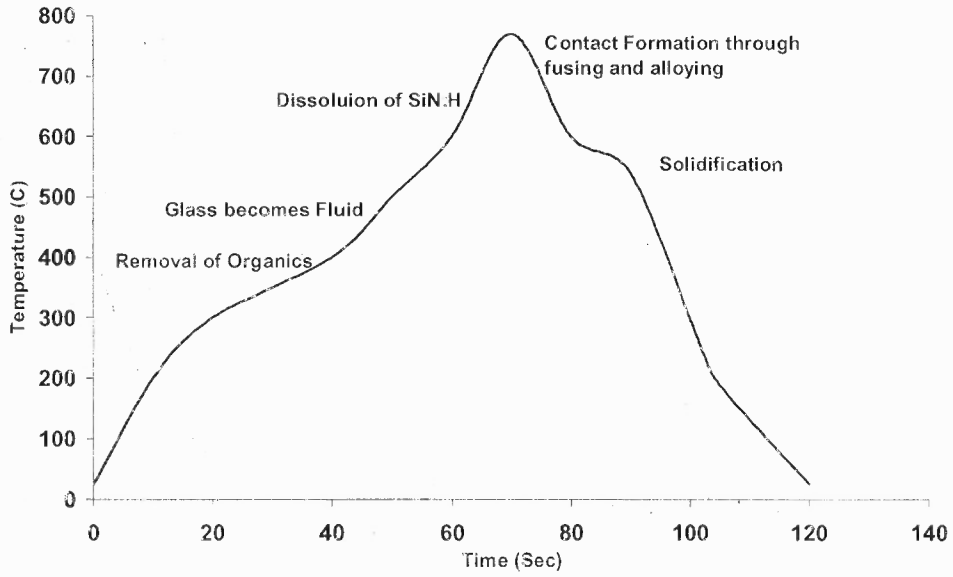

Figure 2.6 Schematic of a typical solar cell firing profile.

Thus, optimization of contact formation involves the synergism of three processes:

1. Front-contact formation to produce a uniform, low-resistance, ohmic contact with high shunt resistance. Such a contact will produce a high open-circuit voltage (V_{oc}) of 680mV and high fill factor (FF) of 85%.

2. Diffusion of Hydrogen deep inside the material and association of Hydrogen with impurities and defects to passivate them. Good bulk passivation will yield a high short-circuit current density (J_{sc}) of 35 mA/cm^2 and high V_{oc}.

3. Formation of Si-Al alloyed region on the back side to produce a large p+-p field, which can lead to a low surface recombination on the back side with a concomitant high V_{OC}.

Metallization firing influences each of the functions differently; hence, maximizing cell performance only reflects a compromised optimum. For example, a mild firing may lead to the formation of a good front contact, but may not diffuse H deep into the bulk. Likewise, a strong firing is required to form a good back-surface field (BSF), but it can cause shunting of the front junction and out-diffusion of Hydrogen. One approach to maximizing the cell performance is to tailor the parameters of the SiN:H, front-side ink, and back-contact ink so that each of these functions can be maximized by the same firing cycle, i.e., temperature-time (T-t) profile. Therefore, it is important to study the details of all three of these phenomena and examine how one can select a suitable choice of inks and processes that can maximize cell performance.

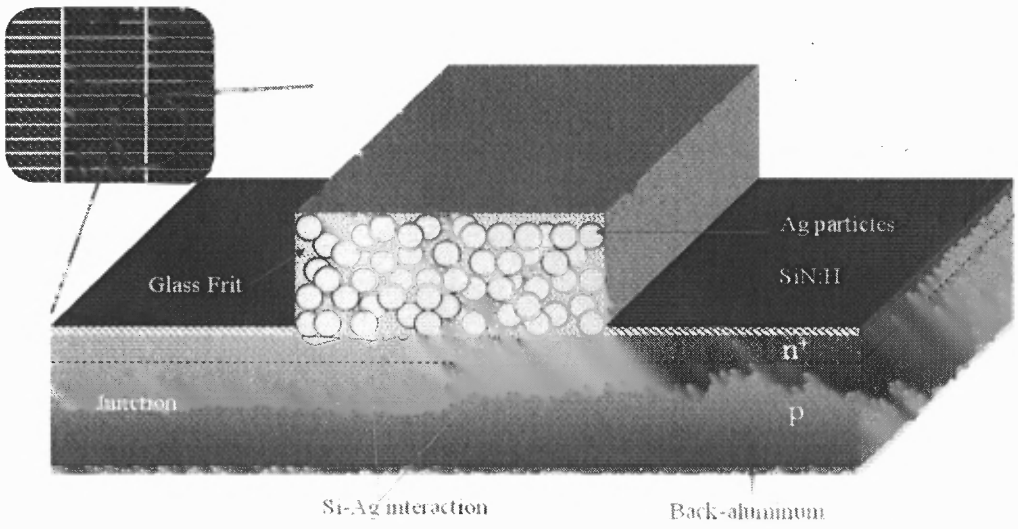

Figure 2.7 Schematic of cross-section of Si solar cell.

Figure 2.7 is a close up schematic of various constituents in a fire-through contact metallization. It can be seen that the silver finger has dissolved SiN:H and is in contact with the Si wafer. The amount of Ag particles is more (≈60-70%) than shown. The depth

of n+ layer is usually 0.3-0.5μm. Figure 2.7 also shows that only a small part of the finger (few microns) actually takes part in the Ag-Si interaction. The shallow emitter of solar cell is one of the limiting factors for cell process engineers. Cells have to be fired high enough so that the glass dissolves SiN:H and Ag-Si alloy is created, but the paste should also not etch deeper or else the junction will be shorted. Firing mc-Si cells is challenging as preferential filamentary dissolution of Si through grain boundaries may also create shunt paths (Cheek, Mertens, Overstraeten, and Frission, 1984). More details are given in Chapter 3.

It is important to point out that although the fire-through process is not well understood, it is used very successfully in commercial cell fabrication. The success of the fire-through process is, in part, due to large process windows of back-contact formation and H diffusion for impurity and defect passivation. In the remaining part of the chapter, a brief description of all three major processes is presented.

2.5.1 Front Contact Formation

Screen printed Ag front contact of a solar cell is gridded to allow maximum light to enter the solar cell, while also collecting the photo-generated carriers and delivering the current to an external circuit. Figure 2.8 illustrates a typical configuration of a solar cell front-contact. It consists of several metal fingers that collect current from the neighboring regions and feed it into a bus bar. For example, in Figure 2.8, the current from region A is collected by fingers 1 and 2. The electrode is designed to offer minimum series resistance, while minimizing optical shadowing. The gridded contact of the fingers and bus bar typically covers between 7-10 % of the cell surface.

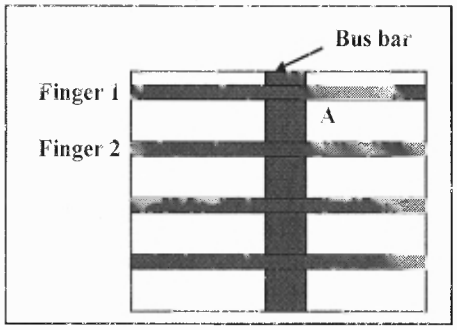

Figure 2.8 Schematic of the top-view of a typical front-electrode configuration of a commercial Si solar cell.

Front contact formation should produce a uniform Ag-Si interaction at the finger-silicon interface, while maintaining high shunt resistance (>≈8kΩ) that can yield a solar cell with high open-circuit voltage (V_{oc}) of at least 700mV and high fill factor (FF) of ≈85%. The front contact formation is however a complex process. Complexity arises because it has to accomplish a number of following functions:

1) Dissolve silicon nitride under the contact metal grid.

2) Interact Ag with Si in presence of glass to form a thin Si-Ag alloy thereby, avoiding shunting the shallow junction (≈ 0.3-0.5 μm).

3) Fusing/agglomeration of Ag particles to form a continuously conducting (≈10^{-6} Ω/cm^2) lateral path for current collection.

4) Bond/Adhere with silicon to give mechanical strength to the finger and bus-bar structure.

5) Withstand lateral temperature distribution (i.e. 20°C) across Si wafer to maintain contact grid homogeneity.

6) Allow itself to be soldered by tinned copper strip for ribbon attachment.

To fulfill these functions, detailed understanding of Ag–Si interaction and optimum firing profile is required. Further information about front contact formation mechanisms and current conduction in front contact will be discussed in Chapter 3.

2.5.2 Back Contact Formation

As mentioned before, to maximize the fire-through contact metallization technique, back contact formation should also be understood in detail. A detailed study of screen printed back Al contact formation mechanisms was carried out (Sopori et al., 2009). A novel technique of Si injection to minimize the defect formation during back contact formation was proposed (Sopori et al., 2009). The back contact of a solar cell must provide a number of electronic and optical properties that can enhance cell performance. These properties include:

- Creating a back surface field (BSF) for minority-carrier reflection that can lower the loss of photo-generated carriers at the back surface. As is well-known (Mandelkorn, & Lamneck, 1973), the BSF arises from band-bending at the p^+-p region. It is important to remember that BSF is useful only when the diffusion length of minority carrier is longer than cell thickness. The thickness of the p+ region that is required for an effective BSF formed by doping is typically about 10μm (Sopori et al., 2007). Thus, it is prudent to determine how the cell should be processed to create a uniform, ~10-μm-wide p+ region in conjunction with a good front contact.

- Produce a uniform low-resistance (e.g. the bulk resistivity of screen printed Al = 30μΩcm (Porter, Teichera, & Meier, 2002)) ohmic contact to achieve a high fill factor (>85%) in the cell. Low-resistance contact formation requires a well-formed ohmic contact between Si and Al to be produced beyond the p^+ region. An ideal contact would

consist of Al/p^+/Si. However, as discussed later, contact formation results in two major deviations from this configuration that are caused by: (a) a eutectic composition that accompanies formation of the p^+ region (i.e., the eutectic composition has a higher sheet resistivity compared to Al, which can lead to increased series resistance of the cell); and (b) a region of disconnected sintered Al particles in a glass matrix, which will likewise increase the sheet resistance of the back contact.

- It should form a smooth, dimple-free Al surface. Optically, the back contact must be highly reflective (>80%), with very little absorption so that it contributes effectively to light-trapping.

In addition to these, the process of making the back contact should be compatible with efficient gettering of impurities. In commercial solar cell fabrication, the primary consideration is given to the electronic properties, whereas optical reflection and gettering are often considered by-products.

The back contact formation relies heavily on alloying of Si and Al to produce a controlled stratified structure. To obtain the desired electronic properties of the back contact, the alloying of Si and Al must be carefully controlled. Kinetics of Si-Al melting and re-solidification of various phases during the firing cycle must be understood. While the inks for front contact are designed to form good contacts at temperatures below 800°C, a good back contact also requires process temperatures in excess of 800°C (to ensure high p+ doping in the BSF).

Experiments were carried out to study the mechanism of melting and solidification of Si-Al during a fire-through process. Experiments were done on the single wafers and mc-Si solar cells. These cells were fabricated on 156 mm, textured

wafers using commercial screen-printed front and back contacts. The wafers were single crystal, single side polished with Al deposited by electron beam deposition either on the polished side or the rough side. The firing was done in an optical furnace in which the cell is illuminated with a tailored optical flux profile and the temperature of the wafer/cell is monitored to determine local temperatures at various critical areas such as under the metallization and away from it (Sopori et al., 2007). All single crystal samples were illuminated from the Si side.

The processed samples were characterized by a variety of techniques. SEM was used for high resolution imaging of the c/s of processed contacts and for dopant profiling to study the BSF formation. SKPM was used to generate potential profiles to evaluate formation of the BSF and determination of local conductivity. SIMS profiles were used for measurement of Si diffusion in Al and profiles of Al after firing. Solar cells were characterized by dark and illuminated I-V analyses.

The structure of a typical contact formed by this process is shown in Figure 2.9. Figure 2.9a is an optical micrograph of the c/s showing the back contact of a cell. The Si surface shows the texture and a Si-Al eutectic layer exists at the interface. The eutectic manifests itself as Si-rich and Al-rich phases (Sopori et al., 2009). This can be observed at the valleys of the Si surface. Away from the interface, the aluminum particles are sintered and agglomerates of the enlarged particles are separated by inclusions of glass. The re-crystallized Al-doped Si side has retained some of the texture. Because this Figure 2.9a is an optical image, we do not see the BSF. Figure 2.9b shows an SEM micrograph taken in dopant contrast mode. As can be seen, the BSF is uniform and follows undulations of the interface. The Al-Si eutectic is seen to fill the texture valleys of the

interface. It may be noted that while the thickness of the eutectic is changing, the BSF region is nearly constant. It was found that the maximum thickness of the BSF is controlled primarily by the thickness of Al.

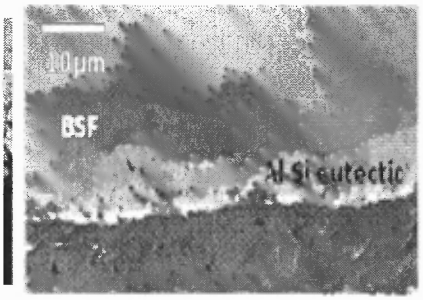

(a) (b)

Figure 2.9 Photographs of Back Al contact, (a) An optical micrograph of a c/s cell showing back Si-Al alloyed structure, (b) Dopant contrast SEM image of c/s cell showing a uniform BSF produced by Si injection alloying.

Figure 2.10 shows an SEM image (Figure 2.10a) of a back contact and its potential profile (Figure 2.10b) under various bias conditions obtained by SKPM. A voltage of 110 mV appears across this p^+-p region. Figure 2.10c is an optical micrograph showing a very important feature of the alloy thickness variation. It shows that thickness of the alloy is largest at the valley of the texture and minimum at the peak of the texture. Furthermore, the alloyed region is continuous within the texture valley. This indicates that during the formation of Si-Al alloy, the melt initially fills up the texture valley. Any excess melt spills over the adjacent valleys and then builds up. The depth of the p^+ region is generally larger at thicker alloyed regions.

Firing process of solar cell involves a very rapid diffusion of Si into Al. This diffusion controls the initial composition and location of the initial melt near Si-Al interface (Mehta and Sopori, 2009). Figure 2.11a shows a SIMS profile of Si diffused

into Al caused by a short firing profile; the thickness of Al was kept at only 1 micron to show that the diffused Si can accumulate at the Al-air interface. Figure 2.11b shows SIMS profile of Si and Al resulting from optical processing at 545 °C for 10s.

In a screen-printed cell, the diffused Si can disperse between melted Al particles. Figure 2.12 shows an SEM (Figure 2.12a) and the EDX images of Si (Figure 2.12b) and Al (Figure 2.12c). In Figure 2.12b, one can see that Si has diffused deep into Al beyond the alloyed region. The presence of Si around Al particles will cause increase in the series resistance of the cell (Mehta et al., 2009).

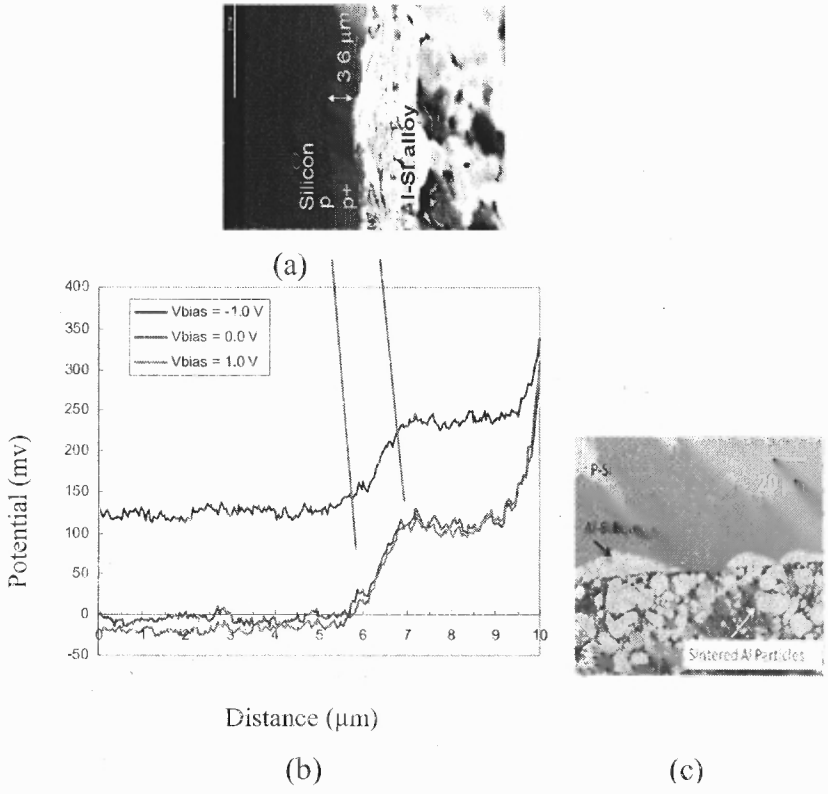

Figure 2.10 (a) An SEM image, (b) corresponding SKPM image (potential profile), and (c) Optical micrograph of a c/s of back contact , showing thickness variations of the alloyed region corresponding to the textured profile of the Si.

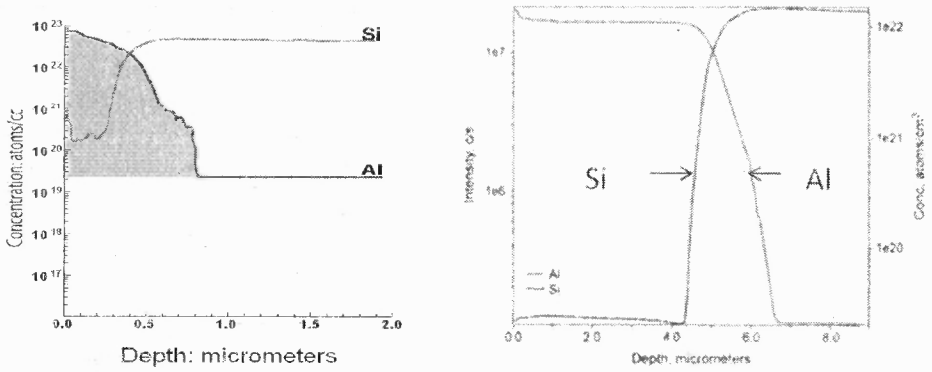

(a) (b)

Figure 2.11 SIMS diffusion profiles of study of Si diffusion in Al (a) SIMS profile of Si and Al resulting from optical processing at 300°C for 30s, and (b) SIMS profile of Si and Al resulting from optical processing at 545 °C for 10s.

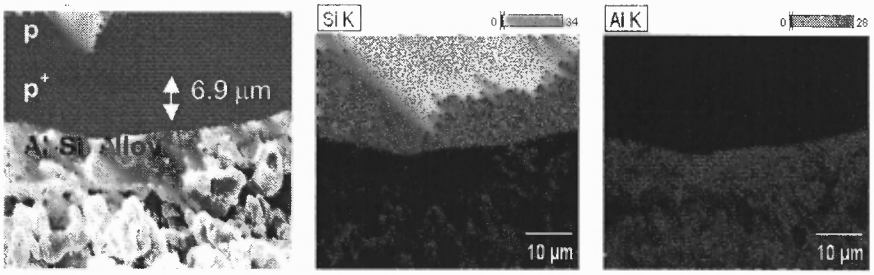

(a) (b) (c)

Figure 2.12 Electro-optical images of back contact structure of c/s cell, (a) Dopant contrast SEM image and corresponding EDX images (b) Si and (c) Al.

Based on above results, a desirable profile to encourage initial Si diffusion was prepared. The profile has been explained in detail in (Sopori et al., 2009). An optimum firing temperature profile leads to the formation of a p-Si/p^+-Si/ Si-Al eutectic/unmelted Al, at the back contact of a Si solar cell. Variations in the interface properties were found to arise from Al-Si melt instabilities. Experiments show that the melt formation is strongly controlled by diffusion of Si into Al. During the ramp up, a melt is initiated at the Si-Al interface, which subsequently expands into Al and Si. During the ramp-down,

the melt freezes causing the doped region to grow epitaxially on Si, followed by the solidification of the Si-Al eutectic. Any unmelted (sintered) Al is dispersed with Si. Implications on the performance of the cell have been described earlier (Sopori et al, 2009).

2.5.3 Hydrogen Passivation

Hydrogen diffusion occurs very rapidly at firing temperatures because there is little or no trapping of hydrogen at elevated temperatures. It has been shown that a significant amount of H is present at the damaged Si surface within a short depth (Sopori et al., 1996). This hydrogen diffuses into the back of a Si cell to passivate impurities and defects. From the experiments (Sopori et al., 2004), it was found that there is bilateral flow of hydrogen from SiN:H into Si and into air. This flow is mediated by the damaged layer (and the hydrogen trapped in this layer). It is important to determine the role of the Al back-contact, which can confine hydrogen within the cell. Such confinement may occur because of a physical barrier and because of the BSF, which can either aid or retard H ions. These results can play an important role in passivation kinetics and may account for differences in the cell performance between co-fired and separately fired conditions. Because diffusivity of H at the firing temperatures is very large, extended firing (i.e., higher temperatures and/or longer times) can result in the depletion of H from the bulk of the cell (due to evolution into air and possibly from the back-side contact of a standard solar cell). Figure 2.13 shows the passivation effect due to H diffusion caused by putting a mc-Si ribbon sample through several firing cycles.

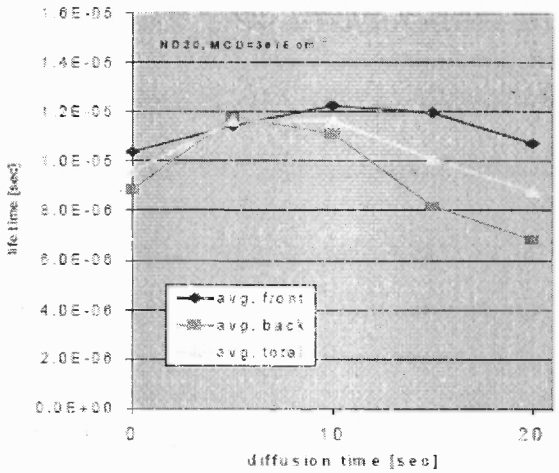

Figure 2.13 Passivation effect due to H diffusion in a mc-Si wafer through several firing cycles.
Source: (Sopori et al, 2007).

This sample had PECVD nitride deposited on both sides. Each firing cycle was done to expose the sample to the maximum firing temperature (<800°C) for 5 s. The passivation was observed by lifetime measurements using the quasi-steady-state photoconductive decay technique. Figure 2.13 shows the lifetime data measured on the front and back sides; each data point represents spatial average taken over three regions of the ribbon sample. Also shown in the Figure 2.13 is the average of front side and back side lifetime. It is seen that initially lifetime increases with the number of firings but decreases after 3-4 firings. The peak of the lifetime is quite broad.

Hydrogen passiviation was not in the scope of the present study; so the reader is encouraged to read work performed earlier (for example, Sopori et al., 1996).

CHAPTER 3

FRONT CONTACT FORMATION IN SCREEN PRINTED mc-Si SOLAR CELLS

In this chapter, front contact formation in screen printed mc-Si solar cells is studied and analyzed in detail. First, a review of the existing hypothesis and models for front contact formation is presented. Next, experimental procedures that are practiced to understand front contact formation is discussed. Results of experiments are presented and explained. Interaction between various reactants (e.g., silver paste, SiN:H, and Si) are discussed. Finally, a hypothesis on the front contact formation mechanism is presented.

The widely accepted fire through screen printed thick film technique, achieves various goals (see Chapter 2) reasonably well. Surprisingly though, it is not yet an optimized process. While industry (Neuhaus, & Munzer, 2007) has reported achieving V_{oc} of 615 mV and FF = 0.77-0.78, on 156.8cm^2 cells, the detailed understanding of contact formation and current conduction mechanisms in metal contacts is lacking. Lack of details (i.e. Ag-Si reaction kinetics) of contact formation on micron scale restricts achieving higher efficiency (η>18%) consistently at production volume of 2000 wafers/hr.

Screen printed silver grid has lower FF than the one fabricated by photolithography (Doshi, Mejia, Tate & Rohatgi,1997). Several scientists (Cheek, (1984), Ballif, (2003), Hilali, (2005), Schubert, (2006)) have proposed various models of contact formation which give incomplete picture of the process.

Many hypotheses of the before mentioned researchers speculate on chemical interactions that occur between various constituents of ink during the firing step. In the next section, a review of existing hypothesis on front contact formation on thick film screen printed Si solar cells is presented.

3.1 Review of Existing Hypothesis

The contact formation mechanism is commonly explained by invoking silver-silicon phase diagram (Chapter 2). The Si-Ag eutectic point in the phase diagram is ≈ 835°C (89 atomic percent of Ag) (Olesinski, Gokhale, & Abbaschian, 1989). Both the heating and the cooling behavior of the metal-semiconductor contacts are described using this phase diagram. However, explanation of a complex system that involves Ag, Si, SiN:H, C and metal oxides (e.g. PbO, ZnO, BiO) by a two phase diagram is not correct. Such an open system has to be supplanted by additional information.

Prudenziati, Moro, Morten, Sirotti, & Sardi, suggested in 1989 that silver particles sinter at firing temperatures and glass percolates through them to react with the silicon. During the process, glass dissolves some Ag and becomes conductive. The thickness of glass then determines the contact resistance between finger/bus bar and Si. However, the time spent by the cell at peak temperature (≈750°C) is ≈25 minutes. Currently, during firing, solar cells spend few seconds at high temperature (≈800°C) and thus there is no major transport of constituents (i.e., Ag, glass) during such a short time of firing.

In 1984, Cheek, Mertens, Overstraeten, & Frisson suggested that sintering causes Ag particle size to increase three times (via liquid phase sintering) and oxygen is required for lower contact resistance. However, the co-firing process used was longer (i.e. 4 min at 810°C). Some agglomeration of silver particles cannot be ruled out but significant

increase in the size of individual Ag particles is difficult, as peak firing temperature (<800°C) of current firing process is much lower than the melting temperature (961.93°C) of silver. Furthermore, industrial solar cells are normally fired in inert gas (i.e., N_2) atmosphere and use of oxygen can produce flaky back aluminum contacts (Huster & Schubert, 2005).

Thuillier, Boyeaux, Kaminski, & Laugier, in 2003, used TiO_2 as antireflective coating and firing step was followed by 20 minutes of low temperature (400-450°C) forming gas annealing. They noticed phase separation in the finger structure with oxide coated silver particles as porous structure and amorphous 300nm glass layer separating bulk of the silver finger and silicon. According to Thuillier et al, contact ohmicity is not realized by the active metal of the paste but due to metallic elements in the oxides. The finger/silicon interface will have residues of oxides and nitrides. Thus, the available contact area is reduced by about 30%. To minimize contact resistance, grid designers use silver (i.e., resistivity $=1.59\times10^{-8}$ Ω.m) for finger and dope emitter (n^+ silicon) with 1E+20 atom/cm^3 phosphorus atoms. Process engineers strive to have maximum Ag-Si contact with minimum shunt damage. To depend on glass (i.e. oxides and nitrides of unknown composition), for contact ohmicity, defeats the purpose of using silver and highly doped silicon. TiO_2 does not passivate the front surface, and is not used in industrial solar cell manufacturing environment. Moreover, the post metallization annealing is not a standard process used by the industry.

Ballif, Huljic, Willeke, & Wyser, in 2003, suggested that Si and Ag dissolve in the glass frit at firing temperatures. Silver and silicon diffuse through the glass and, on cooling, the Si re-grows epitaxially on silicon and the Ag crystallites grow randomly on

silicon. There is a continuous layer of glass between silver crystallites that serves as current collection point for the finger. The lead (Pb) from the glass frit precipitates at the interface. The current peak firing step used in the industry is very narrow (i.e., 5 seconds) and in such short time duration, dissolution of silver by glass, its transport through molten glass and re-crystallization on silicon is very difficult.

Hilali, in 2005, has done extensive experiments with various pastes, and emitters of high and low resistivity. He has also suggested dissolution of silver particles in the glass layer. The silver particle size determines amount of dissolution and sintering. On cooling, the lead and silver separate out. Silver re-crystallizes on silicon as pyramid shaped crystallites. This explanation, however, is counter intuitive because one would expect that, under normal firing conditions, a significant dissolution of Ag in glass cannot occur. This conclusion was also reached by Schubert in 2006, who performed experiments that led to indications that it takes a long time for silver particles to dissolve at normal cell firing temperatures.

Shubert et al. did extensive analysis to understand the contact formation and current conduction mechanisms. Schubert et al. suggested that the lead oxide gets reduced by the Si. The generated Pb alloys with the Ag. Glass etches (100) silicon. On cooling, Ag crystallizes on <111> pyramidal planes. According to Schubert et al., Pb is the transport media of the Ag. During cooling, lead precipitates just below the silver bulk of the finger. Other scientists (Ballif et al, 2003) have not found lead precipitates. Young and Carroll, in 2000, suggested that metal oxide in the glass, at firing temperatures, is reduced by Si (i.e., $xSi + 2MO_x = 2M + xSiO_2$).

This effect would mean that "solvent metal" (M) is present wherever glass and Si are in contact. It would also suggest the existence of a thin layer of SiO_2 at the interface. However, a detailed explanation as to what happens in the micro scale is lacking.

In a fire through process, as is clear by now, glass frit is supposed to dissolve SiN:H and make physical contact with the underlying silicon emitter. Since there is no vigorous intermixing of constituents happening, reaction products are expected to stay at the interface. Kontermann et. al., in 2009, used EDX spectra and showed that after peak firing step (820°C), some amount of SiN:H is still remaining. He measured nitrogen peak in the EDX analysis of the interface. The current collection was proposed to occur only in regions where glass has etched SiN:H completely. Kontermann et al. sputter deposited SiN:H, on textured single crystal Si having pyramids with average height of 12μm. This requires a strong and long texturing process which is not a standard in the solar industry and thicker SiN:H can be expected in valleys of pyramids this tall. The etch depth for conventional alkaline etched mc-Si is less than ≈4.0 microns. Glass becomes molten at 550°C (Prudenziati et. al.) and, at 820°C, aggressive glass frit will dissolve 70nm of SiN:H very quickly. Other researchers such as Khadilkar et al., Shubert et al. did not find SiN:H at the interface.

Ching-Hsi Lin et al., in 2008, used transmission electron microscopy (TEM) and high resolution TEM to show that micro-crystallites of Ag precipitate from the glass frit and take part in the current conduction mechanism. Glass was shown as supersaturated with dissolved Ag atoms. Ag embryos (i.e. Ag crystallites) were found at the Si surface. While it is to be noted that optimally fired single crystal Si cells were used in the study, no information is available about firing conditions or electrical characteristics of the fired

cells. A few nm thin glass layer was always found between bulk Ag and Si. In a typical process, a solar cell spends few seconds (<7 sec) at elevated temperatures (650°C to ≈800°C) and dissolution of Ag, super-saturation of glass with silver atoms, precipitation of Ag and nucleation of embryos at Si surface is difficult to be achieved in such a short time.

Kyoung-Hook Hong et al., in 2009, used various amounts of Ag in glass and fired the wafers at 800°C for 20 minutes. He showed that Ag gets dissolved and Ag^+ ions react with Si to form silver crystallites. It is again important to remember that solar cells spend a few seconds at temperatures around 800°C. Thus, the study conducted earlier cannot be applied to understand conventional industrial silicon solar cell firing process.

Khadilkar et. al., in 2005, used (100) and (111) oriented single crystal silicon wafers to study the effects of orientation on crystallite formation. They found pyramid shaped Ag crystallites on (100) silicon and lens shaped crystallites on (111) silicon. However, it is a typical etching behavior of (100) and (111) silicon planes. The cell was kept at 930°C for two minutes. Since 930°C is above the Ag-Si eutectic temperature, it is possible that Ag-Si alloy filled the etch pits on the silicon surface. This type of firing cycle is not a standard in the industry. Detailed discussion about the crystal structure of Ag crystallite has not been given in this study.

Jeon, Koo, & Hwang, in 2009, used lead free and cadmium free silver paste made with different additives and studied front contact formation mechanisms. The authors fired the cells at a set point temperature of 910°C. It was reported that continuous Ag-Si alloy is formed at finger/bus-bar and silicon interface. The voids found in the structure of Ag finger were reported to be due to burning of binders (i.e., ethyl-cellulose resins). The

silver silicon system has a eutectic at 835°C (11% Si). Thus, at 910°C, >12% silicon atoms in the emitter region below the finger will be consumed to form Ag-Si alloy. The shallow junction (≈0.36μm) can easily shunt at these processing conditions. As was shown in Chapter 2, globules of glass are trapped between Ag particles as the cell is rapidly cooled down. If sample preparation method is not optimal (see Chapter 1), glass globules can be erroneously interpreted as voids.

The limitation in screen printing technology to print finer (<75μm wide) and closely spaced fingers with higher aspect ratio results in large shading losses (7-9%). The temperature across the cell is non-uniform largely due to grid which accounts for the temperature distribution. Most of the investigators have neglected the temperature distribution effects of grid on contact formation mechanisms. Impact of metal contact grid on temperature variation has been discussed in detail in Chapter 4.

The silver, lead (or other metal oxides used as replacement to lead) containing glass and Si are main players in the contact formation mechanism. While all agree that glass plays an important role in Ag –Si interaction, disagreement on how exactly this is accomplished exists.

Most of the studies involve small size samples (<100cm^2). Modules sold in the market in 2010 have cells with 246cm^2 area. Furthermore, many experiments (e.g. Khadilakar et. al., Kyoung-Hook Hong et. al.) were performed in unrealistic conditions that may not occur during typical contact formation. Sometimes, the firing times are too long or usage of non commercial paste or the emitter doping is non standard or the firing temperatures are not representative. This results in an incomplete picture of contact formation mechanism.

Despite the success of the fire-through process, many aspects of the physics of the front-contact formation remain unclear. Some of the concerns relate to:

1. Kinetics of Ag-Si interactions—In particular, how do Ag particles, which are dispersed in a matrix of glass frit, interact with the Si surface?

2. How do Ag particles agglomerate to form laterally conducting contacts, and how does it influence the series resistance of the cell?

3. What is the actual temperature at which Si-Ag forms an alloy, and is this alloy formation aided by the presence of the "solvent metal" M?

4. To what degree does the melting of Ag particles occur?

5. Does Ag get dissolved in glass and re-precipitate, as proposed in some published work?

6. How much Si is consumed in a typical contact formation?

Answers to these questions can help control the co-firing process better and increase the area of Ag-Si interaction to decrease the contact resistance. To further study these issues, experiments were performed as described in the next section.

3.2 Experimental Procedure to Study Contact Formation Mechanism

Experiments were aimed at (i) understanding the mechanism of front-contact formation in a manner to be able to predict the most-favorable process that can yield the best junction performance, (ii) Identification of the spatial distribution of various constituents in the ink after firing, and (iii) Accurate determination of the temperature at the Si-metal interface during contact formation, so that one can apply information from phase diagrams as a guide to project the degree of melting and composition of the Si-Ag alloy.

SiN:H-coated, n+/p cells on single-crystal and multi-crystalline (mc)-Si wafers were screen printed with front and back metallization patterns and fired in a static optical furnace—a computer-controlled furnace that applies a predetermined optical flux as a function of time to the cell. For metallization pastes, Ferro's (Ag-based and Al-based) inks of different properties such as composition and particle size were used. The temperature distribution over the cell was measured by multiple thermocouples attached to the cells. Solar cells were processed at under-fired, optimally fired, and over-fired conditions. The fired cells were analyzed by dark and illuminated current-voltage (I-V) measurements to determine cell parameters (V_{oc}, J_{sc}, and FF), series resistance, and shunt conductance, and by a variety of analytical techniques including secondary-ion mass spectroscopy (SIMS), Fourier transform infrared (FTIR) spectroscopy, and electron-beam methods.

To accurately characterize the contact interface, truly representative samples have to be prepared. SEM samples for most of the before mentioned researchers were prepared by cleaving. Cleaving is fast but creates striations and the cleaved surface is not planar. Such surfaces will not lead to accurate analysis of the Si-Ag interface. To perform a detailed statistically meaningful characterization of Si-metal interactions, a procedure for cross-sectioning large-area solar cell samples was developed, using chemical-mechanical polishing (CMP).

CMP process has been described in detail in Chapter 1. This polishing technique generates a large, planar cross-section of the composite (stratified) device that can be analyzed by AFM, C-AFM, SKPM, and other electron-beam techniques to measure penetration and distribution of metal into Si, and electric potential and field distributions

at the Si-Ag and Si-Al interfaces. This cross-sectioning technique provides access to various components in a segregated composition (such as glass, Ag, Si-Ag alloy in a contact) without destroying the probe tips.

3.3 Results

3.3.1 Cross-sectional Analysis of Finger-Silicon Interface

Figure 3.1 is an SEM image of a cross-sectioned edge showing the Ag front-contact of an optimally fired solar cell. Here, individual particles getting polished in half (i.e., planar cross-sectioning) can be seen. Also seen is the glass frit covering the particles. The Ag-Si alloy can be clearly seen at the finger Si interface. The Ag-Si alloy is not seen above the interface. Some Ag particles coming off during cross-section polishing are noted, and a discontinuous separate glass layer (i.e. globules) can also be observed. SEM does not identify conducting/and or insulating regions; therefore, C-AFM analysis was performed. Figure 3.2 shows a C-AFM image identifying glass phases as insulating regions of low current.

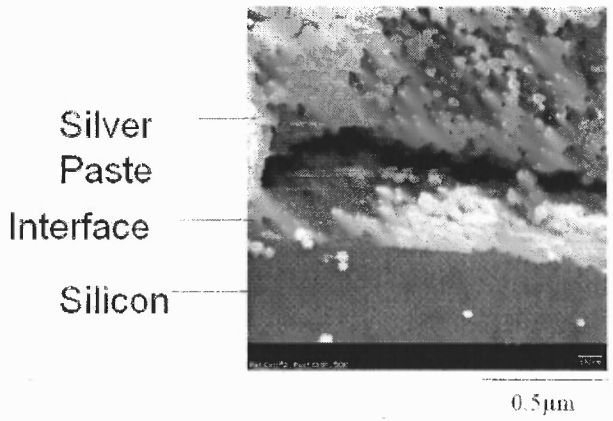

Figure 3.1 SEM image of a top view of cross-sectioned fired cell showing Ag front-contact.

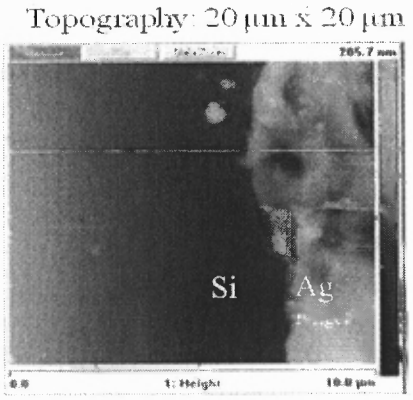

(a)

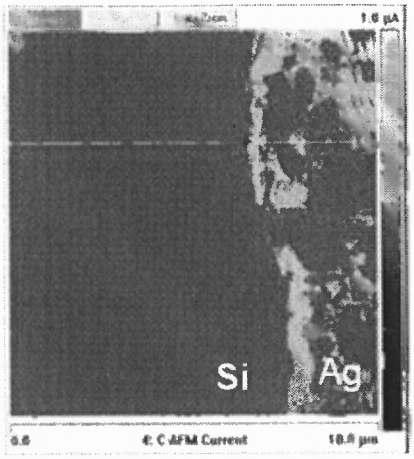

(b)

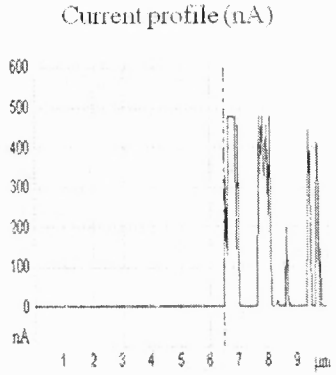

(c)

Figure 3.2 C-AFM images of front contact of c/s cell, (a) Topographic image, (b) current image, and (c) current trace at Ag-Si interface showing Ag particles (conducting) and the glass matrix (non conducting).

Selectivity of C-AFM technique can be studied by looking at two features on the top central part of Figure 3.2a. These glass phases are not conducting and hence are not seen in Figure 3.2b. Analyses of such images for different time-temperature (t-T) profiles (underfired, overfired and optimally fired), shows that, under optimum alloying conditions, a dense Si-Ag alloy is formed at the interface.

Figure 3.3 shows the SKPM images of c/s cell. Figure 3.3a shows topography of the front contact interface with marker (i.e. white line) showing area of the scan. Figure 3.3b shows the strength of the metal/semiconductor field for different bias directions, as probe tip is scanned from left to right. Figure 3.3c displays variation of surface potential as the probe tip is scanned from left to right. It is important to recognize that these types of analysis is not possible if the sample is cleaved or diced, since it has a rough surface and can damage the tip and give erroneous readings.

3.3.2 Etching Studies

Since c/s samples still give small area information (e.g. finger width is between 146-156 μm), preferential etching of the finger/bus-bar and Si interface was done to study Ag-Si interactions on a larger scale. Fired cell sample was dunked in 3% dilute HF solution for 5-10 minutes to remove glass, glass coated Ag particles, SiN:H and oxides from Si surface. In the time duration selected, etch rate of silicon by HF is minimal. Figure 3.4 is an SEM image of part of a metal finger from a cell that was fired optimally, and the Ag that did not react with Si was etched away.

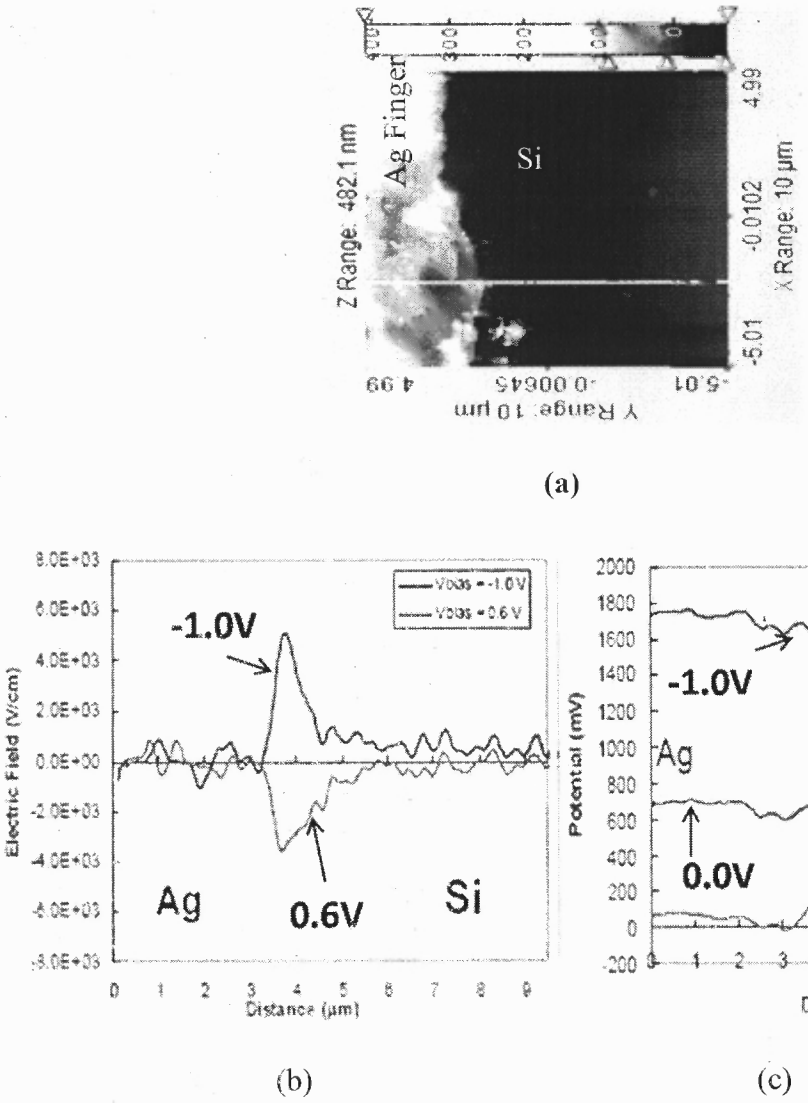

Figure 3.3 Electro-optical images of Ag-Si interface, taken by SKPM, (a) Topography - 10µm x 10µm, (b) E field profiles (V/cm) and (c) SKPM potential profiles (mV).

Ag-Si interactions lead to the formation of Ag-rich and Si-rich regions. It can be seen that the interactions of Si-Ag at the front contact are very non-uniform. From Figure 3.4, it is clear that in a solar cell the current flow has at least two paths: an ohmic contact in the Ag-rich regions and (perhaps) a tunneling contact at the Si-rich regions. Thus, it is desirable to have a large fraction of shallow (0.1µm deep) Ag-rich region to produce a cell with a high FF (>0.8).

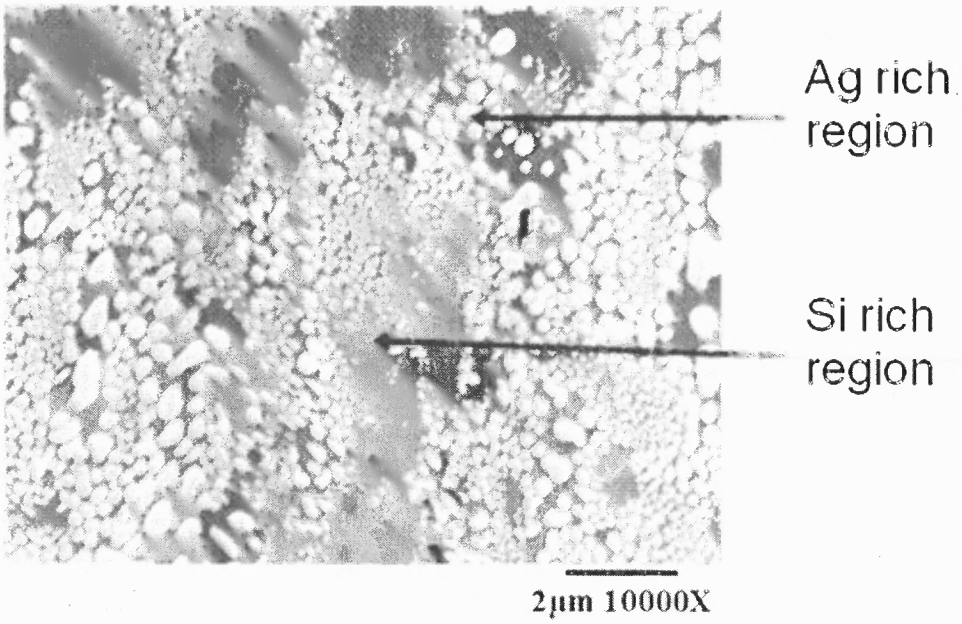

Figure 3.4 SEM image showing formation of Ag-rich (white) alloyed regions under a metal finger.

Figure 3.5a is an SEM image of the sintered Ag-Si-M alloy at the edge remaining after etching. The poor resolution of the screen printing technique can be seen as clear edge of finger is not defined. Figure 3.5 b and c show effect of grain orientation on the alloy growth. Similar effect has been observed by (Khadilkar et al, 2005). In Figure 3.5d, a crystal of one of the solvent metal added (Zn) can be seen on sintered Ag alloy. Formation of a Ag-rich region depends on many factors, including size of the Ag particles, process conditions, and ink composition. From the etching results, it is clear that regions of the metallization that do not directly react with Si are held together by the glass. This result agrees with the results of Fig. 3.2.

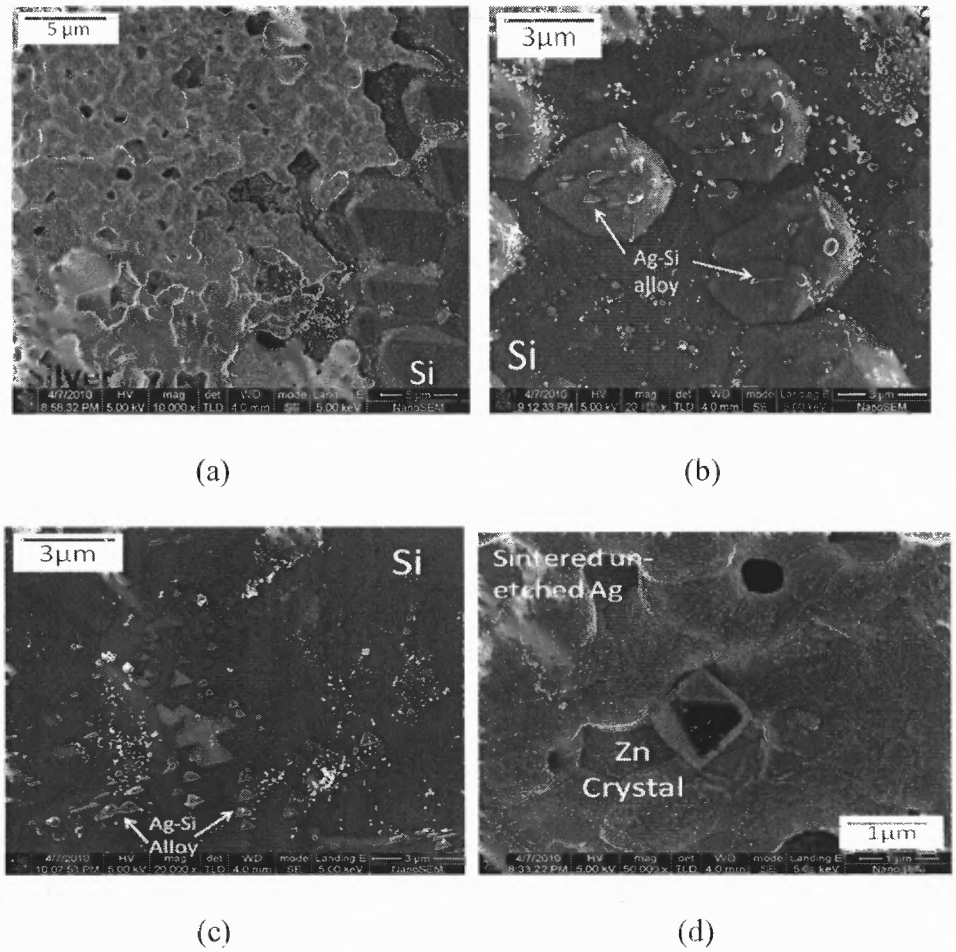

Figure 3.5 SEM pictures of Etch bus bar (a) Near the edge of the finger (b) elongated Ag-Si-M alloy (100) plane, (c) Pyramidal shape of the Ag-Si-M alloy due to grain orientation (111) and (d) Zn crystal inside unetched sintered Ag-Si-M alloy.

3.3.3 Consumption of n+ Region

Semiconductor industry makes near ohmic contacts by alloying. Heavy doping of semiconductor surface is another way to prepare a near ohmic contact. For ohmic contacts on n-type silicon, doping of the order of 1E10+20atom/cm^3 is required (Schroder & Meier, 1984). This doping is commonly carried out using $POCl_3$ diffusion. This level of high doping creates dead layer at the top of the n+ surface of Si. The surface recombination velocity increases (>100^{2}cm/s) as doping creates surface damage. Additionally, optically, the blue wavelength regime of the visible light is lost due to this layer. Thickness of the n^+ layer is kept in the range of 0.3-0.5µm. The sheet resistance is

40-50Ω/□. As seen from Figure 3.4, one consequence of alloying at the front contact is that it consumes dopants near the surface, producing a contact at a higher resistivity interface. This produces a local low V_{oc} region with a manifestation of shunting. Figure 3.6 shows the secondary-ion mass spectroscopy (SIMS) profiles of Phosphorus content after the metal bus bar is etched away from the Si surface. As seen in Figure 3.6, the phosphorous content decreased in the emitter region of the cell. The Ag-Si alloy formation may decrease the net local P content. Thin emitters are more susceptible to shunting. Thin emitter near grain boundary can provide shunt path.

3.3.4 Agglomeration of Ag Particles

To determine the role of glass and its composition in the formation of Si-Ag melt, the interaction of glass with Ag and the interaction of Si with the composite of Ag in glass matrix were investigated. To examine the Ag-glass interactions, screen-printed cells were baked at different temperatures. Figures 3.7a, b, and c show SEM images on simply dried ink, ink baked at 450°C, and ink baked at 600°C, respectively. In Figure 3.7a, the smaller particles of Ag are separated by flake-shaped glass particles. In Figure 3.7b, the flakes have collapsed due to softening and are covering the Ag particles. In Figure 3.7c, Ag particles are surrounded by molten glass. Thus, we conclude that, under normal firing of a solar cell, Ag particles or agglomerates of Ag particles remain suspended in a matrix of molten glass before the peak temperature is reached. This is consistent with the results of under-fired cells.

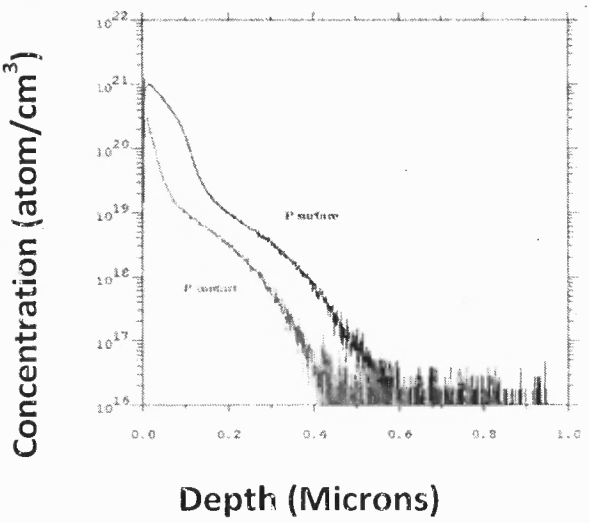

Figure 3.6 SIMS profiles of phosphorus under the metal bus-bar and away from it, showing consumption of P by the metal.

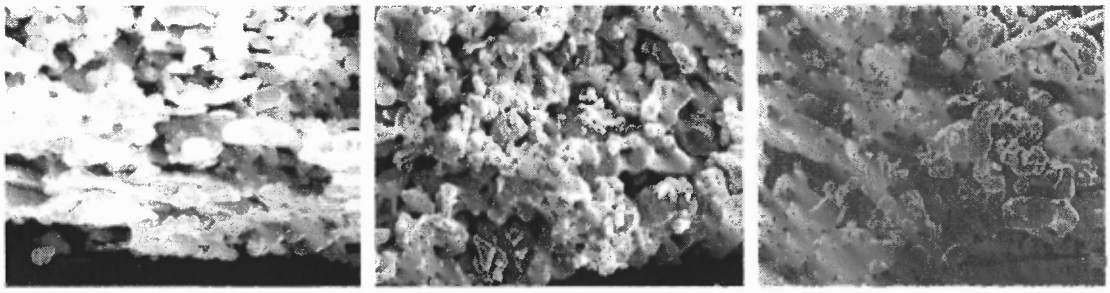

(a) (b) (c)

Figure 3.7 SEM images of Ag-ink before and after baking. (a) Unbaked, (b) Baked at 450°C, and (c) Baked at 600°C.

It was noticed that organic vapor fumes from binders and solvents came out in two steps (once between 200-250°C and then 400-450°C). Since whole area screen printed back al contact is used; maximum fumes come out from the back side. Same fume behavior from the cell was observed when cell was fired in OPF (e.g., since OPF currently has single wafer processing capability; the baking step is kept longer.) Based on the paste composition, the exhaust of the furnace has to be adjusted accordingly. Since

the OPF uses optical light effect to heat wafers, presence of any fume between cells and lamps can have detrimental effect on the cell characteristics. The thick film paste manufacturers use a proprietary composition of paste to meet the cell manufactures requirements; efficient exhaust systems should be designed for safe work environment and proper firing of cell without degrading the cell characteristics.

3.3.5 Analysis of Si-Ag-M Alloy

Cross-sectional analyses of solar cells fired using various firing profiles to examine the formation of Si-Ag alloy was carried out. In the under-fired samples, there is very little alloying of Si with Ag. In the optimum firing case, islands of melt are generated, as seen in Figure 3.4. Figure 3.8a is an SEM image of a cross-sectioned sample that was fired under near-optimum conditions. This Figure 3.8a shows several features:

1. Large agglomerates of Ag particles fused together into a region of continuous Ag.
2. Some Ag particles separated by regions of glass, and
3. Some isolated particles of Ag that have the appearance of precipitates.

Further EDX analyses of regions 1 (i.e., Figure 3.8b) and 2 (i.e., Figure 3.8c) show that these regions have Si and Ag as majority constituents. Therefore, it has the composition of an alloy. Ag crystallites were not found in c/s samples of silicon solar cells.

(a)

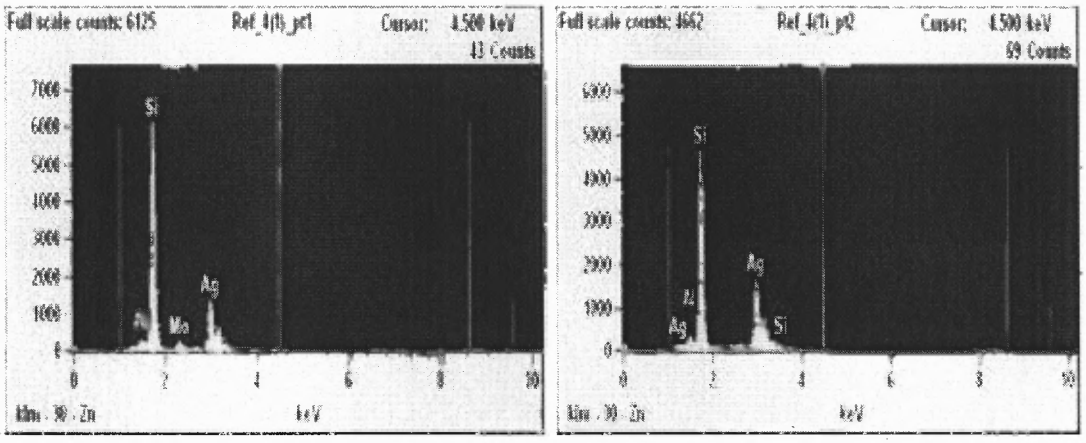

(b) (c)

Figure 3.8 EDX analysis of Ag-Si interface of c/s cell, (a) SEM image, and (b) EDX analyses of interface of Ag-Si alloy (points 1 and 2).

Figure 3.9 shows the area below the bus-bar after it was etched in 3% HF. Here different shapes of Ag-Si-M alloy can be found based on different grain orientation and local temperature variations. EDX analysis in Figure 3.9c shows unusually high carbon concentration. While some may have come from the EDX system, rest is believed to be due to solvent burnout during baking step. EDX analysis of point 1 shows Ag-Si alloy composition. Figure 3.10 is a close view of un-etched Ag-Si-M alloy at the edge of the bus bar. A Zn crystal/particle can be seen embedded in the alloy. Figure 3.10c is the EDX analysis of the components found at point A on the crystal.

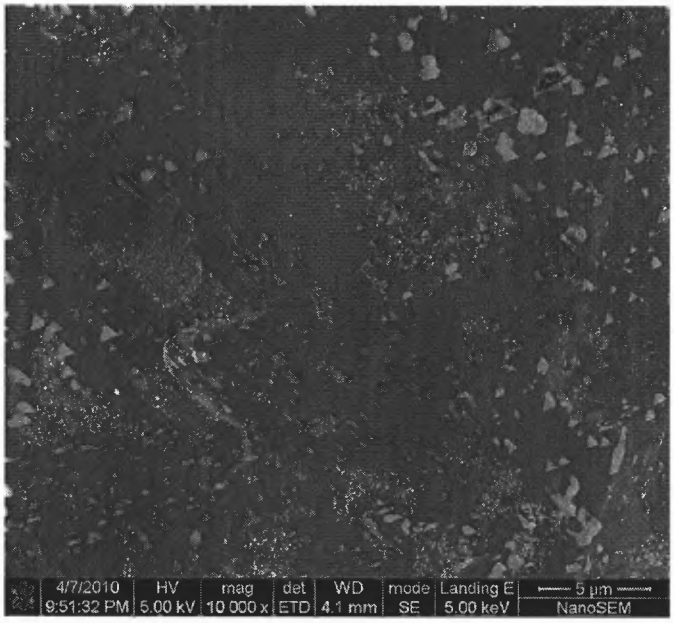

(a)

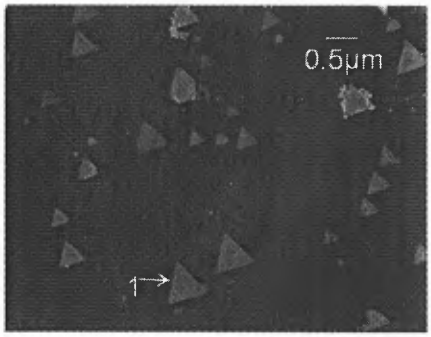

(b)

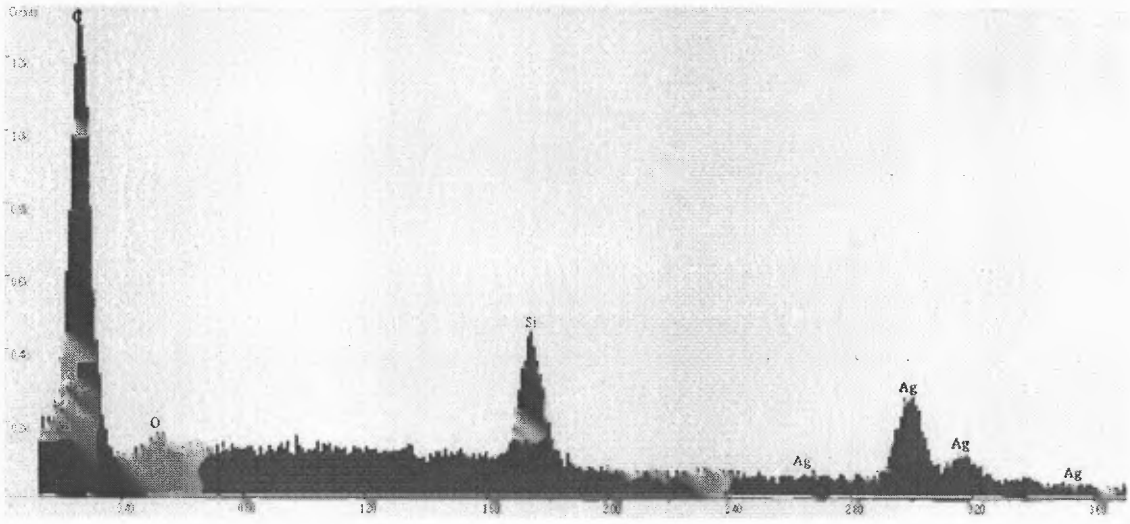

(c)

Figure 3.9 EDX analysis of un-etched silver-Si alloy at the busbar-Si interface. (a) SEM image of etched busbar. (b) Close view of small region of the interface, (c) EDX analysis of the point 1 in Figure 3.9 (b). A large amount of carbon was measured at the interface. Some amount was residue from the solvent burn out during baking step.

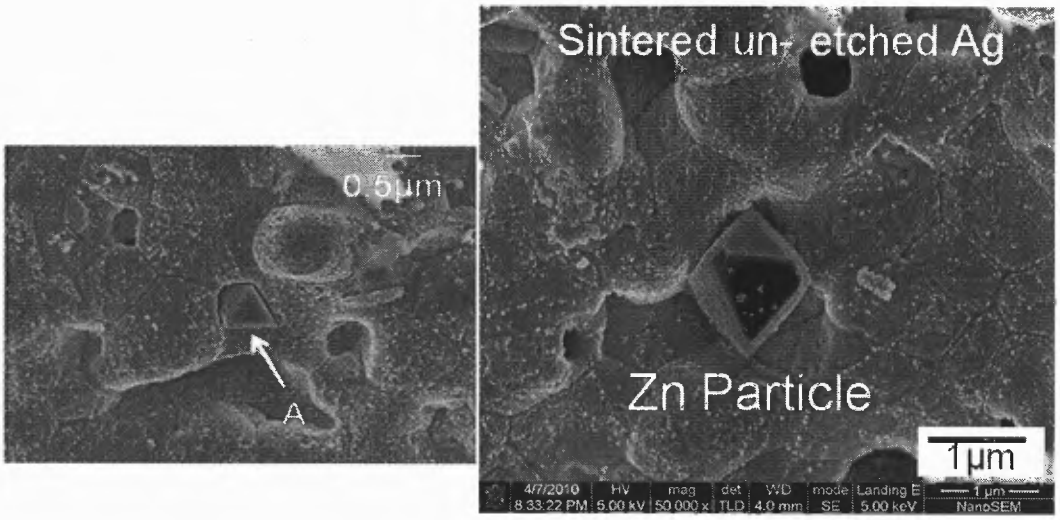

(a) (b)

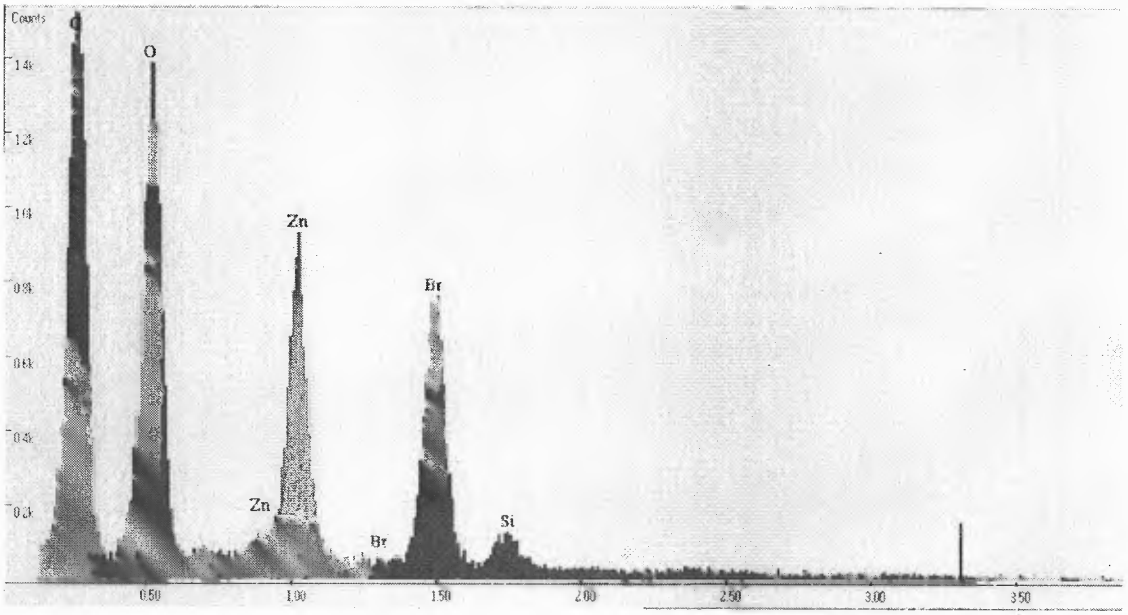

(c)

Figure 3.10 EDX analysis of sintered unetched Ag-Si-M alloy. (a) Zn particle embedded in sintered Ag-Si –M alloy, (b) Close view of Zn particle, and (c) EDX analysis of Zn crystal (point A) in (a).

3.4 Discussion

Based on the preceding observations, it is clear that open systems such as front Ag contact formation mechanism cannot be explained by using phase diagrams alone. The presence of various elements (i.e., Ag, lead borosilicate glass, Bi_2O_3, ZnO, SnO, Si, SiN:H, binders and inorganics) at higher temperature and short cycle time complicates the understanding. In the next subsections, the reactions between different materials that are present at the interface and a hypothesis of contact formation mechanism of Si solar cells will be discussed.

3.4.1 Silver-Glass Interaction

Some authors (Hilali 2005, Ballif, 2003, Grupp, 2005, Kyoung-Hook Hong, 2009) have suggested that, at elevated temperatures (>650°C), the molten glass dissolves Ag. The melting mechanism of Ag in glass is not discussed in detail. A typical solar cell observes peak firing temperatures (650-800°C) only for a few seconds. In such a short time, amount of Ag dissolved in glass is very small (Shubert, 2006).

Based on our experiments, we suggest a different mechanism for Ag–glass interaction. The amount of glass frit in silver paste is about 5-8 wt %. Since the paste is mixed prior to deposition, every Ag particle can be assumed to be coated with thin glass layer (i.e., see Figure 3.4). At elevated temperatures, the molten glass may contain Ag in the form of ions. This is because the submicron size silver particles have irregular surfaces which act as a source of these ions. At firing temperatures (500°C), some unknown amount of solvent metals (M) such as Pb, Zn, Sn or Bi contained in glass will be in ionic form (see Figure 3.11). Exact amount of solvent metal is unknown as the paste composition is proprietary information of paste manufacturers.

Depending on the composition of the frit, any one or combination of these ions will interact with silver through ion exchange. The amount of ions required to form thin layer of Ag-M alloy on micron sized particles is small (see ternary diagram in Figure 2.4b). The melting point of Ag-M alloy is much lower than Silver particles. The sticky coating on silver particles helps in creating agglomerated/fused (i.e., sintered) mass of silver particles. It is important to point out that, in optimal solar cell firing conditions, appreciable increase in size of silver particles was not observed (see Figure 3.1).

Sintering mechanism (i.e., coalescence) of silver particles in solar cells can be considered a special case of transient liquid phase sintering. However, unlike transient liquid phase sintering, there is no mass liquid flow around the matrix of silver particles. Low melting point Ag-M alloy on silver particles helps in forming a lateral conducting path for the finger/bus-bar system. The thickness of the coating increases with increase in temperature and time. On the flip side, thicker coating can increase the series resistance of the finger/bus-bar.

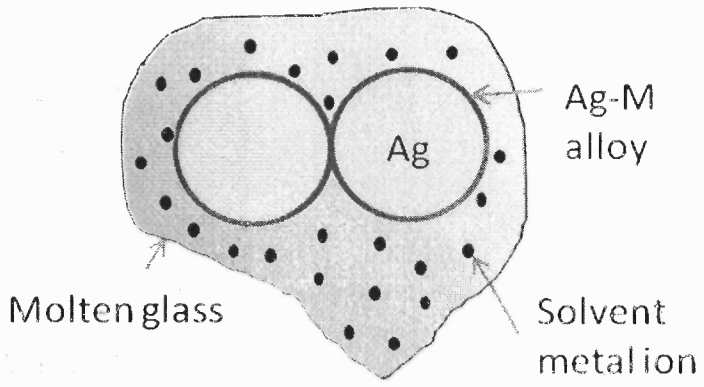

Figure 3.11 Schematic explaining Ag-Silver interaction and sintering mechanism.

3.4.2 Glass–Silicon Interaction

It is well known that molten glass etches the underlying silicon. The etch rate depends on the temperature, crystal orientation, defects and glass composition. Glass provides anchorage (i.e. adhesion) points for the metal grid to stick to silicon surface. Silicon is a known reducer and reduces some metal oxides in the glass (Young & Carroll, 2000). Glass silicon reaction results in thicker glass (i.e. more SiO_2) and shallow pits on silicon surface. Thicker glass at the interface can increase contact resistance and reduce FF of the cell. However, the junction depth of solar cell is only of about 0.3-0.5μm. Thus, chances of creating junction shunt increases if there is more glass-Si interaction. There is also a loss of phosphorous from the emitter into glass and hence decrease in V_{oc} (Sopori, 2007). So, only shallow (≈0.1μm) glass-Si interaction is desired.

3.4.3 Silicon-Silver Interaction

In the firing conditions used for typical solar cells (few seconds at a peak temperature of < 800°C), Ag-Si reaction rate is very small. Experiments by Shubert, 2006 and Young and Carroll in 2000, show very little interaction between Ag and Si in the absence of glass. The diffusion coefficient (D) of silver in silicon measured by Chen et. al. is 10^{-15} cm^2/sec. The experiment involved firing evaporated Ag film on single crystal silicon for 700°C for 30 minutes. Similar process conditions are unlikely in screen printed solar cells. Most of the values are extrapolated from higher temperatures (1100° C), i.e., D = 10^{-12} cm^2/sec.

3.4.4 Silicon-Silver Alloy

Various scientists (Hilali et. al., Ballif et. al., Shubert et. al., Grupp et. al., Huljic et. al., Kontermann et. al., Khadilkar et. al.) have reported the presence of Ag crystallites below metal contacts. These can be of pyramid shape for <100> Si or lens shape for <111> Si. In textured multi-crystalline Si cell, different shapes of crystallites based on various orientations are expected. These crystallites are reported to originate at the interface of the finger and Si. The size of these crystallites varies from 100 nm to 300 nm (Hilali et. al.). Silver re-crystallizes on etched Si from molten glass (Ballif et. al.), gets trapped in re-crystallized Si layer (Hilali et. al.) or is supplied by lead to Si surface (Shubert et. al.). In most areas of the contact, a layer of glass separates them from the bulk of the finger but, in some areas, a direct contact between the bulk of the finger and crystallites is expected. It was reported by these authors that, crystallites behave as current collection points. Hence, they play an important role in current collection capability of fingers.

In a typical solar cell firing process (peak at ≈800°C), the cell is above 700°C for only few seconds. The melting point of Ag is 961.93°C. Solar cell firing cycle is kept short (<180 seconds) to prevent impurity (Fe) segregation/precipitation or prevent them from going deep in the cell. Impurities can be introduced from furnace atmosphere (i.e. Refractory, Quartz Muffle, and Belt) also. During this small time interval, the amount of dissolved Ag is very less (Schubert, 2006). Further re-crystallization of Ag has a time constant. The emitter or the n-type region in a typical solar cell is less than a micron (i.e. <0.5 micron). The grown crystallites are expected to be 0.2 micron deep in emitter. At this depth, J_{02} (saturation current density in space charge region) will increase. Filament diffusion of Ag from these crystallites is possible. In mc-Si cells, the presence of grain

boundaries increases the Ag diffusion (Cheek & Mertens, 1984). In the worst case, it may shunt the junction. In this work, in c/s mc-Si cells, no crystallites at the Ag finger-silicon interface (see Figure 3.8) were seen. It is believed that, at elevated temperatures (>550°C), the glass frit is molten and etches the SiN:H (≈70nm thick ARC). The glass frit brings the Ag particles in direct contact with the Si. The glass, depending on the grain orientation, etches the silicon isotropically or anisotropically. Solvent metals (e.g. PbO, ZnO, SnO) present in the glass reacts with the outer layer of Ag particles and create Ag-solvent metal alloy. This alloy fills the pits etched by the glass on the silicon surface. Hence, on isotropically etched silicon, it appears as round shape and, on anisotropically etched silicon, it appears as inverted pyramid. As mentioned before, cleaved samples have striations and hide the surface details. Thus, many researchers erroneously detect it as Ag crystallite.

3.4.5 Silver-Glass-Silicon Interaction

Front contact formation can best be understood after considering the combined effects of Ag, Si and glass frit (i.e., PbO, B_2O_3, ZnO, Bi_2O_3 and SiO_2). At elevated firing temperatures (>500°C), glass dissolves/etches the SiN:H (≈70nm thick layer) and brings with it the Ag particles to Si surface. Glass incorporates SiN:H as nitrides (Young et. al.). At high temperatures, some of the liquid glass will make globules/ or blobs. Thus, at the interface, ≈ 30% area will be occupied by glass globules. It is important to note that glass globules can be found throughout (i.e., lateral and across) the depth of the finger/bus-bar structure as well (see Figure 3.1).

Since there is no movement of silver particles, only Ag particles near the Si surface will take part in Si-Ag-M interaction. The Ag-M alloy coating on the Ag particles interacts and alloys with the silicon at peak firing temperature. The reaction is shallow (< 0.1μm deep) and non uniform (see Figure 3.4). Areas where Ag-M alloy coated Ag particles can react with Si to form Ag-M-Si alloy (silver rich area) are limited by temperature and time constraints of solar cell firing cycle. In some places, at the interface, a very thin layer of glass (≈<80Å) may be trapped between coated particles and Si. Carriers can still tunnel through the layer (Grupp et. al., Shubert et. al.). In the current work, these are called as silicon rich regions. Since thick screen printed silver paste will always have glass. We will have a distribution of silver rich area, silicon rich area and glass globules at the interface of finger/bus-bar and Si.

3.4.6 Proposed Model for Contact Formation and Current Conduction Mechanism

Based on the time-temperature profile and the SEM images of the cross-sections, a model for contact-formation mechanism is presented in Figure 3.12. A mechanism (Sopori, 2007), which involves diffusion of Ag into the glass around Ag particle or a cluster of Ag, followed by accumulation of M around the Ag particle is presented. This mechanism is expected because at or near firing temperatures, the diffusion of Ag into glass can occur readily (see Section 3.4.1 and Sopori, 2007). A thin layer of liquid glass surrounds the Ag particles. There is ion exchange between diffused Ag and ions of solvent metal (M, where M can be Pb, Sn or Zn etc) in the glass. Because Ag and M can spontaneously react to form an alloy of much lower melting point, this mechanism leads to the formation of a melt around the Ag particle. Figure 3.12 illustrates various stages of this ion-exchange like mechanism.

Figure 3.12a illustrates an initial phase of Ag and glass. Here, glass containing a solvent metal is un-melted and separated from Ag. Figure 3.12b, depicts Ag particles in a molten glass matrix when the cell is heated. Because the glass frit contains other glasses as oxides of Pb, Zn, or Bi, these metals can exist as ions in the molten glass. Ag particles can exchange Ag ions with the solvent metal ions. Figure 3.12c illustrates a solvent metal ion (e.g., Pb or Pb substitutes) in a mobile state (ionized within glass from PbO) to diffuse towards Ag, while a Ag ion diffuses into the glass. The solvent metal ions will interact at the surface of the Ag particle forming a surface melt. Figure 3.12d illustrates the formation of a melt at elevated temperatures, around Ag particles and agglomeration of such particles caused by joining of the peripheral melt.

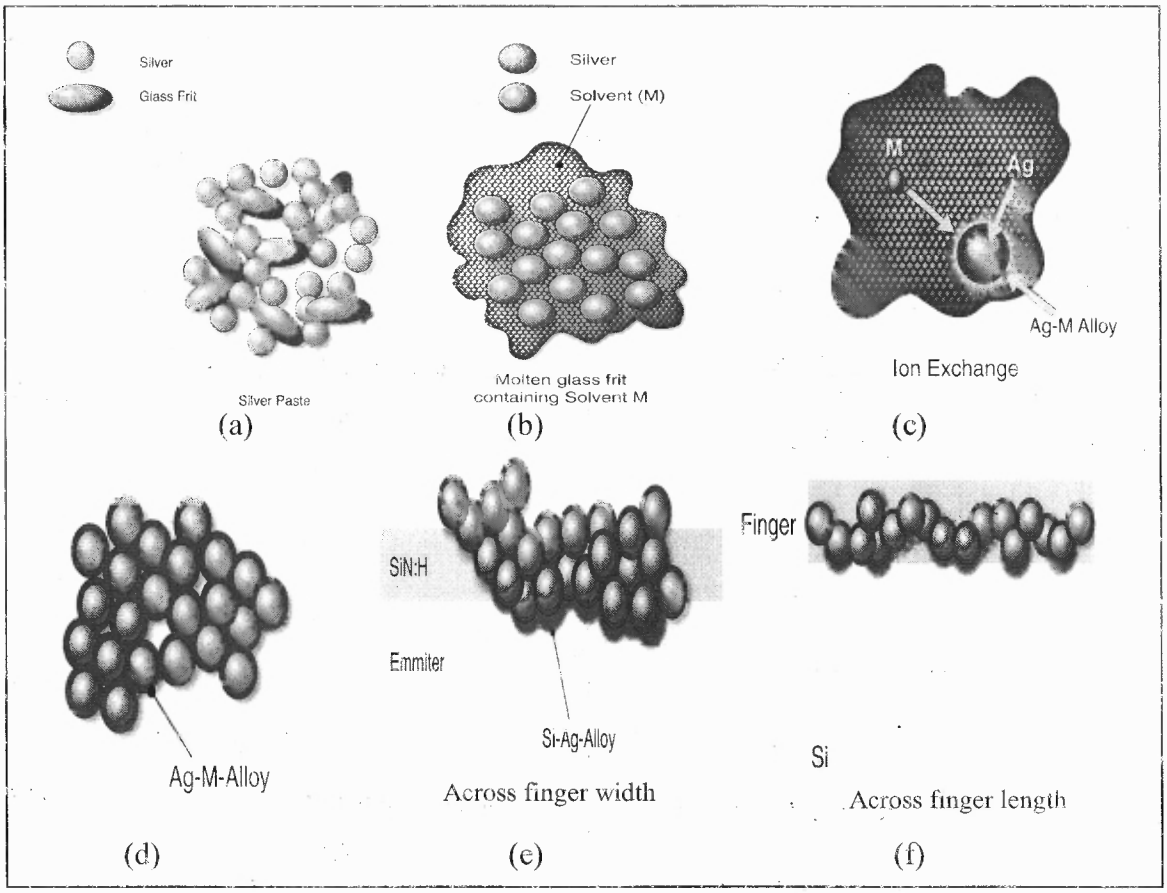

Figure 3.12 Schematic of ion exchange model for contact formation mechanism.

Thus, this process leads to the formation of a chain of clusters of Ag particles within the bulk of the ink, further leading to lateral conductivity of the ink pattern. The Ag particle with a molten periphery experiences enhanced melting because of the catalytic action of Si. Si helps to reduce PbO (or the MO) in the molten glass matrix, leading to the formation of Ag-M-Si alloy. This alloy formation can occur at considerably lower temperatures than Si-Ag eutectic formation. This reaction is illustrated in Figure 3.12e. Because clusters of Ag particles are joined together, they provide a lateral current flow path as illustrated in Figure 3.12f. It can be said that Si-Ag interaction occurs locally over a small area. The composition of this molten alloy depends on many factors such as the composition of the glass frit (particularly metal ions) and the highest temperature during firing. The thickness and spread of the alloy layer depends on factors such as temperature, time, and the concentration of P at the Si surface (sheet resistance of the N^+ layer at the surface). The third stage of the process involves the cool-down. During this stage, the molten constituents solidify. As the Si-Ag-M alloy solidifies, it is likely to produce a grading in the composition of the interface between Si and Ag.

Thus, diffusion and ion exchange can play a crucial role in the formation of a laterally "linked' Ag and in the formation of Si-Ag-M alloy. The exact kinetics of these reactions is not well understood at this time, but is being investigated. It is important to point out that the role of ion exchange can explain many observations reported in the literature. These include the formation of Ag crystallites and enhanced Si-Ag melt formation.

CHAPTER 4

STUDY ON EFFECT OF GRID ON TEMPERATURE DISTRIBUTION OF mc-Si SOLAR CELL DURING FIRE THROUGH CONTACT METALLIZATION

4.1 Introduction

Contact firing of a solar cell aims at forming a uniform contact by making metal-Si interaction as uniform as possible and limiting it to the near–surface region. Because a typical screen-printed Si solar cell has a front metal pattern, which creates a shadow, it is expected to create a non uniform temperature distribution during optical firing. The degree of non-uniformity would depend on many factors, which include the mass width and optical properties of the metal. Also, understanding the temperature distribution in the cell, as it heats up from room temperature, gives us an idea about how the heat is getting absorbed and distributed within the cell. Firing profiles of cell and furnace design can be modified (e.g. more tunable heating zones for uniform temperature distribution (±3°C) on cells) to process cells with higher fill factor (>85%).

In this chapter, a study of the effect of metal grid on temperature distribution on the cell during firing conditions is presented. First, an introduction is given that explains the importance of this study. Next, experimental details of the study are discussed. Experimental results are presented and explained. A finite element based commercial software, Comsol multi physics, was used to study the temperature variation. Details of the various assumptions and a thermal model are described. Results of the calculations are presented and discussed.

Besides the metal grid, temperature distribution profile of the crystalline Si solar cell also depends on other factors such as surface texture, anti-reflection coating, doping concentration, shape of fingers, edge effects, Si-Al interface etc. The temperature non-

uniformity during high temperature step can affect the fire through contact metallization process of the solar cell (see Chapter 3). This can degrade electrical and mechanical properties of the cell. Temperature variation can affect the front Ag contact formation mechanism (e.g., non-uniform Ag-Si alloying and creation of shunts). In this chapter, first experimental results of the various time-temperature profiles will be presented and then thermal modeling will be used to explain the non-uniform temperature distribution. The effect of grid pattern on thermal balance of silicon solar cell during firing has also been discussed in detail in the literature (Sopori et. al., 2007)

4.2 Experimental Details of Temperature Profiling of Si cells During Co-Firing

Experiments aim to: (i) Precisely determine the temperature at the Si-metal interface during contact formation so that one can apply information from phase diagrams as a guide to project the degree of melting and composition of the Si-Ag alloy, (ii) Map temperature distribution across the lateral surface of the solar cell during actual cell firing.

Accurate measurements of temperature of solar cells during actual firing are an issue. While Shubert, in 2005, has used a non-contact pyrometer, Kim et. al., in 2006, have simply placed the thermocouple tip on to the wafer (no cement) and measured temperatures. The pyrometer field of view, type of surface being measured, spectral response, temperature range and mounting environment, mounting limitations are some of the considerations to be taken into account. The wafer, during firing, experiences vibrations and can plastically deform at high temperature and hence the reading of a thermocouple that has its tip touching the wafer can have substantial errors in temperature reading. If the cell is on a moving belt which is a regular firing method, then

non-contact pyrometers yield incorrect temperature readings. In order to have a repeatable temperature measurement, a systematic thermocouple mounting method has to be developed. Figure 4.1 illustrates a typical arrangement to measure temperature of the screen printed mc-Si cells during contact firing. Thermocouples were attached to solar cells/ wafers to find the temperature distribution of the cells/wafer under various firing conditions.

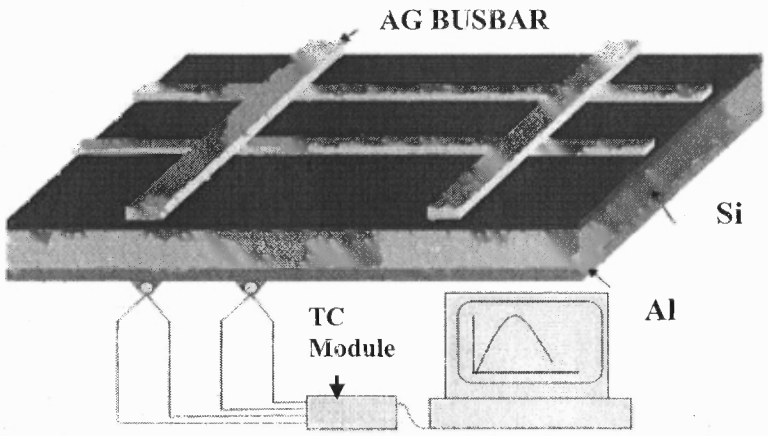

Figure 4.1 Set-up for time-temperature profile measurements.

In the present study, multiple K-type thermocouples were cement bonded onto the wafers, maintaining nearly the same thermal mass of each thermocouple (Sopori et. al., 2007). Surface characteristics of the sample, type of thermocouple cement, thermocouple wire diameter, and the amount of cement are some of the important parameters that require attention. Commercially available, Omegabond® high temperature CC cement with binder was used in the current work. Experiments by using water based cement were not successful because the adhesion of the cement to fired Al paste was poor.

K-type thermocouples are cheap, widely used and reasonably accurate (±2.2°C). To extend their life and to prevent them from being exposed to furnace gases, they were enclosed in double hole ceramic sleeves. One thermocouple was located directly below the bus bar, whereas the other was away from it. Two feet long, kink free, 0.01inch diameter K-type thermocouple was used. A thicker K-type shielded extension wire was used to carry weak (mV) thermocouple signals. The thermocouple output was measured using a multichannel amplifier and software, which converted the voltage outputs to temperature profiles at the different locations of the cell during actual firing.

Single crystal wafers with one side polished and solar cells were used in the current work. As is common knowledge, a dust particle free, oil free, surface gives good a adhesion surface to the cement. Wafers were cleaned in HF (3-5%) and DI water rinsed just before mounting the cement. Mounting thermocouple on unfired cells was a challenging task as furnace dried (e.g. max 150°C) screen printed back contact Al paste is flaky and peels off along with the cement. Hence, pre-fired solar cells were used for experiments of temperature distribution measurements. The cells were replaced after few (3 or 4) firings.

To study the temperature distribution inside the furnace, a thermocouple mounted wafer was placed at various locations (e.g., left, center and right position) inside the muffle. Gas flow rate was also considered as a parameter. To measure temperature distributions on a solar cell, multiple thermocouples (3, 5 or 8 nos.) were mounted on the wafer mainly near edges, below bus-bar and central location.

4.3 Results of Cell Temperature Profiling

Figure 4.2 shows a plot for a typical firing cycle of the cell. Temperature (°C) is plotted on primary y-axis and light intensity signal (V) on secondary y-axis. It is seen that the peak temperature is lower under the bus bar as compared to the area away from it. This is an important observation because it shows that the Ag-Si alloy formation occurs at a lower temperature than the Ag-Si eutectic temperature of 835°C. This reduction of eutectic point can be explained by invoking the influence of other metal oxides present in the glass (e.g., see Section 3.4.1). Time-temperature (t-T) profiles generated indicate that, in presence of glass, the Si-Ag interaction occurs at significantly lower temperatures than previously thought. Details of this interaction have been discussed in Chapter 3.

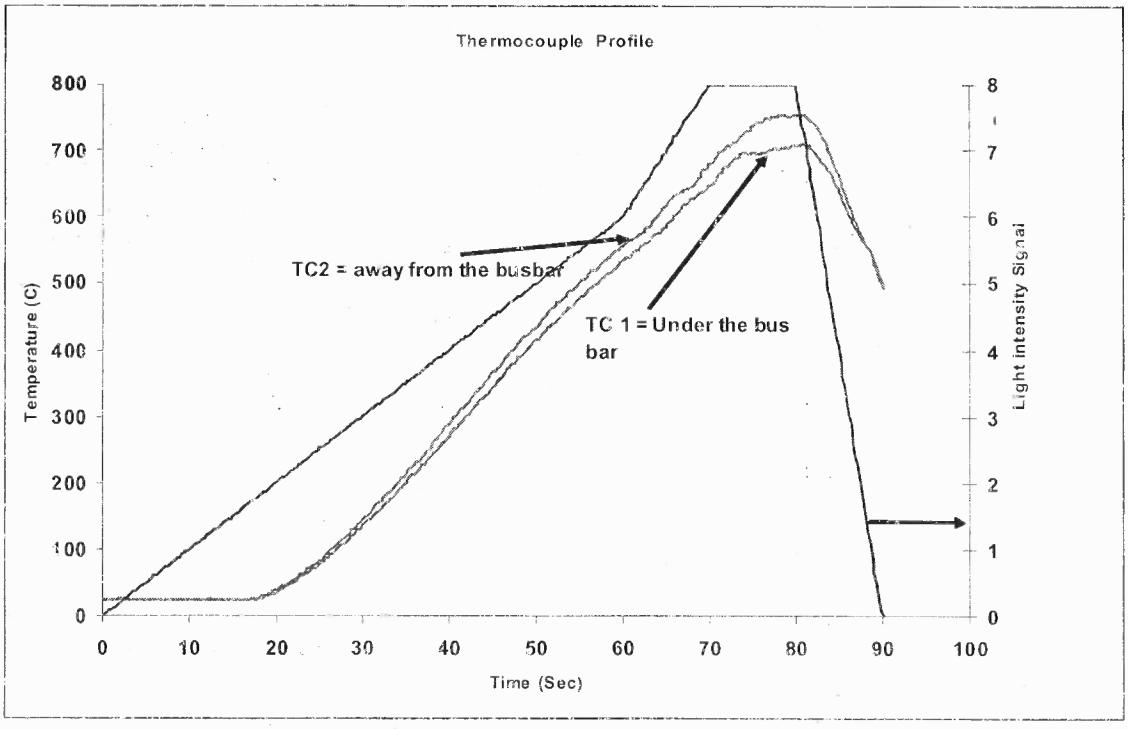

Figure 4.2 Measured temperature profiles (in °C) under a bus bar and away from it during a fire-though process corresponding to the input optical flux.

This time-temperature study can lead to more accurate control of the cell firing profile. For example, a short time (<5 seconds) duration at peak temperature of 780°C) can be sufficient to form a reasonable (ρ_c <0.3mΩ.cm^2) front contact. Figure 4.3 shows a t-T profile of a cell fired during optimal firing condition. One thermocouple was cemented at the central location of the cell. It clearly shows that the amount of time spent at peak temperature is only a few seconds. A longer baking period was utilized because currently the furnace is only capable of firing one cell at a time. In Figure 4.4, a typical application of t-T profile is shown. The temperature difference between individual thermocouples attached to various regions (e.g., center, edges and below bus-bar) of the cell was measured and light intensity signal to lamps was adjusted accordingly. A schematic of the location of the thermocouple on a solar cell is shown as inset in Figure 4.4. Similar experiments were carried out in optical processing furnace to determine the flux distribution and finalize optimal firing conditions for solar cell processing.

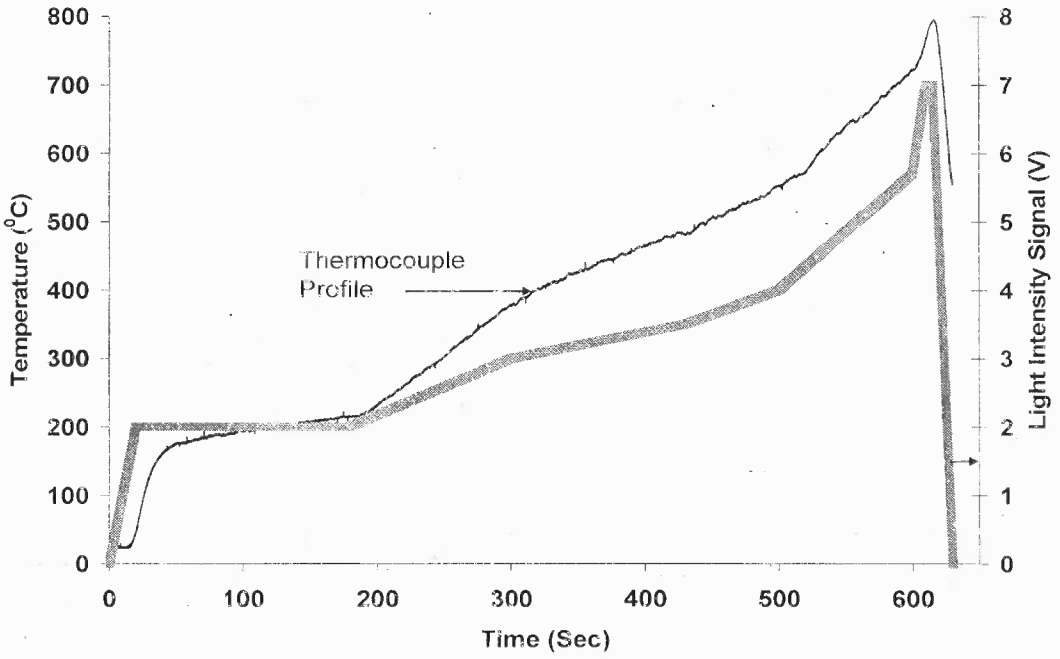

Figure 4.3 A typical firing profile along with measured cell temperature for Si solar cell.

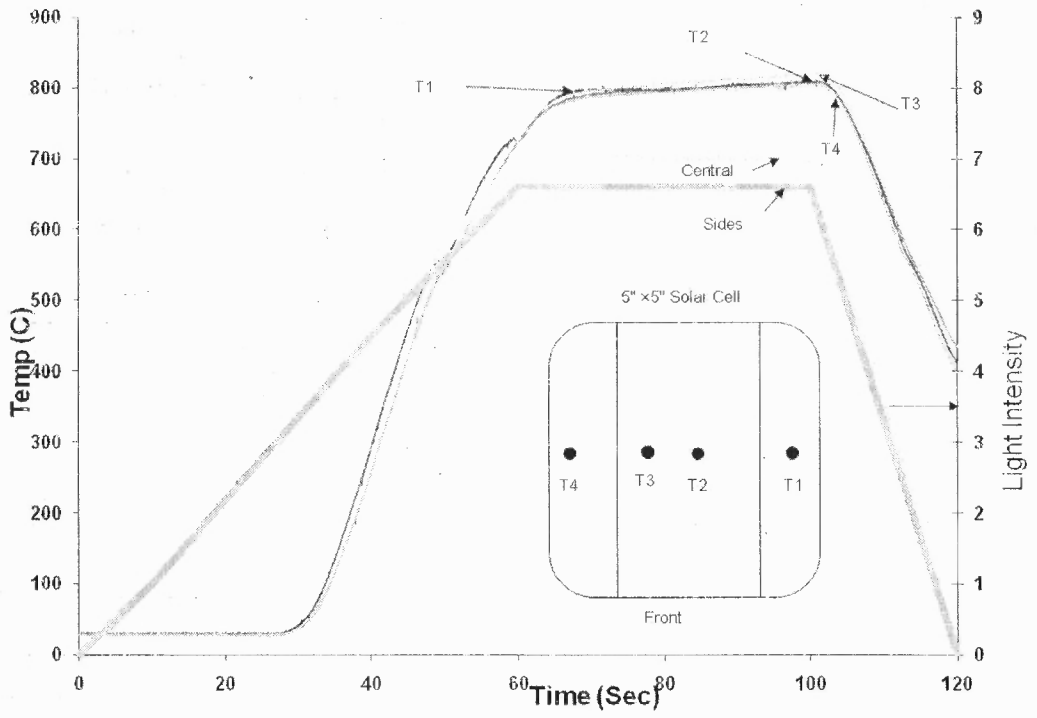

Figure 4.4 Temperature time profile (T-t) of a solar cell with four attached thermocouples.

4.4 Thermal Modeling of Effect of Grid on Cell Temperature Distribution

Thermal modeling was performed to verify the experimental results. To study the role of grid in determining the cell temperature distribution, a commercial software, Comsol multi-physics, was used. It is based on solving partial differential equations using finite element methods. The software runs the finite element analysis together with adaptive meshing and error control using a variety of numerical solvers.

Temperature distribution in cell/wafer for a fixed value of heat flux was calculated in 2- and 3- dimensions. Heat is defined as the energy transferred by virtue of a temperature difference (Incropera & DeWitt, 2001). The mathematical model for heat transfer by conduction is the heat Equation 4.1.

$$\delta_{ts}\rho C_p\frac{\partial T}{\partial t} - \nabla\cdot(k\nabla T) = Q \qquad 4.1$$

$$q = -k\nabla^2 T \qquad 4.2$$

Where, T is the temperature, ρ is the density, C_p is the heat capacity at constant pressure, k is thermal conductivity, Q or q is a heat source or a heat sink, δ_{ts} is a time-scaling coefficient (usually taken as 1).

In steady state condition of heat transfer, there is no temperature variation with time. Thus, the first term containing ρ and C becomes zero. If the heat transfer is by conduction only, q is instead determined by Equation 4.2.

In transient state conduction, Equation 4.1 is used. In this particular study of transient state conduction, temperature varies as a function of time. It gives the heating behavior of various regions of the cell as temperature increases from room temperature to until equilibrium condition (e.g., steady state) in cell is achieved in the furnace.

4.4.1 Assumptions

Single crystal Si wafer was used as substrates in the current model. Because of high thermal conductivity of Si, the effect of grain boundaries has been neglected. Hence, this model is also applicable to mc-Si solar cells. Heat flux (q) of 98000W/m^2 was applied on the top surface of Si wafer. The value of heat flux was determined as that required to increase the solar cell temperature to around 800°C (i.e., typical peak firing temp.). Heat loss was assumed from the rest of the exposed Si surfaces. Surfaces of silver bus-bar and fingers were considered 100% reflective and only heat loss was assumed from their surfaces. Heat loss was assumed from all exposed surfaces of the Al back contact. The thermal resistance between Si and Ag layer and Si and Al is neglected as liquid paste of

metal is applied using screen printing method. Continuity conditions were applied to Ag-Si and Si-Al interfaces. Heat flux was applied from the front side (SiN:H). Solar cell is a composite structure of various materials such as Si, Ag, and Al. As the structure heats up, its thermal conductivity undergoes change because of phonon scattering.

The TC (Thermal Conductivity) of pure Si decreases as temperature is increased due to phonon- phonon scattering. In metals, the electrons take part in thermal conduction. Thus, TC of metal increases as temperature rises. The simulation assumes no change in the TC in either material. The simulation ignores the effect of convection on the cell temperature. During firing, there is compositional change occurring in the front Ag contact. The binder in the silver paste evaporates as temperature increases. There is shrinkage of the contact that occurs as a result of sintering. Both front Ag and back Al contacts are made up of screen printed paste and undergo phase transformation during firing. This can have impact on emissivity. The simulation ignores these changes. The fingers are drawn as rectangular boxes. Normally, the fingers have rough convex surfaces. This type of geometry can affect the reflectivity. The simulation ignores effect of doping on thermal conductivity.

The screen printed Al is applied on the whole back side of the cell. During firing, there is inter-diffusion of Si and Al. The Al melts and solidifies during firing cycle. This change of phase will affect the thermal conductivity. As Al is molten only for a few seconds during actual firing, the simulation ignores this behavior. Si wafer/cells will have impurities (i.e. Fe, O). The amount of impurities found is much lower compared to host Si atoms. The simulation ignores effect of impurities.

As the cell temperature increases, there is an alloying reaction between Si and Al. The Si-Al interface becomes rough and the reflectivity changes. Light trapping is important for design requirement for state of the art solar cells. The simulation ignores this change in reflectivity of the Si-Al interface.

4.4.2 Model

Finite element modeling procedure consists of the following steps: (1) Draw the device, (2) Define the physics by specifying material properties and boundary conditions, (3) Create a mesh, (4) Select and run a solver, and (5) Post process the results. A 300 micron thick C-Si wafer with 155 cm^2 area was modeled. SiN:H layer was modeled by changing the emissivity of the top surface of the cell (Si). The front Ag contact was 25 microns thick. 40 microns thick screen printed Al was applied on the whole back side. Table 4.1, below, gives emissivity and TC values of various materials taken from the literature. Figure 4.5 is a schematic of the model showing direction of heat flux and various heat losses from the surfaces. Arrows coming out from the object indicates heat loss and arrow going inward of the object represents the difference between applied heat flux and radiation.

Table 4.1 Emissivity, TC, Density and Heat Capacity Values of Various Materials

Material	Emissivity, ε	Thermal Conductivity [W/ (m*K.)]	Density (ρ, Kg/m^3)	Heat Capacity (Cp, J/Kg K)
Si	0.64	163	2330	703
Ag	0.46	429	8392	235
SiN:H	0.95	163	N.A.	N.A.
Al	0.31	409	2700	900
Omegabond® CC cement	0.31	1.1530	N.A.	N.A.

Source: (Ibos et al. 2006), (Ravindra et al. 2003), http://www.omega.com/Temperature/pdf/OB_BOND_CHEM_SET.pdf

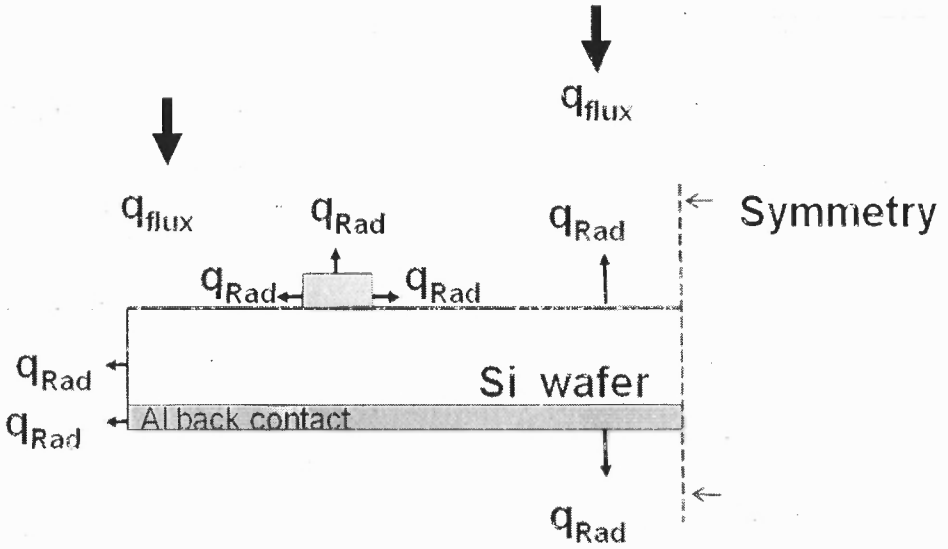

Figure 4.5 Schematic showing various flux input/output directions and various regions of the solar cell.

As the cell is symmetric, only heat input/loss for one half of the cell is shown. Since silver is highly reflective, only heat emission losses were assumed from fingers and bus-bars. Thus, no q_{flux} is applied to the fingers or bus-bar. Loss of heat flux $-q_{Rad}$ is given by,

$$-q_{Rad} = \varepsilon * \sigma * T^4 \qquad (4.3)$$

Where, σ is the Stefan-Boltzmann constant, its value is 5.670400 $Wm^{-2}K^{-4}$, T is the temperature in K and ε is the emissivity.

To simulate temperature distribution profiles of solar cells, initially, temperature profiles of Si wafers of various sizes were simulated to check the validity of the basic assumptions. Calculations were performed for textured Si wafers of 125mm and 156mm by changing the value of heat flux input. The mesh density was varied and optimal mesh density values were chosen. All simulations were performed by using Comsol

Multiphysics software. A 70 nm thick SiN:H is widely used as an antireflection coating in the fabrication of conventional mc-Si solar cells. In the current simulations, SiN:H was introduced by changing the emissivity of front Si surface and adjusting the input flux for change in reflectivity (Ravindra, Ravindra, Mahendra, Sopori, & Fiory, 2003). Al contact was added in geometry as 40 micron thick rectangles; below the rectangle is Si and thermal calculations were performed. Later on, front contact was added as grid pattern in geometry above the Si and temperature distribution was determined.

4.5 Results of Thermal Modeling

Figure 4.6 shows the temperature difference between top and bottom surfaces of Si wafer. As seen from Table 4.1, Si has a high thermal conductivity and Si wafers have large area in comparison to thickness; therefore, very little difference was expected. A temperature difference of 0.05°C was calculated at the center of 300 micron thick wafer. Hence the temperature variation across the wafer thickness can be neglected. The assumption of all the flux getting absorbed on Si surface is valid in the current simulations. The focus of the study was to determine lateral temperature distribution in wafer and subsequently of the solar cell. In the remaining part of the chapter, lateral cell temperature variation will be discussed. To study the mass effect of the attached thermocouple on the cell temperature distribution, thermocouple geometry was introduced as a square below the bus-bar and below the center of the wafer. A 2-dimentional steady state calculation was carried out. Figure 4.7 shows the temperature distribution effect inside the thermocouple dot on the wafer.

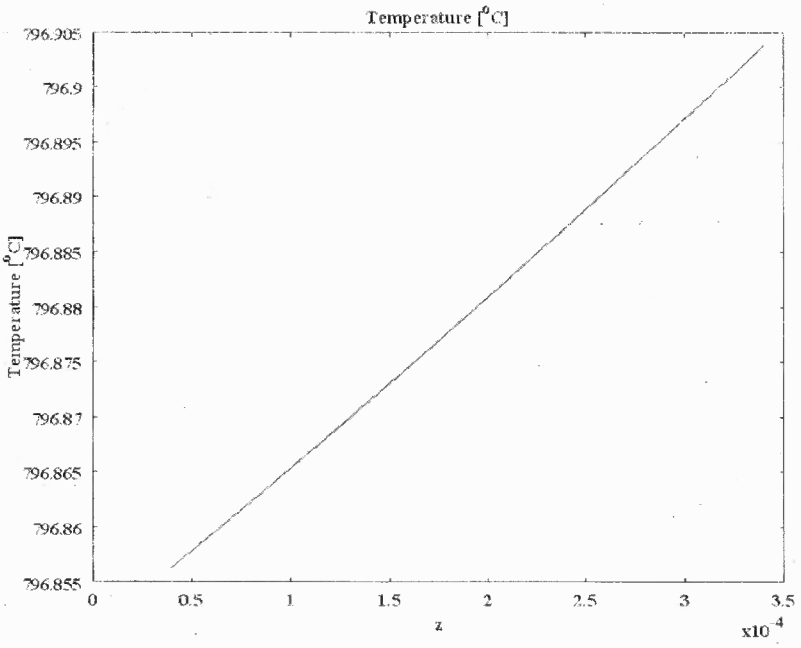

Figure 4.6 Graph showing simulated temperature profile across the thickness of Si wafer. Z is the thickness of the wafer in meters.

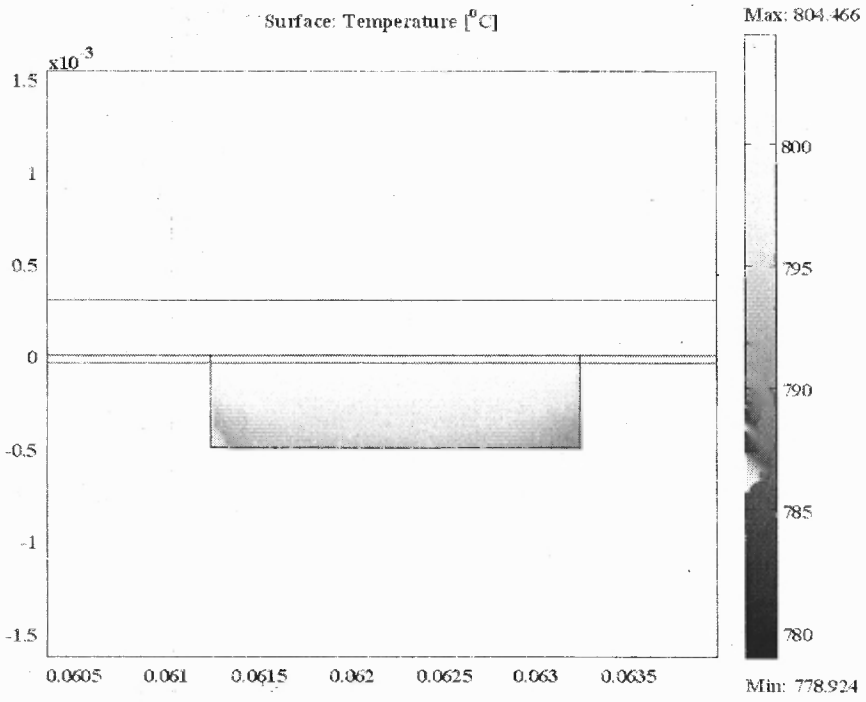

Figure 4.7 Simulation picture showing temperature gradient inside the thermocouple cement dot (e.g., 0.0025cm^2 area). The tip of the thermocouple (not shown) is generally touching the wafer.

Figure 4.8 below, shows that a drop of 9°C was calculated across the cement dot (area = 0.0025 cm^2). Also, since temperature difference between two thermocouple dots was determined, this affect can be neglected.

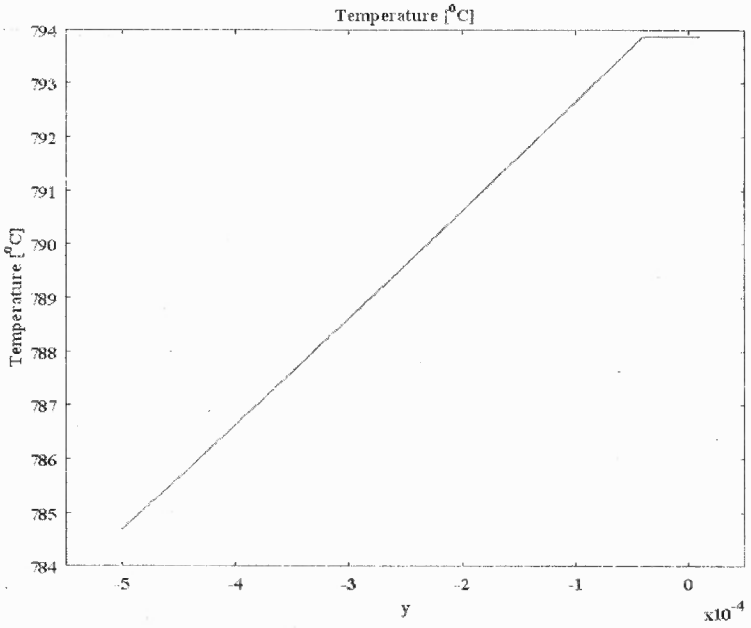

(a)

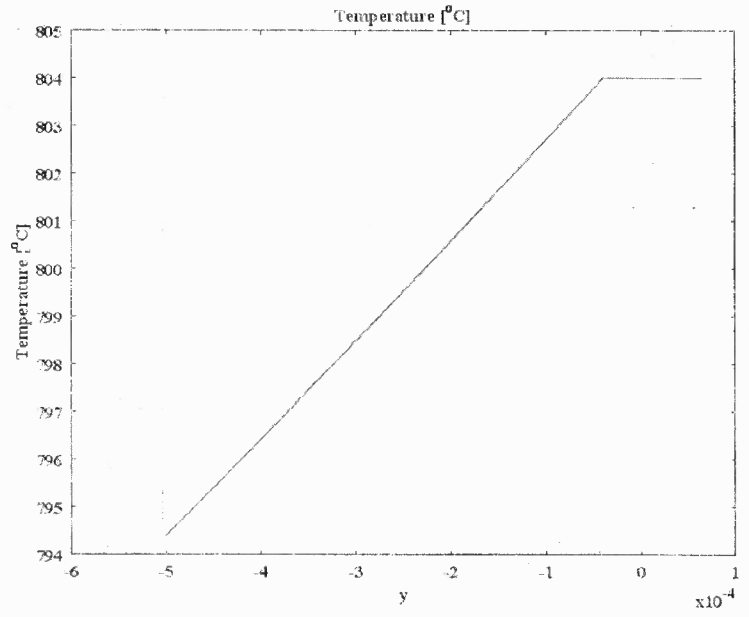

(b)

Figure 4.8 2-D steady state temperature distribution plots across the thickness of thermocouple cement dot, (a) below bus bar and (b) center of the cell.

To verify the various assumptions (see section 4.4.1), the model was initially tested on plain wafers. The heat flux was corrected for texturing. Figure 4.9 shows the temperature distribution of a 6 inch wafer by using 3D steady state condition equations. As can be seen from the figure, the four corners and four sides are cooler compared to the central region due to edge effect. Similar results were achieved for 4 inch and 5 inch wafers.

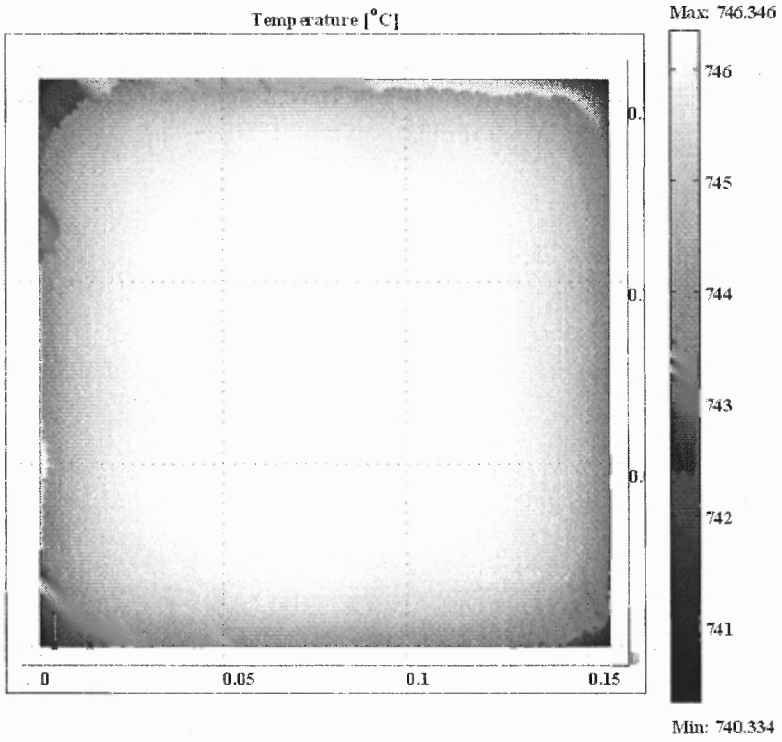

Figure 4.9 3D steady state temperature distribution profile of a 6 inch wafer.

Figure 4.10 shows the temperature distribution after adding SiN:H and back Al layer on the Si solar cell. SiN:H is used as antireflection coating and Al as back contact in solar cell. The flux was adjusted for different values of emissivity of SiN:H and Al. Low frequency plasma enhanced chemical vapor deposition technique is utilized to deposit 70 nm of SiN:H. This technique does create a damage layer (Sopori et al., 1996). A damage layer of few microns does not affect the thermal balance of wafer.

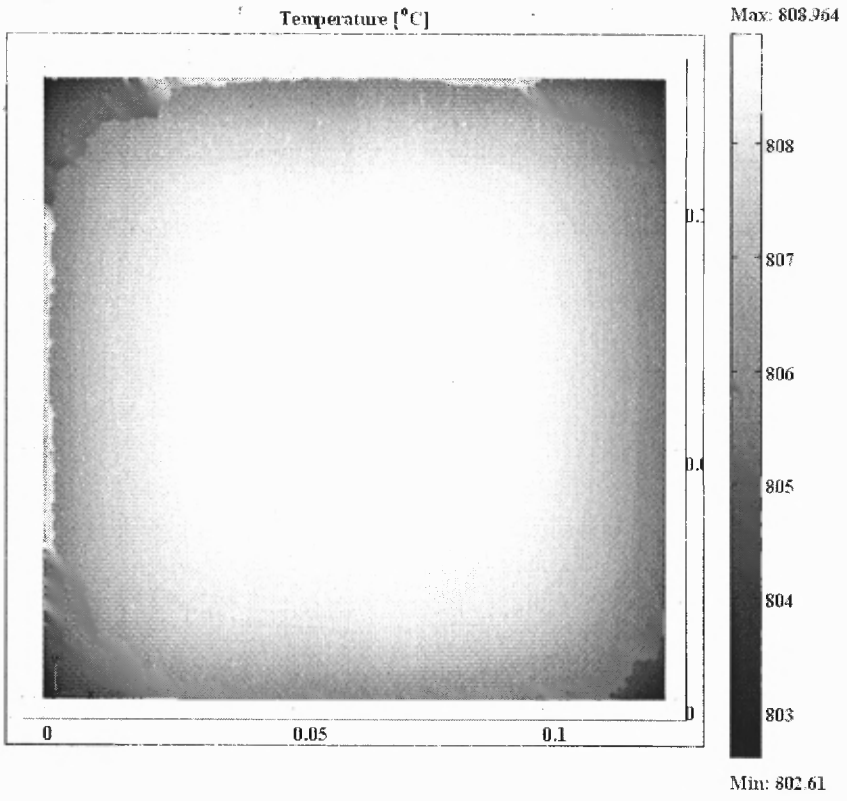

Figure 4.10 3D steady state simulation of solar cell with SiN:H and back Al.

Aluminum is applied as paste using a squeegee in a screen printing machine. Silicon is a fast diffuser in Al (10^{-8} cm^2/s, Sopori et al. 2009) at higher temperatures (550°C). As seen in Figure 4.11, there is also a lot of intermixing occurring between Al and Si. Also both Si and Al have high thermal conductivity; hence the thermal resistance between these two layers has been neglected. Screen printed back Al contact has a melting point of 660°C. Hence, the temperature uniformity of few degrees does not affect the molten Al at 800°C.

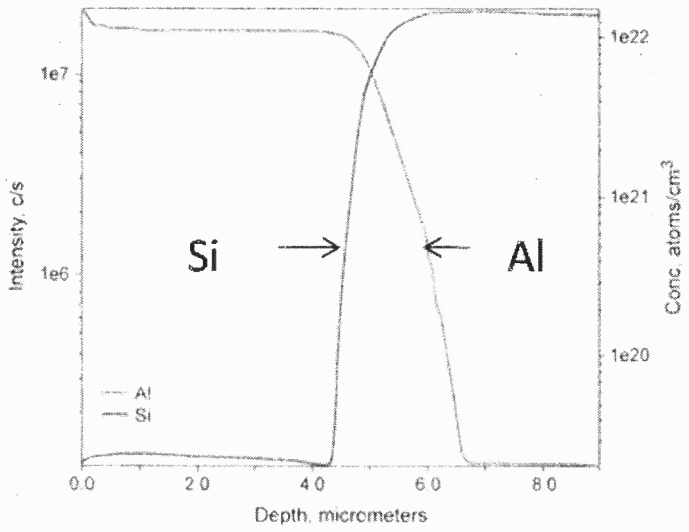

Figure 4.11 SIMS profiles of Si and Al for a sample processed at 550°C for 70 s.

To study the effect of the metal grid, initially, only bus-bar was introduced. Figure 4.12a shows the temperature distribution on the solar cells by introducing bus-bar (2mm wide) in the geometry. Bus-bar shadowing affects modify the temperature distribution of the cell. Figure 4.12b shows the temperature distribution across the centerline of the cell as one moves from left to right. Presence of bus-bar alters the thermal balance substantially. Although Si is believed to be thermally highly conductive, temperature gradients of greater than 10°C were calculated.

A typical conventional solar cell has bus bar extending all the way to edges on two sides. Thus, on these sides, the cell has more temperature non-uniformity because of the combined effect of the edge and the bus-bar. It is important to note that all charge carriers from front contact travel through the bus bars before being collected by the tinned Cu strips. Further, on four corners of the cell, there is lower temperature due to more edge area. As expected, the area between the two bus bars is hotter than the area between the edge and the bus-bar.

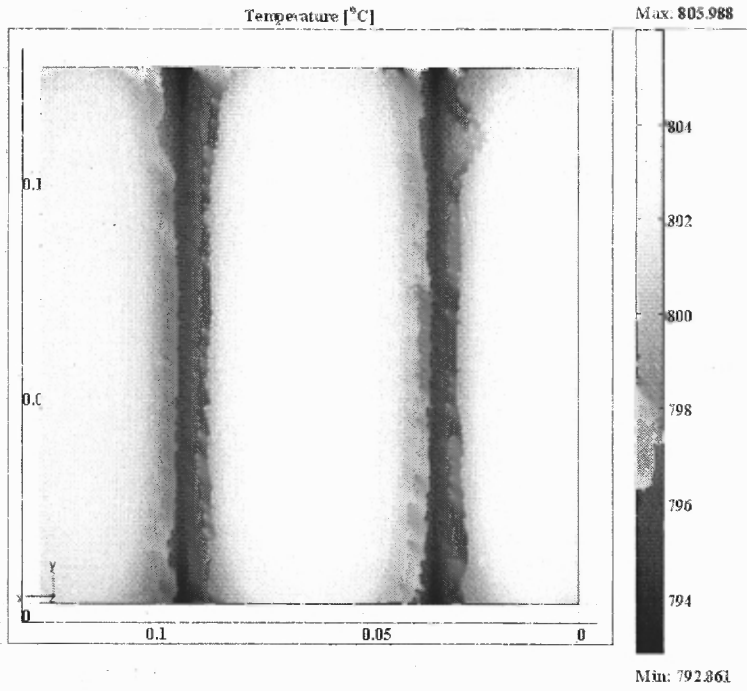

(a)

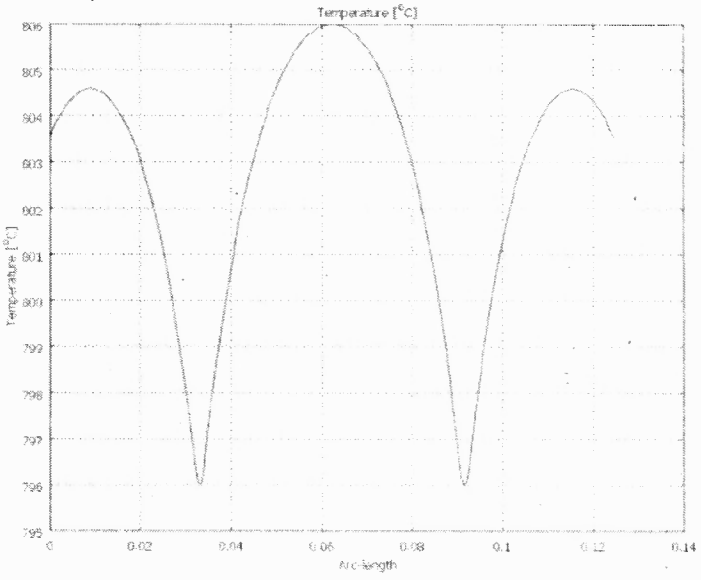

(b)

Figure 4.12 Simulated profiles of 125mm solar cell with bus-bar only, (a) Temperature distribution profile and (b) Temperature distribution plot across the width (i.e., arc length on the x-axis of the cell).

The temperature distribution becomes more non-uniform as one move diagonally from one corner to the other. It is important to emphasize that even on optimized cells the temperature distribution is expected. All this temperature distribution is also well evident in Figure 4.13 (a) & (b). It shows change in thermal gradient across the cell width as fingers were introduced in the geometry to complete the cell structure. There is a drop of 1°C across the width of the finger. Thus, the grid shadow will not directly affect the contact formation mechanism below the finger. The temperature drop across the bus bar region is about 10°C. For optimized cell, this can have significant impact. Process engineers might think of increasing the firing temperature higher so that the temperatures below bus bar can be at least 800°C but it may create shunt in other areas (i.e. central region).

While the edge effect is well known, its impact on the contact formation (i.e. Ag-Si interaction) and subsequent current conduction is not well studied. The edge effect can be reduced by proper f/c design (i.e., adding guard ring). But the shadowing effect cannot be reduced as it depends on the design of the metal grid. Both the photolithography and screen printed cell will have temperature distribution as shown in Figure 4.13.

3-D transient state calculations were performed to study change in temperature with respect to time. It is important to point out that change in TC, emissivity, absorption coefficient of Si, Ag and Al were neglected. They were carried out to study the heating behavior of cell as it is introduced in the furnace. Figure 4.14 shows cell after 5 seconds (Figure 4.14a) and 10 seconds (Figure 4.14b) of heating in furnace.

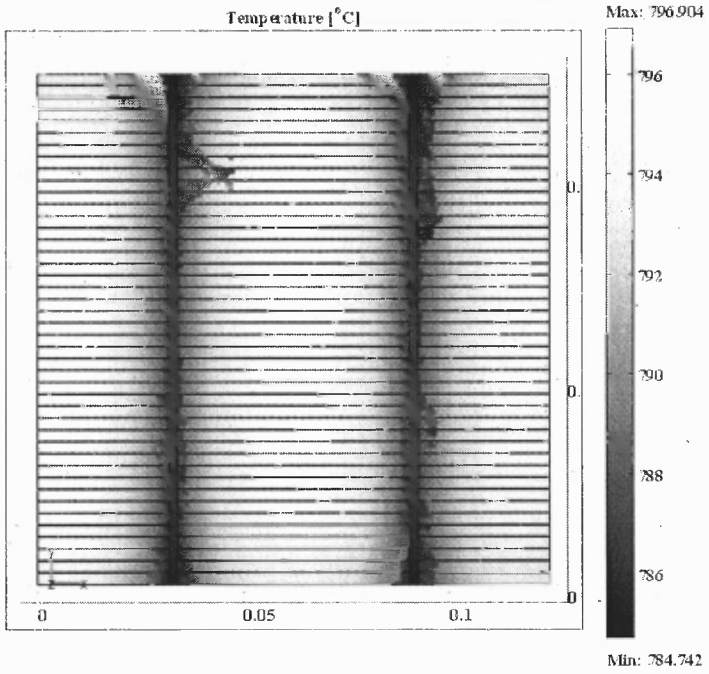

(a)

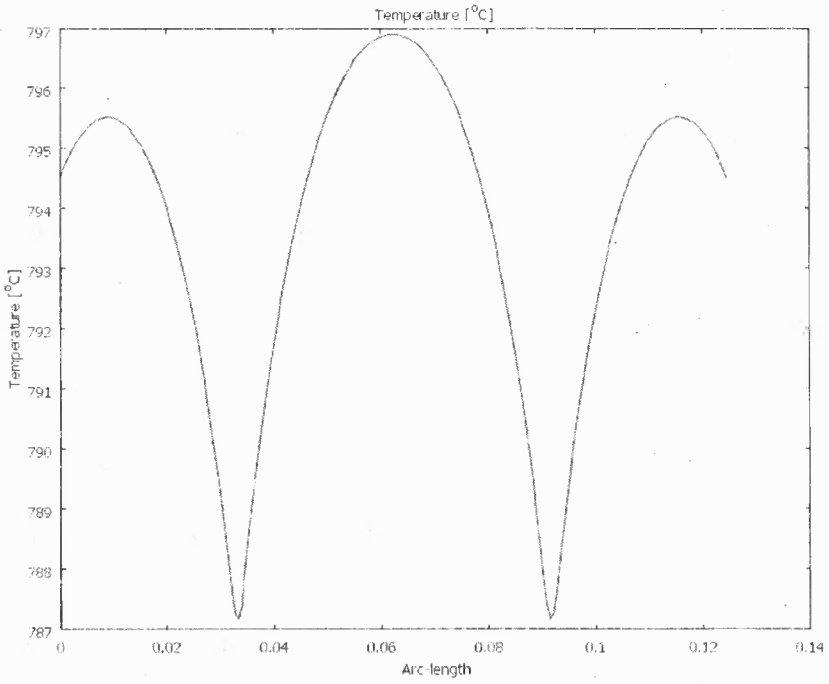

(b)

Figure 4.13 3D steady state simulation result of 125mm inch solar cell, (a) profile of temperature variation across cell, (b) Temperature distribution plot.

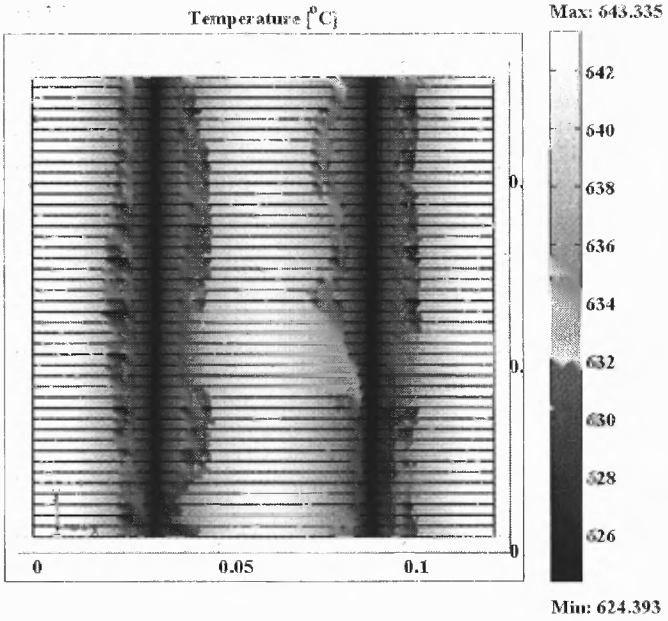

(a)

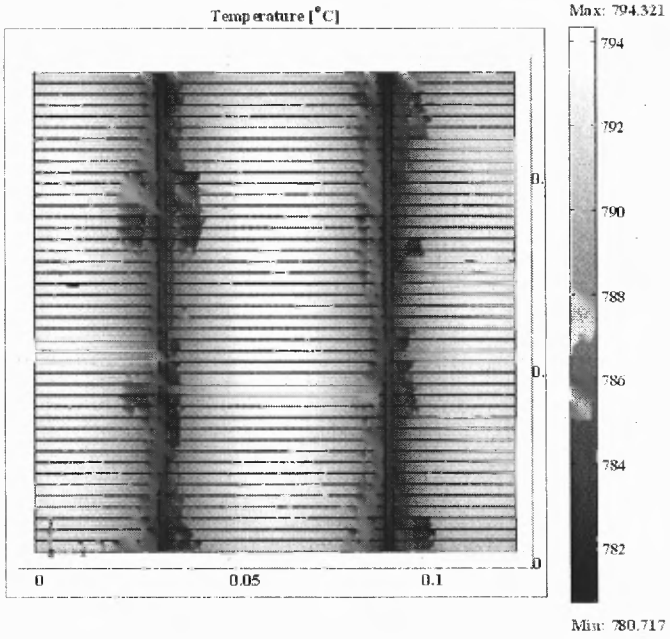

(b)

Figure 4.14 3-dimensional transient state temperature distributions on the cell in the furnace after (a) 5 sec (b) 10 sec.

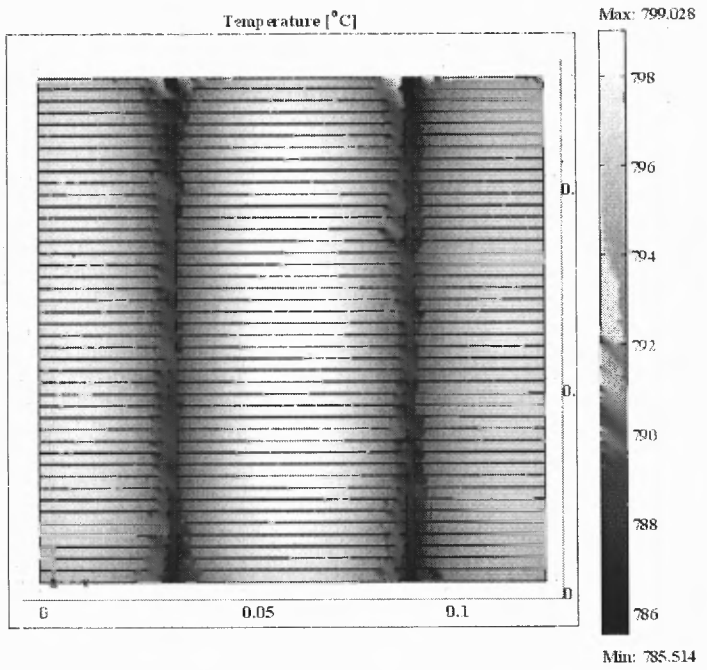

(a)

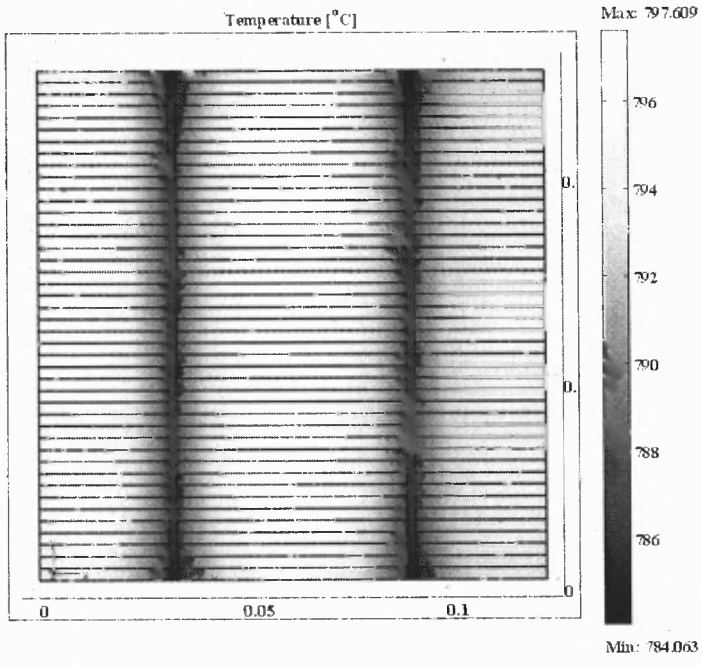

(b)

Figure 4.15 3D transient state thermal modeling showing heating behavior of the cell. After (c) 15secs, (d) 20secs.

It was calculated that the cell achieved steady state condition in 18-20 seconds. Near the edge of the cell, it takes 3 seconds longer to achieve the steady state condition because of edge cooling. It takes about 20 seconds for the cell to achieve equilibrium condition (see Figure 4.16). Figure 4.15a shows thermal profiles after 5 sec. The cooler region around the bus bar is initially wider and it shrinks at the center as time increases (Figure 4.15 b, Figure 4.15c and Figure 4.15d). The cooler region where the bus bar meets the edges does not shrink.

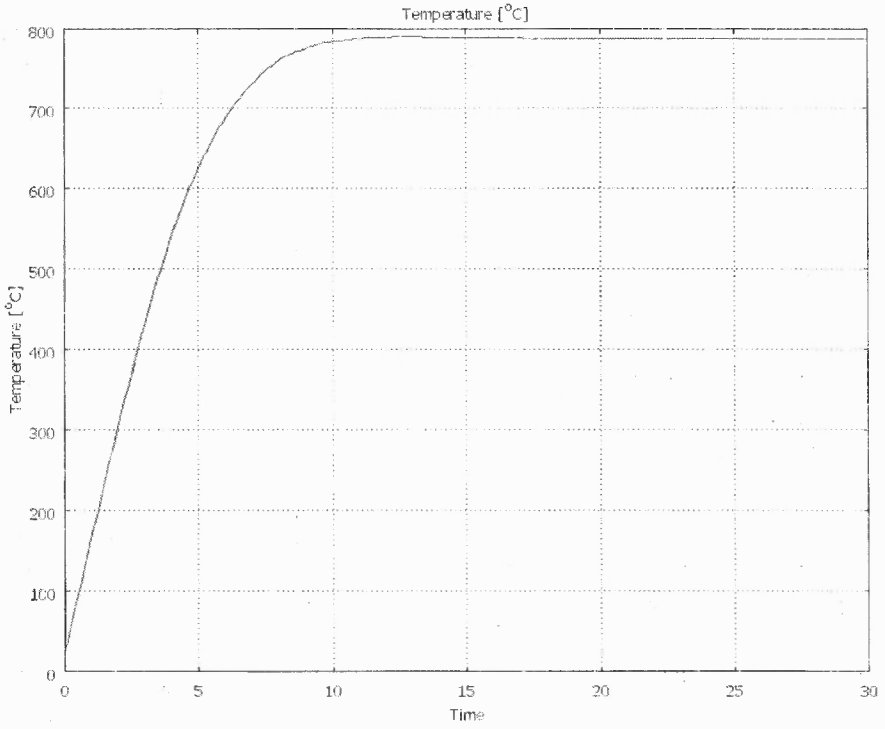

Figure 4.16 3-dimensional Transient analysis of temperature progression of a point at the center of the wafer for fixed flux amount.

Similar behavior is expected as the cell is cooled. The relatively lower temperatures observed below the bus bar during the experiments have found validation during simulation calculations.

4.6 Discussion

The solar cell front metal contact grid design is determined mainly by the sheet resistance of the emitter. The metal bus bar is intended to receive the carriers (i.e., electrons) collected by the individual fingers. The tinned copper strip is then soldered on the bus bar and charge carriers (i.e., electrons) are taken out of the cell. The commercial screen printing technology has limitation of printing about 80-125 micron wide fingers. It is desired that all region below the finger and bus-bar participate in the current collection mechanism. Analyzing the effect of front metal grid on the heating rate of the cell can be helpful in understanding the contact formation and current conduction mechanism. It is well known that the role of Ag-Si alloy/crystallites in contact formation is crucial in reducing contact resistance (Sopori et. al. 2007, Schubert, 2007). A nucleus for alloy formation is dependent on temperature among other things (i.e., lattice imperfection, grain boundaries etc). Temperature distribution has effect on mechanical (i.e., adhesion strength, bow etc,) as well as electrical characteristics of the cell. Mechanically, the front contact design is supposed to aid in compensating for the bowing effect of the back Al contact (Khadilkar et. al. 2005). Thus, uniform bonding of the fingers with underlying Si is also desired.

Impact on mechanical properties will not be discussed as it is beyond the scope of the present study. Effect on electrical characteristics will be discussed in the next section.

4.6.1 Impact of Temperature Distribution on Electrical Characteristics of Cells

Ag-Si eutectic is at 835°C (Olesinski, Gokhale & Abbaschian, 1989). The diffused emitter region of a typical solar cell is only ≈0.5 micron thick. The shallow emitter can be shunted by contact metal at higher temperatures. Thus the amount of Ag-Si interaction

has to be controlled. Solvent metals are added to silver paste to bring down the eutectic temperature. Conventional solar cells are fired around 800°C. Time interval at peak temperature is 5 seconds. The emitter doping is generally kept in the range of 1E+20 atom/cm^3. At this doping level, the current conduction from Si to metal is believed to be of field emission type (Schroder & Meier, 1984).

The series resistance and hence, the fill factor of the C-Si solar cell depend on the metal semiconductor contact quality and the conductivity of the metal (i.e., Finger/Bus bar/back metal contact in our case). Both the front contact formation and the current conduction mechanisms depend on how well the silver metal interacts with the silicon and glass frit. For large-area industrial silicon solar cells, the fill factor drops by about 4.5% absolute to 5.5% absolute per 1 W cm^2 increase in series resistance (Mette, 2007). A number of scientists have also observed non-uniform Ag-Si interaction below Ag grid but have not explained it in detail (See Chapter 3.3). This characteristic can have major impact in the current collection and consequently current conduction behavior of the contact. In sections below, impact of thermal distribution on current conduction and contact formation is discussed for fingers.

The Ag finger (100-146μm wide, 25μm thick) is thinner than a bus bar (2mm wide, 25μm thick). Thus, as expected, the temperature difference across the finger is very small (<1°C). However, length-wise, it experiences large temperature differences (>≈10°C). Regions where the fingers meet the bus-bar are at lower temperatures (>≈10°C) compared to central and near edge regions. During firing, cooler regions are detrimental for contact formation for two reasons: (i) Since this part is supposed to carry carriers collected from the half length of the finger, carriers will observe resistance in

their path; (2) the contact resistance of finger in cooler regions will be enhanced. Contact formation directly affects V_{oc} as recombination velocity under the finger increases (e.g., dark current increases). The glass etches the underlying Si. The resulting sheet resistance change can increase contact resistance due to phosphorous consumption by the paste (see Chapter 3).

The high temperature step observed by the cell sinters the Ag particles in the presence of the glass frit. The non-uniform temperature distribution is not supposed to affect the current conduction of the finger in regions away from the bus bar. However, length-wise, it experiences large temperature differences (>10°C). The junction with the bus bar is at lower temperature then the rest of the length of the finger. Since most of the carriers collected by the finger have to pass through this region, they will invariably encounter resistance. Grid design envisions that every succeeding step in the current collection should have lower series resistance than the previous step. The non-uniform temperature distribution challenges the hierarchy. Figure 4.17b is a schematic showing clusters of Ag particles joined together, providing a lateral current flow path.

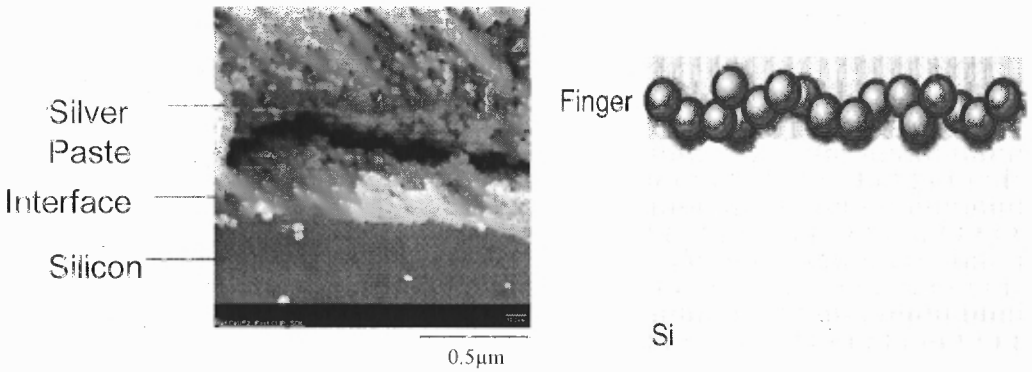

Figure 4.17 (a) The SEM of C/s of finger showing closely connected silver particles and (b) schematic showing clusters of Ag particles joined together, providing a lateral current flow path along the finger length.

As is well known, the bus-bar carries the charge carriers (e.g., electrons) collected by the fingers. The bus-bar region is about 10°C cooler than the center of the cell. At peak firing temperatures (800°C), the particles are coated with Ag-solvent metal alloy. Some of them may be sintered/fused creating lumps of agglomerated Ag particles. In some regions, there will be segregated lumps of glass also. As seen from Figure 4.17a, the silver particles are very closely spaced in optimally fired cell. The temperature is uniform within the bus bar region. The screen printed silver paste resistivity is in the range of ≈3 μΩ-cm (Hilali, 2005). This value is twice than the corresponding value if photolithography (i.e. 1.7 μΩ-cm) was used. Hence, the non-uniform temperature distribution will not affect the lateral current conduction of the bus bar.

4.6.2 Effect of Temperature Distribution on Alloy Growth below Bus-bar

Schubert, in 2006, etched the bus bar and showed distribution of crystallites (Figure 4.18). More crystallites were found at the edges below the busbar than at the center. In Figure 4.19, these are shown as the white regions. Schubert suggested that shrinking of the paste during firing created such features. However, a detailed explanation of such behavior was not given.

In this work, attempts were made to explain this behavior with respect to temperature distribution effect of the grid. Due to the shadow effect of the grid, as seen from the calculations (see Figure 4.13), central regions of solar cell have $\geq\approx$ 10°C higher temperature than the cell area under the bus bar. It has been shown in Chapter 3 that Ag-Si interaction is non-uniform (see Figure 3.4).

Below the bus-bar, due to temperature gradient, there will be more alloy growth at the edge than compared to the center of the bus-bar. Figure 4.19 schematically shows this behavior. Top area of the figure is a schematic, showing size distribution of the Ag rich region.

Figure 4.18 SEM image of area beneath the etched bus-bar.
Source: (Schubert, 2006)

Bigger regions are at the edges and small uniform Ag-rich regions are shown at the center. Bottom part of the schematic shows the relationship between temperature gradient and alloy size. To verify this hypothesis, mc-Si cell was etched in HF (3%) solution for 10-15 minutes and SEM images were taken from different regions of the cells.

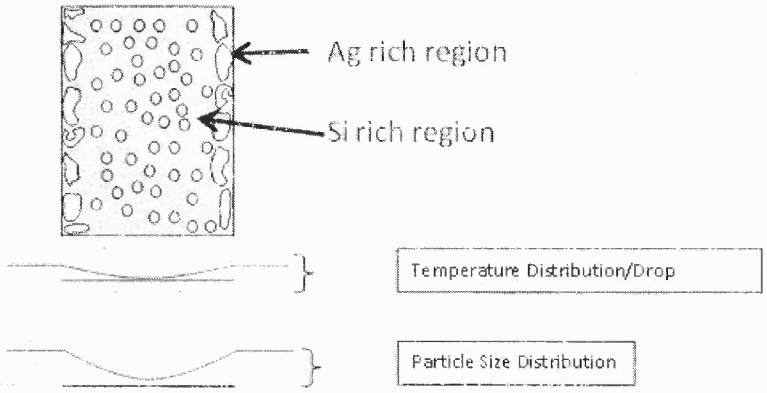

Figure 4.19 Schematic showing effects of temperature gradient on the Ag-Solvent metal-Si alloy distribution.

Figure 4.20a shows a close up of the region below one of the etched bus-bar. Discontinuous sintered agglomerated mass of Ag-Si-M alloy can be seen. Figure 4.20b is a large area SEM micrograph showing junction of two fingers with the bus-bar. In this Figure 4.20b, agglomerated mass of Ag-Si-M alloy is not seen at the edges. Similar SEM images of other areas of the cell also showed non-uniformity in the Ag-Si-M alloy formation at the edges. Further experiments are needed to confirm that the temperature distribution affects the Ag-Si-M alloy size distribution.

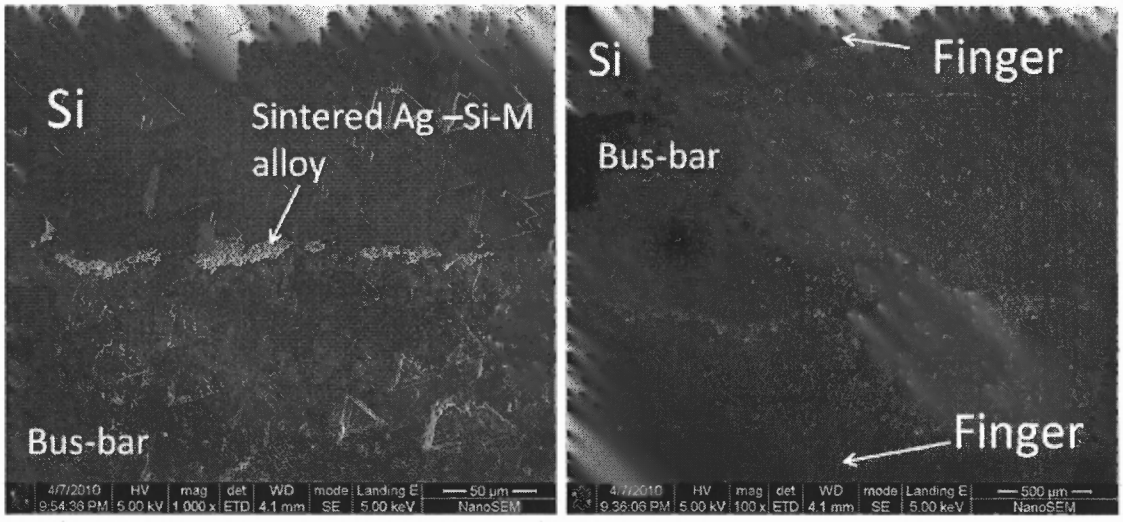

(a) (b)

Figure 4.20 SEM images below the etched bus-bar in mc-Si solar cells, (a) Sintered Ag-Si-M alloy can be seen below the bus-bar. (b) Large area SEM view, showing no size distribution of the Ag rich region.

CHAPTER 5

CURRENT-VOLTAGE (I-V) CHARACTERISTICS OF FIRED mc-Si CELLS

In Chapter 3, a study on the contact formation mechanisms of front contact was presented, and in Chapter 2, formation of back contact was discussed. Front contact requires fast, shallow (≈0.1μm) and continuous Ag-Si interaction below ≈800°C and good back contact requires higher than 800°C for thicker BSF. As discussed in Chapter 4, temperature distribution during firing step is non-uniform because of the shadow and mass effect of the metal grid. Temperature non-uniformity across the cell can further suffer unless edge losses due to radiation are compensated during co-firing.

Knowledge acquired through Chapters 2, 3 and 4 was used to create time-temperature firing profiles for mc-Si solar cells. The initial OPF furnace design with two zones was suitable for firing 4 inch wafers. Later, lamp assembly was modified to accommodate firing of 125mm (≈5 inch) cells. The latest version of the OPF is designed to process 156mm (≈6 inch) solar cells.

Initially, only the back aluminum contact firing was carried out. Firing profile was adjusted to achieve a V_{oc} of 620mV, approximately 10 micron thick BSF and flat back surface (Sopori et. al. 2009). Much of the work on back contact was done on solar cells that did not have a front contact. Hence, I-V characteristics of back contact studies have not been presented. The results were finally integrated into a complete cell fabrication process. I-V characteristics of fired cells were taken. The furnace expansion to accommodate 156 mm was also being carried out simultaneously. As will be discussed in Section 5.2, cells that were under fired were observed at the edges due to radiation heat loss. I-V characteristics were affected due to uneven cell heating. Cutting the cell from its

original size is not recommended but it was cut to show that the central part of the cell is fired well and it is the edges which are under fired (i.e., edge cooling) and affecting the important cell parameters (FF and V_{oc}). The cell was cut using dicing saw from the edges (0.4 inch from each edge) and I-V characteristics were again taken. I-V characteristics of devices of both sizes were then dissected using two diode equations (see equation 1.8). The light profiles were adjusted and another cell was fired. The process was repeated again. Both 125mm and 156mm cells were fired in the OPF.

5.1 Current Voltage (I-V) Characteristics-Basics

The current voltage (I-V) characteristics of a solar cell are the superposition of the I-V curves of the solar cell diode in the dark with the I_L. Increased power generation due to the illumination has the effect of shifting the I-V curve down into the fourth quadrant where power can be extracted from the diode. I-V measurement technique is a commonly used tool to determine various important parameters (i.e., J_{sc}, V_{oc}, FF, η) of solar cells. Figure (5.1) shows the schematic of a typical set-up used for measuring I-V characteristics of solar cells. A height adjustable, calibrated xenon light source (Air Mass 1.5 spectrum, with intensity of $1000W/m^2$) is used to illuminate the cell. The cell is placed on water cooled, nickel coated oxygen free copper stage. A close looped temperature controller system assisted by Peltier devices (i.e. placed between stage and water jacket) and Resistance Temperature Detector (RTD) (i.e., placed inside the stage) maintains stage/cell temperature at $\approx 25.4°C$. Carefully designed, series of current and voltage probes are placed on top of the cell in such a way so that probes create minimum shadow on the cell. The number of current collecting probe increases as cell area increases. A voltage probe is also placed below the cell and the entire back side acts as a

current collection probe. Both current and voltage channels are kept different to minimize series resistance losses. The light intensity is fixed by first measuring current of a calibrated cell and then using the test cell.

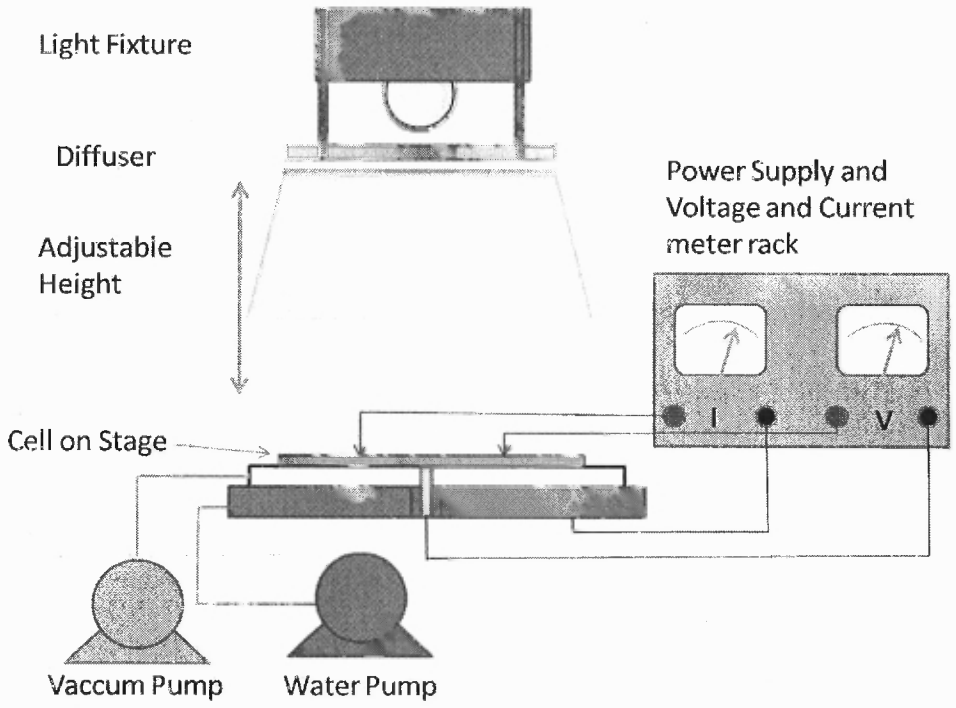

Figure 5.1 Schematic of a Set up of a typical solar simulator.

Illuminated I-V characteristics yield the values of V_{oc}, FF, and J_{sc}. Dark I-V Characteristics are useful in determining series resistance (R_s), shunt resistance (R_{sh}) and saturation current density in bulk and emitter (J_{01}) and in the depletion region (J_{02}). They are usually calculated by dissecting logarithmic dark curves using a two diode model (King, Hansen, Kratochvil, & Quintana, 1997). The solar cell is measured in the dark by applying a bias voltage from 0 to 0.620 V, and the current J_d is measured as a function of the applied voltage (Figure 5.2). The experimental data is fitted to equation (5.1) below using the least-squares method (Kleinbaum, Kupper, Muller, & Nizam, 1998, Hilali,

2005) and five pertinent variables: the saturation current density (J_{o1}), the junction leakage current (J_{o2}), the shunt resistance (R_{sh}), the series resistance (R_s), and the second-diode ideality factor n_2.

$$J_d = J_B + J_j + J_{sh} = J_{o1}\left[\exp\left(\frac{q(V+JR_S)}{n_1 kT}\right)-1\right]+J_{o2}\left[\exp\left(\frac{q(V+JR_S)}{n_2 kT}\right)-1\right]+\frac{(V+JR_S)}{R_{sh}} \tag{5.1}$$

The first-diode ideality factor n_1 for bulk recombination is always set to one. For low bias, the shunt resistance effect dominates the dark I-V curve. At voltages below the maximum power point, the junction leakage current (second diode) starts to influence the dark I-V curve, and at slightly higher voltages the bulk saturation current strongly affects the dark I-V curve. At higher voltages, the series resistance strongly affects the dark I-V curve.

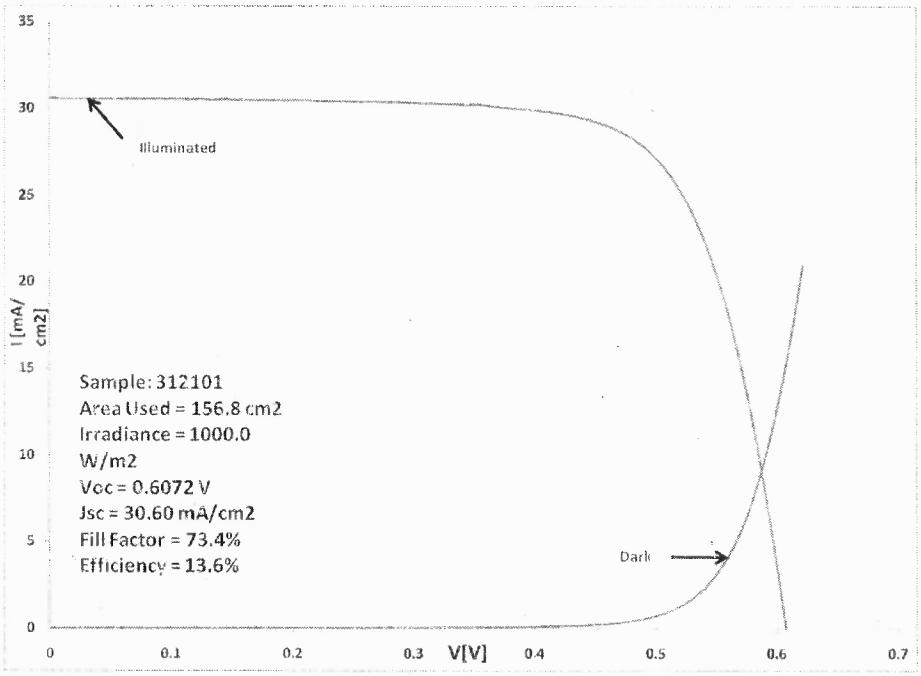

Figure 5.2 Illuminated and Dark I-V characteristics of screen printed mc-Si cell.

5.2 Influence of Edge Effect on I-V Characteristics of mc-Si Cell

Figure 5.3 shows the photograph of a fired cell (125mm) with temperature non-uniformity. In the current study, regions that were alloyed are called grey regions and regions that were cooler (≈15°C) and un-alloyed during firing are called white regions. On the edges and corners of the certain cells, white regions can be observed. In the white regions, the screen printed aluminum paste is flaky and can be removed by simply touching. The occurrence of white regions in the edges and corners of the cell can be avoided by using better temperature profile. These white regions occur due to non laminar gas flow above the cell, higher exhaust, poor lamp assembly design and placement, lamp burnout and poor muffle design.

The current furnace has been modified to solve some of the above mentioned problems (e.g., improved lamp design and power control, lamp burnout feedback loop, rotary van pump with exhaust control valve). Work is in progress to solve the remaining issues (e.g., muffle design, better light trapping).

The FF is affected by the (R_s) and shunt resistance (R_{sh}). For higher FF (>80%), the series resistance has to be minimum (<0.5mΩ) and shunt resistance has to be maximum (>8kΩ). From Figure 5.3, it can be seen that the V_{oc} of the white regions will be poor. Hence, the dark current increases. The cell V_{oc} will be decreased by these white regions.

Figure 5.4 shows various I-V profiles of solar cells fired at different light intensities as controlled by signal voltages applied to various segments of the light source. It shows the approach taken to optimize the solar cell firing. The ratio of the light intensity signal to lamp power controller is adjusted after temperature distribution

profiles of the cell are determined (See Chapter 4). Ref 1(156mm) and Ref 2 (125mm) are vendor supplied reference cells. The LI values indicated are the peak signal voltages applied during cell firing. The LI values are adjusted to have highest possible FF.

Figure 5.3 Photograph of back side of fired 125mm solar cell. On the bottom edge of the photograph, temperature non-uniformity can be seen at both corners.

From Figure 5.4, it can be seen that with LI of 6.8, the cell suffers from poor fill factor. The cell has high series resistance as J_{sc} is much lower (31mA/cm^2). LI of 7.2 improves the cell I-V profile but still the series resistance is higher and hence fill factor is poor (FF=0.68). Above LI of 7.3, the cell FF starts to degrade. Higher value of LI (>7.4) corresponds to temperature above 800°C. At high temperatures, the cell develops lower shunt manifested by a lower V_{oc}.

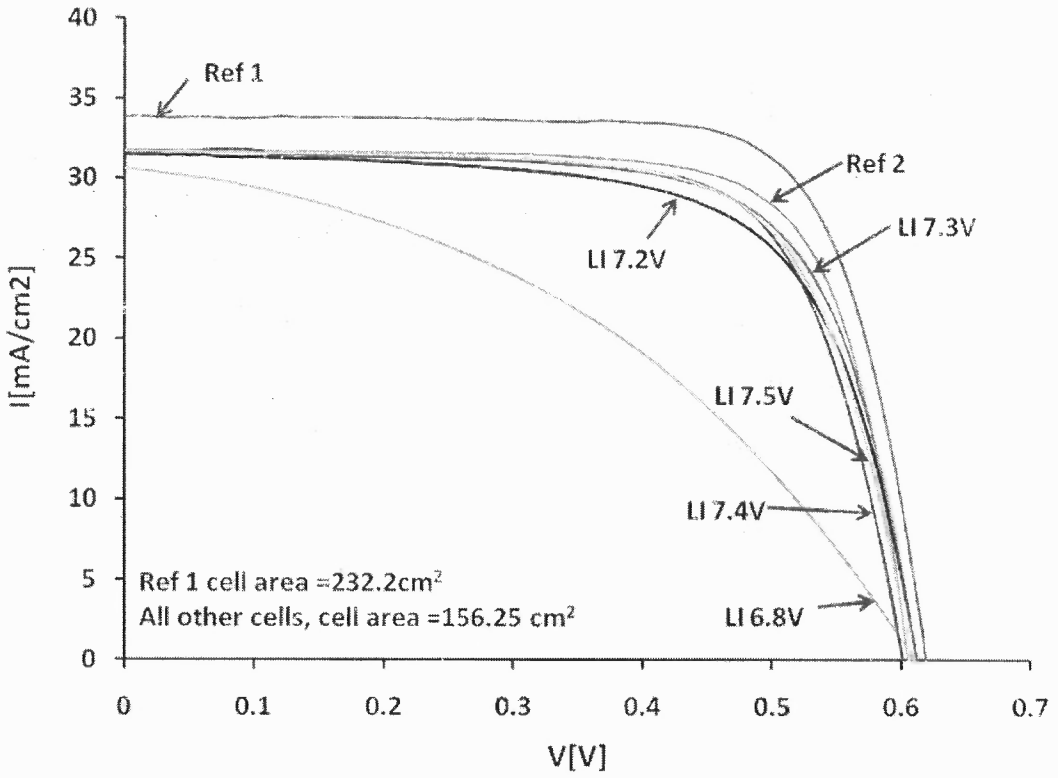

Figure 5.4 I-V Characteristics of mc-Si cells fired at various light intensities. Ref 1 is 156mm cell. Ref 2 and other cells are 125mm. LI= Light Intensity.

Tables 5.1 and 5.2 give I-V characteristics of full size and reduced size cells measured at 25.4°C. Cell (a) with original area of 156.8 cm^2 had a V_{oc} of 601.2 mV. The FF was 73.5%; efficiency was 13.6%. When the cell was cut to a smaller size (108.2cm^2), the re-measured V_{oc} increased to 603mV and FF was increased to 75.7% (see table 5.2). The efficiency of the cut cell increased to 14.1%. The edges of the cell were found to be under fired compared to the center. This can be seen with increased shunt resistance (R_{sh} =18.143kΩ) after a reduction in the size. The series resistance has marginally increased from 4.7 to 6.7 mΩ.

FF of cell (b) increased from 70.6% to 73.9%. However, the current did not increase due to increased series resistance. The increased V_{oc} values indicate that the contact formation (junction strength) and front and back surface passivation are

reasonably good. FF of cell (c) increased from 73.4% to 74.1%. Again, the cell was under fired at the edges. This can be seen because the shunt resistance increased and the series resistance increased only marginally. Cell (d) showed largest increase in the fill factor. However, non-uniform alloying (e.g., non-uniform temperature distribution) at the back contact prevented the V_{oc} from achieving a higher value.

Table 5.1 I-V Parameters at 25.4 ^{0}C (Area: 156.8cm^2) (Full size)

Cell ID.	V_{oc} (V)	J_{sc} (mA/cm^2)	FF (%)	η (%)	R_s (mΩ)	R_{sh} (kΩ)	I_{01} (mA/cm^2)	I_{02} (mA/cm^2)
a	0.601	30.76	73.5	13.6	4.765	5.581	1.54E-09	2.71E-05
b	0.608	30.87	70.6	13.3	8.330	13.432	1.27E-09	2.57E-05
c	0.607	30.60	73.4	13.6	5.812	13.977	1.2E-09	2.11E-05
d	0.603	30.63	65.4	12.1	8.152	19.515	1.2E-09	2.01E-05

Table 5.2 I-V Parameters at 25.4 ^{0}C (Area: 108-109 cm^2) (Reduced size)

Cell ID.	V_{oc} (V)	J_{sc} (mA/cm^2)	FF (%)	η (%)	R_s (mΩ)	R_{sh} (kΩ)	I_{01} (mA/cm^2)	I_{02} (mA/cm^2)
a	0.603	30.96	75.7	14.1	6.798	18.143	1.64E-09	2.14E-05
b	0.614	30.99	73.9	14.1	11.608	17.283	1.02E-09	1.65E-05
c	0.609	30.88	74.1	14.1	6.621	24.441	9.64E-09	3.29E-05
d	0.605	30.88	74.1	14.1	11.378	40.420	9.54E-09	3.2E-05

Figure 5.5 shows the comparison of I-V characteristics of cut and original cell size. Here overall increase in the cell performance can be observed. Figure 5.6 shows that the lab fired cells show higher V_{oc}, J_{sc} and η compared to vendor supplied cells. However, further work is required to improve the fill factor of the laboratory fired cell.

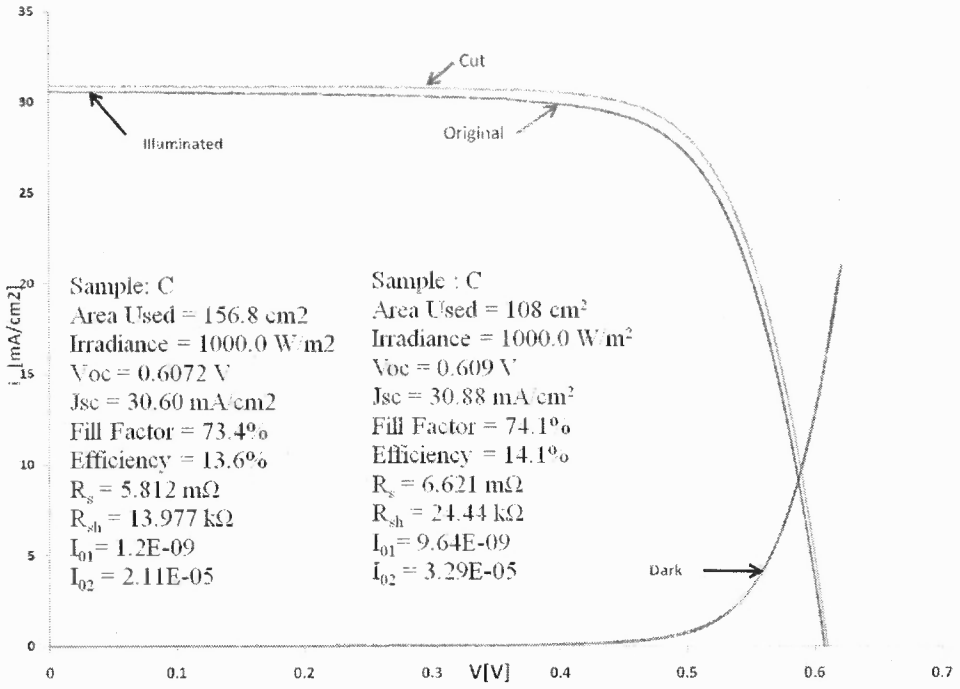

Figure 5.5 I-V characteristics of original and cut mc-Si solar cell.

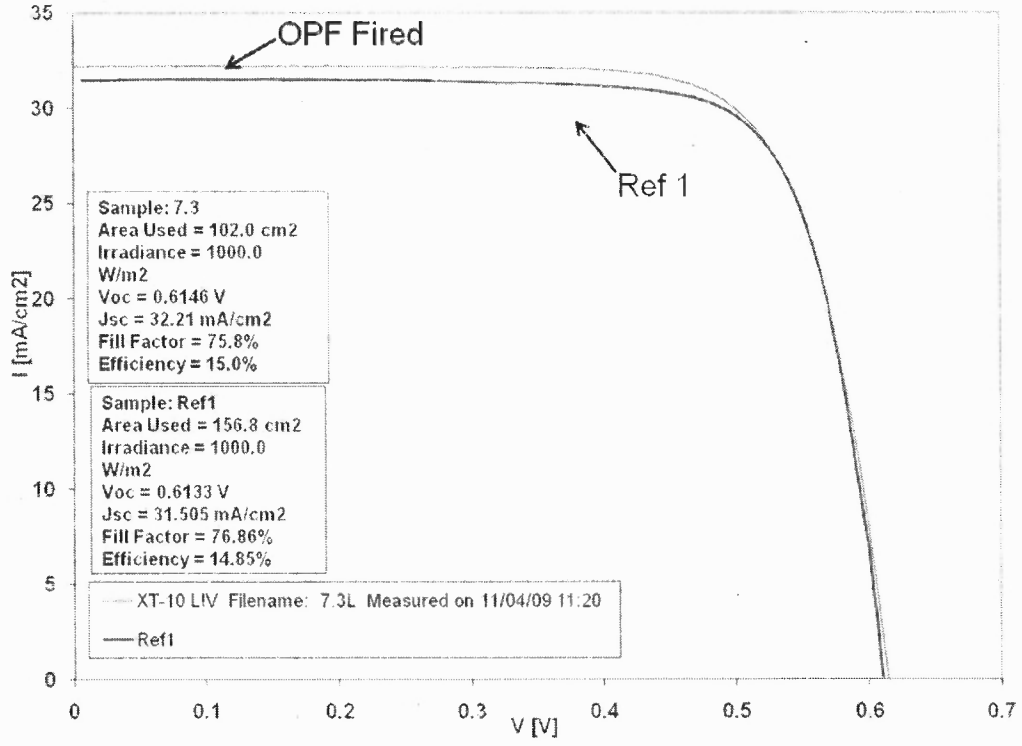

Figure 5.6 Comparison of lab fired cells and vendor supplied mc-Si cell.

Figure 5.7 below shows the I-V Characteristics of a 156 mm (243.4cm^2) cell. The firing profiles determined during firing of 125 mm (156.8cm^2) cell were slightly modified and applied to fire the cell. The cell improvement in FF and V_{oc} can be seen when compared to full size 125 mm cells. High shunt resistance (R_{sh}) can be noted. Further work is being carried out to match the efficiency and fill factor values of vendor supplied reference cells.

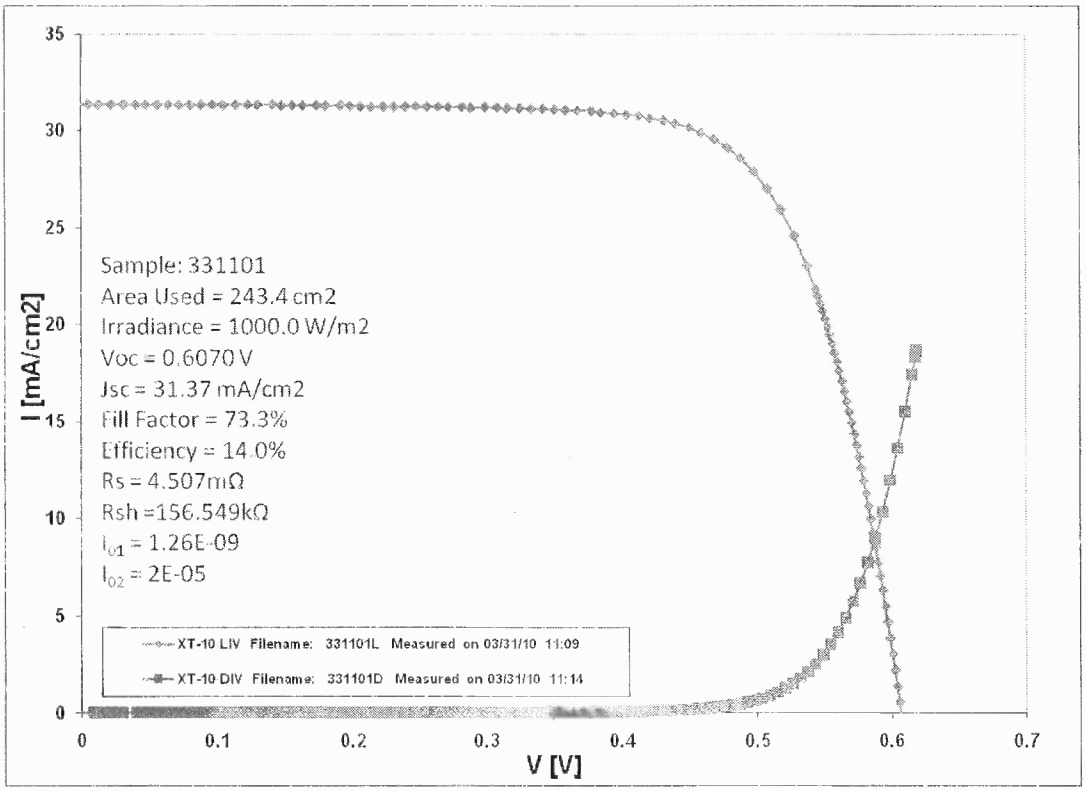

Figure 5.7 I-V characteristics of 156 mm solar cell.

CHAPTER 6

CONCLUSIONS AND FUTURE WORK

6.1 Conclusions

A rapid and high volume fire through process for contact metallization of mc-Si solar cells has been discussed. Screen printing as well as new promising techniques were reviewed. Complexity of screen printed front contact formation was elaborated. Various hypotheses for front contact formation were reviewed.

An improved technique based on CMP to cross-section large lengths of wafers/solar cells at any step of the solar cell fabrication was presented. This method produces large solar cell samples which can be used in performing a variety of AFM, CFM, SKPM, EDX and other scanning analyses. The large flat cross section is very valuable for optical examination of various regions such as metal fingers, BSF, and metal penetration into the front contact for statistically meaningful analyses of the metal semiconductor interface. Further work needs to be carried out to make this technique repeatable.

Temperature distribution of wafers with different surface characteristics (polished, textured, SiN:H coated) and conventional mc-Si solar cell were recorded. Single or multiples thermocouples were attached to the cells/wafers and fired in OPF. The data obtained were used to generate firing profiles that created uniform temperature distribution (±5°C) on wafer/cell. On large area cells, temperature uniformity is an important parameter for low resistance (<0.3mΩ) contact formation.

Time-temperature profiles generated also indicated that, in the presence of glass, the Si-Ag interaction occurs at significantly lower temperatures than previously thought. This result can lead to more accurate control of the cell firing profile. Experimentally, a temperature difference of 25 °C was measured in the region below the bus bar and away from the bus bar. More experiments must be performed to further confirm this behavior. SIMS study on etched cells showed that a significant consumption of phosphorous occurs during Si-Ag interaction. This effect can also reduce V_{oc}. C-AFM study identified glass as a non-conducting phase. SKPM profiles were studied to measure the surface potential of the metal semiconductor region. SEM images of C/s samples showed that glass does not significantly dissolve silver. Glass coated Ag particles can be clearly seen to have >80% of the contact structure in optimally fired cells.

Ag-Si, Ag-glass, glass-Si and Ag-glass-Si reactions were discussed. Typically, the maximum temperature reached under the metal is less than 800°C; this is much lower than the eutectic point of Ag-Si (≈835°C). Solvent metals such as Pb, Bi, Sn reduce the melting point of the surface of Ag particles through ion exchange between glass and Ag particles. Alloy coated particles interact with Si and create Si-Ag alloy. Due to the presence of glass and dissolved SiN:H, the area for Ag-Si interaction is reduced by about 30%.

Ag-glass-Si interactions lead to the formation of Ag-rich and Si-rich areas. The amount of each area depends strongly on the contact-formation mechanism. Because Ag-rich area forms an ohmic contact at the Si interface, it is desirable to have a large fraction of a Ag-rich area to have a high fill factor of the cell. During optical characterization (i.e. EDX studies) of c/s samples, no Ag crystallites were observed. The non-uniformity of the

Ag-Si interaction may lead to degradation of various electrical parameters (i.e. FF and V_{oc}). Based on present study, a hypothesis invoking ion exchange phenomena for front contact formation was presented.

To study the effect of metal grid on temperature uniformity, thermal modeling of the cell at peak firing temperature (≈800°C) was carried out. A temperature gradient of more than 10°C across cell width was calculated using thermal simulation. Shadow effect of the bus-bar (≈2mm wide), results in lower temperature underneath it than the rest of the cell. Gradients (10°C) in temperature were calculated in areas around bus bar (e.g. 1cm on each side). Since it is a grid shadowing effect, cells prepared either by screen printed or evaporated contacts will have temperature distribution across their entire width. Hence, cells with all contacts on the back side will have advantage over front gridded cells. Experimentally, the Si-Ag interaction below the bus-bar was not found to be affected by temperature distribution during firing.

For optimal control of the co-firing process, better understanding of back contact is also necessary. Hence, a study on back Al contact formation was also conducted. Some results were presented. Importance of BSF in cells having longer diffusion lengths (> cell thickness) was stressed. Si diffusion was attributed to several defects (e.g. bumps, holes, shunts). Higher firing temperatures (>800°C) are required to produce thicker BSF. This requirement is opposite to that of front contact where glass frit is added to lower the Si-Ag eutectic temperature. Due to the presence of glass, Al alloyed regions are not uniform laterally, but can produce wide (≈10μm thick) BSF regions.

Firing profiles were adjusted to incorporate the knowledge gained by the contact formation study. Cells were fired in an optical processing furnace. I-V characteristics were measured. Results were presented. A V_{oc} of 615 mV with cell efficiency of 15% mc–Si was measured. Further studies are being carried out to improve the V_{oc} to 620mV.

6.2 Future Work

The following is a list of additional work that will help to develop a better understanding of the front contact formation in screen printed fire-through contact metallization:

1. The screen printing technology has to be modified to allow for higher aspect ratio for fingers and bus-bar and improve the finger width resolution
2. Alternative techniques to screen printing such as inkjet printing and hot melt paste should be further investigated.
3. Numerical analyses and development of experimental procedures can help to prove hypotheses of the ion exchange based front contact formation model.
4. There are a number of incremental improvements that could be made to the implementation of the thermal modeling (COMSOL Multiphysics) of the effect of grids on solar cells during co-firing. In particular, the following is a list of features that would improve the accuracy of the calculations:

    a. Include the convection effect (i.e. carrier gases inside the furnace) on solar cells along with the radiation heat flux.

    b. Incorporate change of heat balance due to the endothermic alloying of Si and Al during heating.

    c. Implement change in temperature distribution due to use of multiple cemented thermocouples.

    d. Include effects on temperature distribution due to change in reflection and texturing of Si surface due to Al-Si alloying.

    e. Incorporate the effect of change in emissivity of front contact grid on temperature variation of cell during co-firing.

f. Measurement and use of reasonable accurate values of optical and physical properties (i.e., emissivity, thermal conductivity) of metal pastes will help to improve the thermal model.

5. Implementation of a better technique to measure repeatable and accurate contact resistance of the screen printed front contact can help to optimize firing profile.
6. Numerical methods such as descretized modeling and finite element method (continuous) can be explored to describe resistive electrical losses in front contact and help to create an integrated model.

REFERENCES

Alamo, J. B., Eguren, J., & Luque, A. (1981). Operating limits of Al-alloyed high-low junctions for BSF solar cells. *Solid-State Electronics, 24*, 415, 415-419. doi:10.1016/0038-1101(81)90038-1.

Amick, J. A., Bottari, F.J., & Hanoka, J. I. (1994). The effect of aluminum thickness on solar cell performance. *Journal of Electrochemical Society, 141*(6), 1577-1585. Retrieved from http://dx.doi.org/10.1149/1.2054965.

Appel, J. S., Sopori, B., Rupnowski, P., Duda, A., Roybal, L., Mehta, V., & Ravindra, N. M. (2008). Characterization of solar cell substrates using diode array technique. Paper presented at the *137th Annual TMS Meeting and Exhibition, New Orleans*, LA.

Ballif, C., Huljic, D. M., Willeke, G., & Wyser, A. (2003). Silver thick-film contacts on highly doped n-type silicon emitters: structural and electronic properties of the interface. *Applied Physics Letters 82*, 1878-80. doi:10.1063/1.1562338.

Basore, P. A. (1993). Extended spectral analysis of internal quantum efficiency. Proceedings of the *23rd IEEE Photovoltaic Specialists Conference*, 147-152. doi:10.1109/PVSC.1993.347063.

Cheek, G., Mertens, R., Overstraeten, R., & Frisson, F. (1984). Thick-film metallization for solar cell applications. *IEEE Transactions on Electron Devices, 31*(5), 602-609.

Chung, Y., & Kim, H.G. (1988). Effect of oxide glass on the sintering behavior and electrical properties in Ag thick films. *IEEE Transactions on Components, Hybrids, and Manufacturing Technology*, *11*, 195-199. doi: 10.1109/33.2987.

COMSOL AB, computer code COMSOL Multiphysics version 3.5 (COMSOL AB, Burlington, MA, 2009).

Conductive AFM Option (C-AFM). (2010). Retrieved on March 30, 2010.from http://www.veeco.com/conductive-afm-option-mode-cafm/index.aspx.

Cudzinovic, M., & Sopori, B. (1996). Control of back surface reflection from aluminum alloyed contacts on silicon solar cells. Proceedings of the *25 th IEEE Photovoltaic Specialists Conference*, 501-503.doi: 10.1109/PVSC.1996.564053.

Cuevas, A. & Russell, D. A. (2000). Co-optimization of the emitter region and the etal grid of silicon solar cells. *Progress in Photovoltaic: Research and Applications*, *8*(6), 603-616. doi: 10.1002/1099-159X(200011/12)8:6<603::AID-PIP333>3.0.CO;2-M.

Doshi, P., Mejia, J., Tate, K., & Rohatgi, A. (1997). Modeling and characterization of high-efficiency silicon solar cells fabricated by rapid thermal processing, screen printing, and Plasma-Enhanced Chemical Vapor Deposition. *IEEE Transactions on Electron Devices, 44*(9), 1417-1424. doi: 10.1109/16.622596.

Erath, D., Filipovic,´A. , Retzlaff, M., Goetz, A. K., Clement F, Biro, D., & Preu, R., (2010). Advanced screen printing technique for high definition front side metallization of crystalline silicon solar cells. *Solar Energy Materials & Solar Cells, 94,* 57-61. doi:10.1016/j.solmat.2009.05.018.

Glunz, S. W., Knobloch, J., Biro, D., & Wettling, W. (1997). Optimized high efficiency silicon solar cells with J_{sc}=42 mA/cm^2 and η=23.3 %. Proceedings of the *14th European Photovoltaic Solar Energy Conference,* 392-395.

Glunz, S. W., Mette, A., Aleman, M., Richter, P. L., Filipovic,A., & Willeke, G.(2006). New concepts for the front side metallization of silicon solar cells. Proceedings of the *21st European Photovoltaic Solar Energy Conference.*746-749.

Goetzberger, A., Knobloch, J., & Bernhard., V. (1998). *Crystalline silicon solar cells.* John Wiley & Sons.

Green, M. A. (1992). *Solar cells: operating principles. Technology and system applications.* The University of New South Wales: Kensington, N.S.W.

Green, M. A. (1993). Silicon solar cells: evolution, high efficiency design and efficiency enhancements. *Semiconductor Science Technology, 8*(1), 1-12. doi: 10.1088/0268-1242/8/1/001.

Gzowski, O., Murawski, L., & Trzebiatowski, K. (1982). The surface conductivity of lead glass. *Journal of Physics D: Applied Physics, 15,* 1097-1101. doi:10.1088/0022-3727/15/6/019.

Hilali, M. M. (2005). Understanding and development of manufacturable screen printed contacts on high sheet-resistance emitters for low-cost silicon solar cells (Doctoral Dissertation, Georgia Institute of Technology). Retrieved from http://hdl.handle.net/1853/7284.

Hilali, M. M., Sridharan, S., Khadilkar, C., Shaikh, A., Rohatgi, A., & Kim, S. (2006). Effect of glass frit chemistry on the physical and electrical properties of thick-film Ag contacts for silicon solar cells. *Journal of Electronic Materials, 35* (11), 2041-2047.

Hilali, M.M., Rohatgi, A., & To, B. (2004). A review and understanding of screen-printed contacts and selective–emitter formation. Proceedings of *16th Workshop on Crystalline Silicon Solar Cells & Modules: Materials and Processes.* Ed. by B. Sopori et al, (109-116).

Hong, K. K., BinCho, S., You, J., WeonJeong, J., MookBea, S., & YoulHuh, J. (2009). Mechanism for the formation of Ag crystallites in the Ag thick-film contacts of crystalline Si solar cells. *Solar Energy Materials & Solar Cells, 93*, 898-904. doi:10.1016/j.solmat.2008.10.021.

Huljic, D. (2006,October 8). Structured method for applying a thermoplastic paste on a substrate and its use. Retrieved April 8, 2010 from, http://www.patent-de.com/20060810/DE102004056492B3.html.

Huster, F. & Schubert, G. (2005). ECV doping profile measurements of aluminium alloyed back surface fields. Proceedings of 20th European Photovoltaic Solar Energy Conference, 1466-1469.

Huster, F., Gerhards, C., Spiegel, M., Fath, P., & Bucher, E. (2000). Roller printed multi crystalline silicon solar cells with 16% efficiency and 25 μm finger width. Proceedings of *27th IEEE Photovoltaic Specialists Conference*, 205-208. doi: 10.1109/PVSC.2000.915790.

Ibos, L., Marchetti, M., Boudenne, A., Datcu, S., Candau,Y., & Livet,J. (2006). Infrared emissivity measurement device: Principle and applications. *Measurement Science and Technology, 17*, 2950-2956. doi: 10.1088/0957-0233/17/11/013.

Iles, P. A. (2001). Evolution of space solar cells. *Solar Energy Materials & Solar Cells, 68,* 1-13. doi:10.1016/S0927-0248(00)00341-X.

Incropera, F., & DeWitt, D. P. (2001). *Fundamentals of heat and mass transfer.* John Wiley & Sons.

Jeon, S., Koo, S., & Hwang, S. (2009). Optimization of lead-and cadmium-free front contact silver paste formulation to achieve high fill factors for industrial screen-printed Si solar cells. *Solar Energy Materials & Solar Cells, 93* 1103-1109. doi:10.1016/j.solmat.2009.01.003.

Kaminski, A., Vandelle, B., Fave, A., Boyeaux, J. P., Nam, L. Q., Monna, R., Sarti, D., and Laugier, A. (2002). Aluminium BSF in silicon solar cells. *Solar Energy Materials & Solar Cells 72*, 373-379. doi:10.1016/S0927-0248(01)00185-4.

Kattner, U. (2003). Ag-Bi-Pb System. Retrieved April 8, 2010 from http://www.metallurgy.nist.gov/phase/solder/agbipb.html

Khadilkar, C., Kim, S., Shaikh, A., Sridharan, S., & Pham, T. (2005). Characterization of Al back contact in a silicon solar cell. Tech. Digest. of International PVSEC-15. Retrieved April 15, 2010 from, http://www.ferro.com/non-cms/ems/solar/technical/Paper-1.pdf.

Khadilkar, C., Sridharan, S., Gnizak, D., Pham, T., Kim, S., & Shaikh, A. (2005). Effect of glass chemistry and silicon orientation on the front contact microstructure formation in a silicon solar cell. Proceedings of *20th European Photovoltaic Solar Energy Conference*, 1291-1296.

Kim, K., Dhungel, K. S., Gangopadhyay, U., Yoo, J., Seok, C. W., & Yi, J. (2006). A novel approach for co-firing optimization in RTP for the fabrication of large area mc-Si solar cell. *Thin Solid Films, 511-512,* 228-234. doi:10.1016/j.tsf.2005.12.131.

King, B. H., O'Reilly, M. J., & Barnes, S. M. (2009). Characterizing aerosol jet® multi-nozzle process parameters for non-contact front side metallization of silicon solar cells.1107-1111.

King, D.L., Hansen, R., Kratochvil, J.A., & Quintana, M. A. (1997). Dark current-voltage measurements on photovoltaic modules as a diagnostic or manufacturing tool. Proceedings of the *26th IEEE Photovoltaic Specialists Conference*, 1125-1128. doi: 10.1109/PVSC.1997.654286.

Kleinbaum, D.G., Kupper, L. L., Muller, K.E. and Nizam, A. (1998). *Analysis and other multivariable methods.* 3rd. ed., Duxbury Press.

Kontermann, K., Horteis, M., Kasemann, M, Grohe, A., Preu, R., Pink, E. & Trupke, T. (2009). Physical understanding of the behavior of silver thick-film contacts on n-type silicon under annealing conditions. *Solar Energy Materials & Solar Cells, 93*, 1630-1635. doi:10.1016/j.solmat.2009.04.019.

Licari, J.J.; Enlow, L.R. (1998). *Hybrid microcircuit technology handbook.* William Andrew Publishing/Noyes, 2nd edition.

Lin, C. H., Tsai, S.Y., Hsu, S. P., & Hsieh, M.H. (2008). Structural properties of the solidified–Al/regrown-Si structures of printed Al contacts on crystalline si solar cells. *Solar Energy Materials & Solar Cells 92*, 986-991. doi:10.1016/j.solmat.2008.02.031.

Lin, C., Tsai, S., Hsu, S., & Hsieh, M. (2008). Investigation of Ag-bulk/glassy-phase/Si heterostructures of printed Ag contacts on crystalline Si solar cells. *Solar Energy Materials & Solar Cells, 92*, 1011-1015. doi:10.1016/j.solmat.2008.02.032.

Lin, J. C., & Wang, C. Y. (1996). Effect of surface properties of silver powder on the sintering of its thick-film conductor. *Materials Chemistry and Physics 45*(3), 253-261. doi: 10.1016/0254-0584(96)80116-7.

Lindmayer, J., & Allison, J. (1973). The violet cell: an improved silicon solar cell. *COMSAT Tech. Rev. 3*(1), 1-23.

Luque, A., & Hegedus, S. (Eds.) (2003). *Handbook of photovoltaic science and engineering.* John Wiley & Sons.

Mandelkorn, J., & Lamneck, J. H. (1973). A new electric field effect in silicon solar cells *Journal of Applied Physics, 44,* 4785.

Massalski, T. B. (1992). *Binary alloy phase diagrams.* ASM International.

McCaldin, J.O., & Sankur, H. (1971). Diffusivity and Solubility of Si in the Al Metallization of Integrated Circuits," *Applied Physics Letters, 19*(12), 524-527.

Mehta, V., & Sopori, B. (2009, December). Screen printed Al back contacts on si solar cells: issues and some solutions. Paper presented at the *2009 MRS Fall Meeting*, Boston, MA.

Mehta, V., Sopori, B. L., Rupnowski, P., Reedy, R., Appel, J., Domine, D., & Ravindra N. M. Formation of Ag-Si contact in fire-through metallization for solar cells: Experimental studies. *To Be Published in Journal of Materials Science.*

Mehta, V., Sopori, B., & Ravindra, N. M. (2008, March). Mechanisms of front contact formation in Si solar cell. Paper presented at the *137th Annual TMS Meeting and Exhibition*, New Orleans, LA.

Mehta, V., Sopori, B., Rupnowski, P., Appel, J., Domine, D., Moutinho, H., To, B., Shaikh, A., Merchant, N., Carlson, D., & Ravindra, N. M. (2007, March). Formation of Ag-Si contact in fire-through metallization for solar cells: Experimental studies. Paper presented at *136th Annual TMS Meeting and Exhibition*, Orlando, FA.

Mehta,V., Sopori, B., Guhabiswas, D., Reedy, R., Moutinho, H., To, B., Liu, F., Shaikh, A., Young, J., & Rangappan, A. (2009, August). A new approach to overcome some limitations of back Al contact formation of screen printed silicon solar cells. Paper presented at the *19th Workshop on Crystalline Silicon Solar Cells & Modules: Materials and Processes*, Vail, CO.

Mette, A. (2007). New concepts for front side metallization of industrial silicon solar cells (Doctoral Dissertation). Retrieved March 3, 2009 from, http://publica.fraunhofer.de.

Nakajima, T., Kawakami, A., & Tada, A. (1983). Ohmic contact of conductive silver paste to silicon solar cells. *International Journal for Hybrid Microelectronics, 6,* 580-586.

Narasimha, S., Rohatgi, A, & Weeber, A.W. (1999). An optimized rapid aluminum back surface field technique for silicon solar cells. *IEEE Transactions on Electron Devices 46*(7), 1363-1369.

Neuhaus, D. H., & Munzer A. (2007). Industrial silicon wafer solar cells. *Advances in OptoElectronics*, 1-15. doi:10.1155/2007/24521.

Nonnenmacher, M., O'Boyle, M. P. & Wickramasinghe H. K. (1991).Kelvin probe force microscopy. *Applied Physics Letters, 58*, 2921-2923. doi:10.1063/1.105227.

Oba.,T & Inaba, A. (1995). Sintering behavior of silver with various glass frits. Electronic Manufacturing Technology Symposium, 1995, Proceedings of *1995 Japan International, 18th IEEE/CPMT International*, 179-182. doi: 10.1109/IEMT.1995.541022.

Olesinski, R., Gokhale, A., & Abbaschian, G. (1989). The Ag-Si (silver-silicon) system. *Bulletin of Alloy Phase Diagram, 10*(6), 635-640.

Plekhanov, P. S., Negoita, M.D., & Tan, T.Y. (2001). Effect of Al-induced gettering and back surface field on the efficiency of Si solar cells. *Journal of Applied Physics, 90* (10), 5388-5394. doi:10.1063/1.1412575.

Porter, L. M., Teichera, A., & Meier., D. L. (2002). Phosphorus-doped, silver-based pastes for self-doping ohmic contacts for crystalline silicon solar cells. *Solar Energy Materials & Solar Cells, 73*, 209-219.

Prudenziati, M. (Ed.) (1994). *Thick Film Sensors*. Elsevier.

Prudenziati, M., Moro, L., Morten, B, Sirotti, F., & Sardi, L. (1989). Ag based thick film metallization of silicon solar cells. *Active and Passive Elec. Comp. 13,*133-150.

Ralph, E. L. (1976). Recent advancements in low cost solar cell processing. Proceedings of the *11th IEEE Photovoltaic Specialists Conference*, 315-316.

Rane, S. B., Seth, T., Phatak, G., Amalnerkar, D., & Ghatpande, M. (2004). Effect of inorganic binders on the properties of silver thick films. *Journal of Materials Science: Materials in Electronics, 15*(2), 103-106. doi:10.1023/B:JMSE.0000005385.21127.ac.

Ravindra, N. M., Ravindra, K., Mahendra, S., Sopori, B., & Fiory, A. T. (2003). Modeling and simulation of emissivity of silicon-related materials and structures. *Journal of Electronic Materials, 32*(10), 1052-1058.

Rollert, F., Stolwijk, N. A., & Mehrer, H. (1987). Solubility, diffusion and thermodynamic properties of silver in silicon. *Journal of Physics. D: Applied Physics, 20*, 1148-1155.

Romijn, I. G., Rieffe, H., Weeber, A., & Soppe W. (2005). Passivating mc-Si solar cells using SiNx:H: How to tune to maximum efficiencies. Proceedings of *15th International Photovoltaic Science and Engineering Conference*, 303-304.

Schema MEB (en).svg. In Wikipedia. Retrieved April 6, 2010, from http://en.wikipedia.org/wiki/File:Schema_MEB_(en).svg.

Schematic depiction of SIMS source region. (2010). Retrieved March 20, 2010 from http://serc.carleton.edu/details/images/8453.html.

Schroder, D. K. (2006). *Semiconductor material and device characterization.* Wiley-IEEE Press, 3 edition.

Schroder, D. K., & Meier, D. E. (1984). Contact resistance: Its measurement and relative importance to power loss in a solar cell. *IEEE Transactions on Electron Devices*, *31*(5), 647-653.

Schroder, D. K., & Meier, D. E. (1984). Solar cell contact resistance -A review. *IEEE Transactions on Electron Devices*, *31*(5), 637-647.

Schubert, G. (2006). Thick film metallization of crystalline silicon solar cells: Mechanisms, models and applications (Doctoral Dissertation, University of Konstanz). Retrieved December 10, 2008 from, http://www.ub.uni-konstanz.de/kops/volltexte/2007/2559.

Schubert, G., Fischer, & Fath P. (2002). Formation and nature of Ag thick film front contacts on crystalline silicon solar cells. Proceedings of *17th European Photovoltaic Solar Energy Conference*, 343-346.

Schubert, G., Huster, F., & Fath, P. (2004). Current transport mechanism in printed Ag thick film contacts to an N-type emitter of a crystalline silicon solar cell. Proceedings of *19th European Photovoltaic Solar Energy Conference*, 813-816.

Shaheen, S. E., Radspinner, R., Peyghambarian, N., & Jabboura, G.E. (2001). Fabrication of bulk heterojunction plastic solar cells by screen printing. *Applied Physics Letters 79*, 2996-2998. doi:10.1063/1.1413501.

Sopori, B. (1982). A sectioning technique for demountable semiconductor samples. *Journal of Electrochemical Society*, *129*(2), 448-450.

Sopori, B. (1989). A rapid wax mounting technique for cross-sectioning and angle polishing metallographic samples. *Journal of Electrochemical Society*, *136* (1), 287-291.

Sopori, B. *Dry texturing for solar cell fabrication.* U.S. Patent No. 5,358,574.

Sopori, B. L., Deng, X., Benner, J. P., Rohatgi, A., Sana, P., Estreicher, S. K., Park, Y. K., & Roberson, M.A. (1996). Hydrogen in silicon: A discussion of diffusion and passivation mechanisms. *Solar Energy Materials and Solar Cells, 41-42,*159-169. doi:10.1016/0927-0248(95)00098-4.

Sopori, B. L., Zhang, Y., Reedy, R., Jones, K., Yan, Y., Al-Jassim, M., Kalejs, J. & Bathey, B. (2004). On the mechanism of hydrogen diffusion in si solar cells using PECVD SiN:H. Proceedings of *Materials Research Society Symposium,* 813, H6.2.

Sopori, B., & Mehta, V. (2009, October). Formation of screen-printed contacts on si solar cells. Paper presented at the *216th Electrochemical Society meeting*, Vienna, Austria.

Sopori, B., Mehta, V. R., Rupnowski, V. R., Domine, D., Romero, M., Moutinho, H., To, B., Reedy, R., Al-Jassim, M., Shaikh, A., Merchant, N., & Khadilkar, C. (2007). Studies on fundamental mechanisms in a fire-through contact metallization of si solar cells. Proceedings of the *22nd European Photovoltaic Solar Energy Conference*, 841-848.

Sopori, B., Mehta, V., & Knorowski, C. (2008, August). Technique for rapid cross-sectioning of si solar cells with highly planar, damage-free, edge. Poster session presented at the *18th Workshop on Crystalline Silicon Solar Cells and Modules: Materials and Processes*, Vail, CO.

Sopori, B., Mehta, V., & Ravindra, N.M. Back Al contact formation, to be published in *Journal of Materials Science.*

Sopori, B., Mehta, V., Fast, N., Moutinho, H., Domine, D., To, B., & Al-Jassim, M. (2007). Cross-sectioning si solar cells: Mechanics of polishing. Proceedings of *17th Workshop on Crystalline Silicon Solar Cells & Modules: Materials and Processes*, 222-227.

Sopori, B., Mehta, V., Guhabiswas, D., Reedy, R., Moutinho, H., Bobby, T., Shaikh, A., & Rangappan, A. (2009). Formation of a back contact by fire-through process of screen-printed silicon solar cells. Proceedings of the *34th IEEE Photovoltaic Specialists Conference*, 1963-1968. doi: 10.1109/PVSC.2009.5411536.

Sopori, B., Mehta, V., Rupnowski, P., Appel, J., Romero, M., Moutinho, H., Domine, D., To, B., Reedy, R., Al-Jassim, M., Shaikh, A., Merchant, N., Khadilkar, C., Carlson, D., & Bennet, M. (2007). Fundamental mechanisms in the fire-through contact metallization of si solar cells: A Review. Proceedings of *17th Workshop on Crystalline Silicon Solar Cells & Modules: Materials and Processes*, 93-103.

Sopori, B., Mehta, V., Rupnowski, P., Moutinho, H., Shaikh, A., Khadilkar, C., Bennett, M., & Carlson, D. (2009). Studies on backside Al-contact formation in si solar cells. In B. Sopori, J. Yang, T. Surek, B. Dimmler (Ed.), *MRS Symposium on Fundamental Mechanisms: Vol.1123. Photovoltaic Materials and Manufacturing Issues*, 7-11, Warrendale, PA.

Sopori, B., Nilsson, T., & McClure, M., (1981). Damage free polishing of polycrystalline silicon. *Journal of Electrochemical Society, 128*(1), 215-218.

Sopori, B., Rupnowski, P., Appel, J., & Mehta, V., (2006, October). Defect engineering approaches for improving silicon solar cell performance: Characterization, modeling, and cell fabrication. Poster session presented at the meeting of *CU/NREL Energy Symposium*, Boulder, CO.

Sopori, B., Rupnowski, P., Appel, J., Mehta, V., Li, C., & Johnston, S. (2008). Wafer preparation and iodine-ethanol passivation procedure for reproducible minority-carrier lifetime measurement. Proceedings of the *33rd IEEE Photovoltaic Specialists Conference*, 1-4. doi:10.1109/PVSC.2008.4922688.

Sopori, B., Rupnowski, P., Mehta, V., Budhraja, V., Johnston, S., Call, N., Moutinho, H., Al-Jassim, M., Shaikh, A., Seacrist, M., & Carlson, D. (2009). Performance limitations of mc-Si solar cells caused by defect clusters, *ECS Transactions 18* (1), 1049-1058. doi: http://dx.doi.org/10.1149/1.3096571.

Sopori, B., Rupnowski, P., Mehta, V., Ewan, M. (2008, August). Mechanism of hillock formation during chemical-mechanical polishing of multicrystalline silicon wafers. Poster session presented at the *18th Workshop on Crystalline Silicon Solar Cells and Modules: Materials and Processes*, Vail, CO.

Sopori, B., Rupnowski, P., Taliaferro, B., Gagnoon, D., & Li, C. (2005). Polishing multicrystalline silicon wafers for defect etching. Proceedings of *15th Workshop on Crystalline Silicon Solar Cells & Modules: Materials and Processes*, 222-228.

Sopori, B.L., Marshall, C., Rose, D., Jones, R.M., Reedy, R., & Asher, S. (1993). Optical processing: a novel technology for fabricating solar cell contacts. *Photovoltaic Specialists Conference, Conference Record of the 23rd IEEE.*97-100. 10.1109/PVSC.1993.347072.

Speed, M., Romero, M., To, B., Mountinho, H., Page, M., & Sopori, B. (2006). Cross-sectioning a finished solar cell for detailed characterization of cell structure," Proceedings of *16th Workshop on Crystalline Silicon Solar Cells & Modules: Materials and Processes*, 244-248.

Sun, T., Miao, J., Lin, R. & Fu, Y. (2005). The effect of baking conditions on the effective contact areas of screen-printed silver layer on silicon substrate. *Solar Energy Materials & Solar Cells, 85*(1), 73-83. doi:10.1016/j.solmat.2004.04.012.

Teng, K. F., & Vest, R. W. (1988). Metallization of solar cells with ink jet printing and silver metallo-organic inks. *IEEE Transactions on components, hybrids, and Manufacturing Technology, 11*, 291.

Thuillier, B., Berger, S., Boyeaux, J. P., & Laugier, A. (2000). Observation of mechanisms of screen printed contact formation during heat treatment on multicrystalline silicon solar cells by transmission electron microscopy. Proceedings of the *28th IEEE Photovoltaic Specialists Conference*, 411-413. doi: 10.1109/PVSC.2000.915855.

Thuillier, B., Boyeaux, J. P., Kaminski, A., & Laugier, A. (2003). Transmission electron microscopy and EDS analysis of screen-printed contacts formation on multicrystalline silicon solar cells. *Materials Science and Engineering B, 102*, 58-62. doi:10.1016/S0921-5107(02)00627-X.

Weber, L. (2002). Equilibrium solid solubility of silicon in silver. *Metallurgical and Materials transaction A* (33A), 1145-1150.

Yiwei, A., Yunxia, Y., Shuanglong, Y., Lihua, D., & Guorong, C. (2007). Preparation of spherical silver particles for solar cell electronic paste with gelatin protection. *Materials Chemistry and Physics, 104*(1), 158-161. doi:10.1016/j.matchemphys.2007.02.102.

Young, J.L., Mehta, V., Guhabiswas, D., Moutinho, H., Bobby To, Ravindra, N. M., & Sopori, B. (2009, August). Back contact formation in si solar cells: Investigations using a novel cross-sectioning technique. Poster session presented at *19th Workshop on Crystalline Silicon Solar Cells & Modules: Materials and Processes*, Vail, CO.

Young, R. J. S, & A. F. Carroll (2000). Advances in front-side thick film metallization for silicon solar cells. Proceedings of *16th European Photovoltaic Solar Energy Conference*, 1731-1734.